Numerical simulations and experimental studies of microfluidic droplet formation

Shazia Bashir

Submission for the degree of
Doctor of Philosophy

School of Mathematics and Statistics
August 2012

Supervisors: Dr. JM Rees,
Prof. WBJ Zimmerman

University of Sheffield

Abstract

Within the microfluidic platform, the formation of droplets inside an immiscible carrier fluid is a key process which forms the basis of several potential applications. A series of investigations on microfluidic droplet formation is presented in this study using both numerical and experimental techniques. Numerical simulations based on the two phase level set method were performed to enable a detailed parametric study of the droplet formation process. A detailed experimental study of the effects of surfactants on an oil-water interface and on channel wettability during the droplet formation process were performed. Microchannels were patterned in polydimethylesiloxane (PDMS) via a SU-8 mould fabricated using soft lithography technique in order to prepare microfluidic devices for droplet generation. Modification of the inner microchannel surface from hydrophobic to hydrophilic was achieved using a novel plasma polymerization technique which enabled the generation of oil-in-water droplets. We present a novel channel blocking technique used in conjunction with a plasma polymerized coating to partially modify the surface wettability of pre-assembled microfluidic devices. Under controlled flow rate conditions, these spatially patterned devices are shown to be

capable of generating water-in-oil-in-water double emulsions. Furthermore, we have used micron resolution particle image velocimetry (μPIV) to quantitatively describe the flow behaviour in both water-in-oil and oil-in-water emulsions.

Acknowledgments

I would like to express my most sincere gratitude to my supervisors, Dr. JM Rees and Prof. WBJ Zimmerman for their guidance, support and encouragement throughout this journey. I am thankful to 'faculty development program' of higher education commission, Pakistan for funding this research project. I would like to thank all of my friends, Dr. Daniel Rees, Dr. Andrew Newton, Amy Scott, Khairia Mira, Roald Koudenburg and Suliadi F Sufahani for being caring and motivating during this period of time. I am indebted to my CBE colleagues, Dr. Dimitry Kuvshinov, Dr. Rile Ristic and Dr. Hemaka Bandulasena, for many helpful discussions during the lab work. I would also like to acknowledge Dr. Xavier Casadevall i Solvas from Imperial College London for helping me in fabrication of microfluidic devices and giving me several tips for my very first experiment. Special thanks to my husband for his ultimate support and motivation in completing this thesis. At the end, I am grateful to my parents and siblings for their wishes and encouragement, and my sweet daughter Aliza for her patience and love.

Copyright Notice

Contents

List of Figures

List of Tables

Nomenclature

α	Ratio of neck width to main channel width	[Dimensionless]
β	Slip length	[μm]
δz_m	Measurement depth	[μm]
δ	Dirac delta function	[Dimensionless]
ϵ	Interface thickness	[μm]
η	Dynamic viscosity	[Pa.s]
γ	Reinitialization parameter	[Dimensionless]
κ	Curvature of the fluid-fluid interface	[m^{-1}]
λ	Quotient of the viscosity of the dispersed phase with the viscosity of the continuous phase	[Dimensionless]
λ_l	Wavelength of light	[nm]
$\mathbf{F}_{fr}$	Frictional force	[N]
$\mathbf{u}$	Velocity field	[ms^{-1}]
$\phi(\mathbf{x}, t)$	Level set function	[Dimensionless]
ρ	Density	[kgm^{-3}]
ρ_p	Particle density	[kgm^{-3}]
σ	Surface tension	[Nm^{-1}]
σ_{LG}	Surface tension at liquid/gas interface	[Nm^{-1}]
σ_{SG}	Surface tension at liquid/gas interface	[Nm^{-1}]
σ_{SL}	Surface tension at solid/liquid interface	[Nm^{-1}]

θ	Contact angle	[Degrees]
θ_a	Advancing contact angle	[Degrees]
θ_r	Receding contact angle	[Degrees]
ξ	Gap between the emerging droplet and the opposite wall of the main channel	[μm]
ζ	Shape factor	[Dimensionless]
A_s	Area of interface	[m^2]
C_s	Surfactant concentration	[Mol]
d_e	Effective particle diameter	[μm]
d_p	Particle diameter	[μm]
d_s	Diameter of the diffraction limited point-spread function	[μm]
D_{iw}	Water droplet size encased in an oil droplet	[μm]
g	Gravitational acceleration	[ms^{-1}]
L_d	Droplet length	[μm]
M	Magnification	[Dimensionless]
n	Refractive index	[Dimensionless]
NA	Numerical aperture	[Dimensionless]
p	Pressure	[Pa]
P_c	Continuous phase pressure	[Pa]
P_d	Dispersed phase pressure	[Pa]
Q	Ratio of flow rate of dispersed phase to the flow rate of continuous phase	[Dimensionless]
Q_c	Continuous phase flow rate	[$\mu l min^{-1}$]
Q_d	Dispersed phase flow rate	[$\mu l min^{-1}$]
Q_{ew}	External dispersed water phase flow rate	[$\mu l min^{-1}$]
Q_{iw}	Internal dispersed water phase flow rate	[$\mu l min^{-1}$]

Q_i	Flow rate ratio of internal water phase to the middle oil phase in double emulsion	[Dimensionless]
Q_{mo}	Middle oil phase flow rate	$[\mu \mathrm{l min}^{-1}]$
R_1, R_2	Principle radii of curvature	[m]
Re_c	Reynolds number based on continuous phase flow	[Dimensionless]
S	Spreading coefficient	$[\mathrm{N m}^{-1}]$
$t_{squeeze}$	Squeezing time of emerging droplet	[sec]
U_c	Continuous phase fluid velocity	$[\mathrm{m s}^{-1}]$
U_d	Dispersed phase fluid velocity	$[\mathrm{m s}^{-1}]$
U_{growth}	Growth rate of droplet	$[\mathrm{m s}^{-1}]$
w_c	Width of the main channel	$[\mu \mathrm{m}]$
w_d	Width of lateral channel	$[\mu \mathrm{m}]$
w_n	Neck width of emerging droplet	$[\mu \mathrm{m}]$

1

Introduction

This chapter provides an introduction to the field of microfluidics and droplet based microfluidics. The overview of droplet formation in microfluidics and surface modification of microfluidic devices is presented. The goals of this project are outlined and brief descriptions of each chapter are presented.

1.1 From microfluidics to droplet microfluidics

Microfluidics is the miniaturization of chemical and biological processes, which involves the manipulation of very small volumes (pico- to nano-liter) of fluids in a precise and controlled manner. It has therefore been proved to be a promising technology for performing laboratory scale experiments for high throughput applications. Miniaturization of laboratory scale operations in microfluidic devices (also known as lab on a chip systems) has resulted in many processes now being carried out more efficiently with the requirement of reduced reagent costs (Stone et al., 2004; Su et al., 2006; Solvas and deMello, 2011). The behavior of a fluid at a microfluidic scale can differs significantly from that on the macrofluidic scales. Typically, flow in microfluidic devices occurs at low Reynolds numbers (Re $\sim$ O(1)) and thus is solely laminar (Teh et al., 2008; Squires and Quake, 2005). Due to this laminar flow behaviour, mass transfer and mixing processes occuring across adjacent fluid streams are dominated by diffusion rather than by convection as in the macroscale case (Teh et al., 2008; Stone et al., 2004; Figeys and Pinto, 2000; Weigl and Yager., 1999). Such slow mixing rates can pose disadvantages for performing chemical reactions within microfluidic length scales. However, due to the parabolic flow profile associated with the laminar flow, dispersion of solutes can occur along the microchannel (Taylor-Aris dispersion (Taylor, 1953)), which can lead to dilution and cross-contamination of injected samples (Herlod and Rasooly., 2009).

Droplet-based microfluidics provides a platform of fluid manipulation within droplets. Monodispersed droplets can be precisely controlled within a microchannel and hence they can be mixed, reacted, stored and analyzed as discrete microreactors. The confinement of samples inside liquid droplets, or plugs,

surrounded by another immiscible fluid has been shown to overcome many of the problems encountered in continuous phase microfluidic systems (Song et al., 2006; Leshansky and Pismen, 2009). As droplets formed in emulsions are separated from the microchannel walls by a thin layer of carrier fluid. Problems associated with reagents in the droplets adhering to the microfluidic channel walls, and with axial dispersion in the microchannel is prevented. Also, no cross-contamination occurs between successive sample reagents inside these droplets. The major advantages of droplet based fluidic systems are the existence of a high surface-to-volume ratio, often by several orders of magnitude, compared to those of macroscale devices. Therefore, transfer processes can occur across a greater interfacial surface area, leading to increased heat and mass transfer rates due to the presence of recirculation zones within the liquid droplets.

1.2 Droplet formation in microfluidics

Over the last decade droplet formation has become a very important area of research due to its wide-ranging applications in science and microprocess engineering. The ability to produce nearly monodispersed microdroplets has numerous applications within microfluidic based lab on a chip devices (Yap et al., 2009). Commonly, the fluid chosen to be dispersed in the form of droplets is known as the dispersed phase and the fluid used as a droplet carrier is known as the continuous phase. The controlled formation of microdroplets has unique advantages as the consumption of reagents is small (Song et al., 2006; Li et al., 2008). Liquid droplets are particularly well-suited for biochemical reactions (e.g., protein crystallization) where each droplet can serve as an individual chemical reactor (Song et al., 2006; Stone et al., 2004; Breslauer et al., 2006; Zheng et al., 2004;

Leng and Salmon, 2009). In each of these microreactors aqueous solutions are manipulated at room temperature. Mixing in these liquid microdroplets has been achieved effectively (Song et al., 2003; Tice et al., 2003; Bringer et al., 2004). The fine controls possible over the size and shape of these microdroplets are of much importance since they influence the biological and chemical properties of microparticles (Teh et al., 2008). A number of methods have been developed for droplet formation in microfluidic channel. These include droplet breakup at a symmetric T-junction (Leshansky and Pismen, 2009) or bifurcation junction (Jullien et al., 2009), flow focussing of a continuous stream of liquid which guides the droplets formed towards the center of the channel (Anna et al., 2003; Tan et al., 2006), perpendicular rupturing using a cross-flow microchannel (Tan et al., 2008), and the shearing of the dispersed phase stream by the continuous phase at a T-junction (Thorson et al., 2001; Nisisako et al., 2002; Garstecki et al., 2006). T-shaped microdroplet generators are the simplest and most widely used, in which the dispersed phase is sheared off by the continuous phase in order to generate highly monodispersed microdroplets. In contrast to droplet formation in macroscale systems, droplets formed in microdevices tend to be stable, free from coalescence and do not break up as they propagate downstream. A microfluidic device for generating uniform sized water droplets within an oil phase incorporating a T-junction was first introduced by Thorson et al. (2001). They suggested that the dynamics of the droplet breakup process is determined by the balance between the tangential shear stress and the interfacial tension. Nisisako et al. (2002) described a procedure for generating pico/nanoliter sized water droplets within an oil-based continuous phase using a T-junction microchannel. They succeeded in controlling the droplet diameter reproducibly by varying the flow velocity of the continuous phase. Van

der Graaf et al. (2005) used a T-shaped microchannel to investigate unconfined droplet breakup as a model for membrane emulsification. A similar microfluidic device was used by Husny and Cooper-White (2006) to examine the influence of liquid viscosities and elasticity on the mechanism of droplet breakup. They found that the presence of elasticity with low viscosity fluids resulted in the creation of secondary drops of varying sizes. A detailed study of the formation of droplets and bubbles in a T-junction microchannel was carried out by Garstecki et al. (2006). They identified that, in the squeezing regime, the droplet breakup process is dominated by the pressure drop across the droplet as it emerges and proposed a scaling law for the length of the confined droplet that depends only on the flow rate ratio of the two immiscible fluids. Xu et al. (2008) investigated scaling laws for controlling the range of droplet sizes within the squeezing and dripping regimes in T-junction microfluidic devices. Christopher et al. (2008) reported on a detailed experimental study of droplet breakup in the squeezing-to-dripping transition in T-shaped microfluidic junctions. They found that the dimensionless lengths of the stable droplets produced depended qualitatively on flow rate, capillary number and the ratio of the widths of the inlet channels, which controls the degree of confinement of the droplets.

Besides experimental observations, numerical techniques are of importance for investigating multiphase flows in microfluidic devices. Recent advances in computational fluid dynamics (CFD) particularly for multiphase flows, have made the prediction of local parameters of the flow regime within a microfluidic device, such as velocity profiles, temperature and pressure gradients, and interface configurations, more accessible. Better understanding of these features is important for improving the design and control of microfluidic devices. Such data may be difficult, or even impossible, to extract from experiments. Sang et al. (2009)

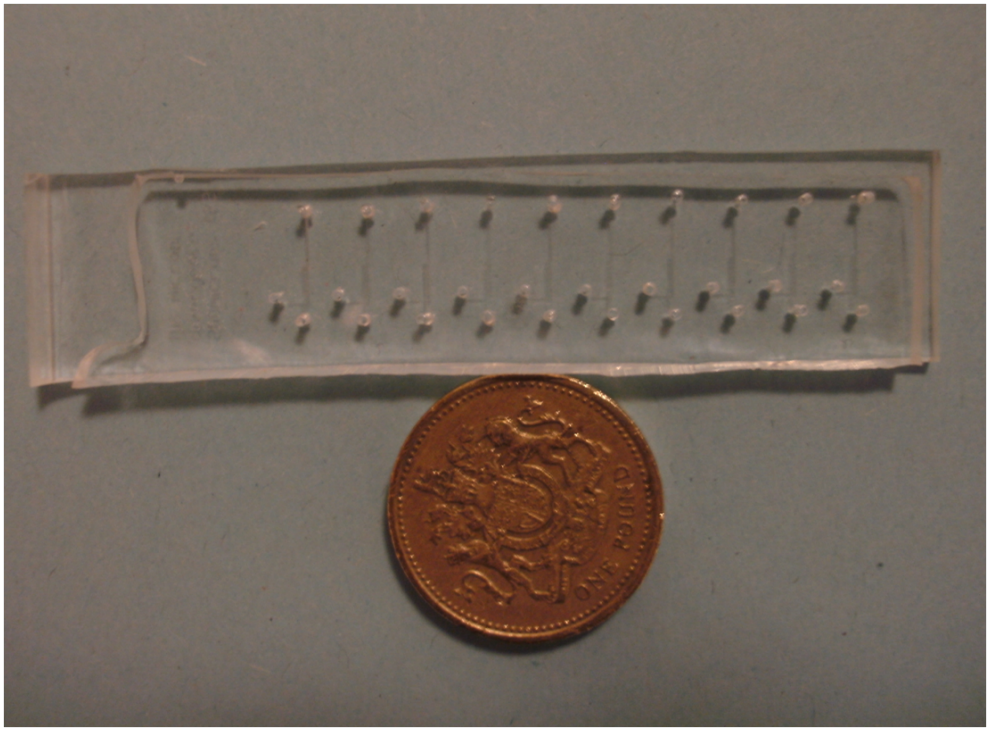

Fig 1.1. PDMS microchip with multiple microchannels compared to one pound coin.

investigated the effect of viscosity on droplet formation in T-shaped microchannels using numerical and analytical methods. Qian and Lawal (2006) studied the gas-liquid slug flow regime in T-junction microchannels using the volume-of-fluid (VOF) based commercial CFD package FLUENT. The predicted lengths of slugs at various operating conditions were found to be in good agreement with experimental observations. Zhou et al. (2006) performed a numerical study of the formation of simple and compound drops in microfluidic flow-focusing devices. They used a finite element scheme with adaptive meshing in a diffuse-interface framework to simulate breakup in coflowing conditions and also to investigate the effects of viscoelasticity in the drop phase. Davidson et al. (2005) used a VOF method to predict the dynamics of droplet formation in a microfluidic flow-focusing geometry. They obtained a qualitative comparison

between the VOF simulations and experimental observations. Van der Graaf et al. (2006) used the Lattice Boltzmann method to model the droplet breakup process at a T-junction and derived a semiempirical model for estimating the droplet volume in terms of flow rate and capillary number. Based on numerical simulations using a phase field method, De Menech et al. (2008) categorized the droplet breakup process into three different regimes: squeezing, dripping and jetting.

1.3 Types of emulsions and their stability

There are two types of emulsions that are typically generated in microfluidic devices, namely water-in-oil (W/O) emulsions, in which water is the dispersed phase and oil is the continuous phase, and oil-in-water (O/W) emulsions, in which oil is the dispersed phase and water is the continuous phase. In addition to single emulsions, double emulsions also exist. A double emulsion comprises an emulsion within an emulsion. There are two main types of double emulsions, namely: water-in-oil-in-water (W/O/W) and oil-in-water-in-water (O/W/O)(Link et al., 2004; Okushima et al., 2004). W/O emulsions can be generated in hydrophobic microchannels (e.g., PDMS, PMMA) where oil preferentially wets the channel walls. O/W emulsions can be generated in hydrophilic microchannels (e.g., those made from glass or quartz) where water preferentially wets the channel walls. Stable formation of liquid droplets dispersed in another liquid (or emulsions) requires an emulsifier or surfactant. Surfactants have the ability to radically alter surface and interfacial properties. Therefore, surfactants can be used to incur wettability modifications. The dynamical effects exerted by a surfactant on the interface between two fluids reduces the interfa-

cial tension. This reduction of the interfacial tension contributes towards the stabilization of droplets against coalescence. The choice of surfactant depends on the type of emulsion and wettability of microfluidic device.

1.4 Surface modification of microfluidic device

The control of surface properties of microfluidic devices is necessary in order to exploit them for a wide range of applications in microfluidics. In order to generate droplets in microchannels, the continuous phase should completely wet the channel surface while the dispersed phase should be non-wetting. For the formation of oil droplets in water (O/W) the microfluidic channel needs to be hydrophilic, and for water in oil emulsions the channel should be hydrophobic. Therefore, the choice of appropriate materials for microfabrication and surface modification methods for droplet generation and their manipulation is important. Preparation of both types of emulsions within the same type of microfluidic device requires surface modification. Usually glass based microchannels are used in order to form oil-in-water emulsions. The surface of a glass microchannel needs to be modified if the desire is to generate a water-in-oil emulsion. Also, a section of a glass microchannel needs to be modified in order to generate W/O/W and O/W/O double emulsions (Okushima et al., 2004). Even though well developed modification methods exist for glass microchannels, their use is not common place due to costly and time consuming fabrication processes. In contrast to this, polymer based microfluidic devices, especially those made from PDMS are cheap and fast to replicate. Other attractive properties of PDMS are its biocompatibility, optical transparency, non-toxicity and permeability to gases. However, PDMS surface modification for generating oil-in-water emul-

sions is a challenging task due to its fast hydrophobic recovery (Bodas and Khan-Malek, 2007; Hillborg et al., 2000). A number of methods have been applied for PDMS surface modification such as silanization (Papra et al., 2001), graft polymerization (Hu et al., 2002), sol-gel methods (Roman et al., 2005) and layer-by-layer methods (Bauer et al., 2010). Although these methods have been widely used for surface modification of PDMS microchannels, they are wet chemical, multistep and time consuming processes. Furthermore, clogging of microchannels may occur (e.g., during graft polymerization) which could alter the channel dimension due to poor control of coating thickness. Therefore, the development of an efficient surface modification method is vital to render the PDMS surface to be stably hydrophilic. We have used the technique of plasma polymerization to modify PDMS devices, exploiting the advantage of it being single and dry step process.

1.5 Thesis goals and layout

The role of wettability of a microchannel surface for the formation of droplets of the dispersed phase within a continuous phase is the main subject of this thesis. The thesis presents numerical simulations of droplet formation using the two phase level set method and considering its potential for exploring the effects of a number of physical parameters to improve on a fundamental level our understanding of the process. We have studied numerically how the process of droplet formation in a microfluidic T-junction is influenced by several parameters that could be controlled to optimize the performance of a microfluidic device. The dynamic surface modification of PDMS microchannel walls was performed experimentally by the use of surfactant in a carrier oil phase

to enhance the wetting of the microchannel by the oil phase. This lead to the stable formation of water droplets in the T-junction microchannel. Hydrophilic surface modification of a PDMS microchannel using a novel microjet plasma polymerization technique was carried out in order to generate oil-in-water and water-in-oil-in-water emulsions. Also, two phase flow behaviour in microchannel was quantitatively described using μPIV.

This thesis consists of eight chapters, the organization of them is as follows: Chapter 1 presents an introduction to droplet based microfludics and droplet formation in microfluidics. The role of surfactants in droplet formation and motivation for modifying the surface wettability of microfluidic devices is also discussed. Chapter 2 presents underlaying physical concepts in microfluidics along with a description of the role of surfactants in the formation of emulsions. In chapter 3, the two phase level set method is used to study the effects of several parameters such as flow rate, interfacial tension and, in particular, wettability effects on droplet formation in a T-junction microfluidic device. In chapter 4 we present a detailed numerical study on the upstream pressure profiles in the squeezing regime for investigating the response to the breakup of plugs at a T-junction of a confined microchannel. The experimental work on microfluidic droplet formation highlights some important aspects which is presented in chapters 5, 6 and 7. In chapter 5, we discuss surface tension effects and presents contact angle measurements. The dynamic wetting of droplets in microchannel in presence of surfactants is explored. In chapter 6, a novel plasma polymerization method for modifying PDMS microfludic channels is presented. Its use for the formation of oil-in-water emulsions and water-in-oil-in-water double emulsions is investigated. A novel spatial patterning of the microfluidic device for generating double emulsions within a single device is pre-

sented. Chapter 7 presents flow visualization and measurement using micron resolution particle image velocimetry. Chapter 8 summarizes the results from the thesis and highlights future perspectives.

2

Background

This chapter introduces some basic concepts necessary for understanding the behaviour of fluid flow at microscales, along with the role of surfactants in the preparation of emulsions. The objective of this chapter is to provide the reader with a comprehension of the topics presented in subsequent chapters. The last section presents the general mechanism of the droplet formation process in a T-junction microchannel.

2.1 Fundamentals of microfluidics

Microfluidics is the study of fluid dynamics and manipulation in lab on a chip devices. The behavior of fluids at the 'microscale' differs from that at 'macroscales' due to the scaling effects. Therefore, improved understanding of physical phenomena at microfluidic scales is an important goal.

2.1.1 Dimensionless numbers

The relative importance of different physical phenomena associated with microscale flows must be assessed. Dimensionless parameters compare the importance of these phenomena as given below:

The Reynolds number (Re) characterizes the relative importance of the inertial to viscous forces,

$$Re = \frac{\rho U L}{\eta}, \tag{2.1}$$

where ρ is the density of the fluid, U is a characteristic fluid velocity, L is a characteristic length of the geometry, and η is the dynamic viscosity of the fluid. The Reynolds number is generally very small in microfluidics analogous to a laminar flow regime.

The Bond number (Bo) is a measure of the importance of gravitational forces relative to surface forces,

$$Bo = \frac{\Delta\rho g L^2}{\sigma}, \tag{2.2}$$

where $\Delta\rho$ is the volumic mass difference between the two fluids, g is the gravitational acceleration and σ is surface tension or interfacial tension between the two fluids. At microscales, surface forces dominate over the force of gravity

therefore Bo $<<$ 1. The capillary number (Ca) is very important dimensionless number in two-phase microfluidics. It compares the viscous forces to the surface tension forces,

$$Ca = \frac{\eta U}{\sigma}. \tag{2.3}$$

The capillary number is a useful criterion on which predictions related to the droplet breakup in microfluidic devices can be made. The friction of droplets confined within the walls of a microchannel is a function of the capillary number of the liquid of which the droplet is composed.

The Weber number (We) relates the inertial forces to the surface tension:

$$We = \frac{\rho U^2 L}{\sigma}. \tag{2.4}$$

Usually, We remain less than 1 in most microfluidic applications as inertia becomes insignificant in flow geometries with micron scale dimensions. Exceptionally, it is used to predict the distortion of an interface between two fluids under the action of very high speed flows.

2.1.2 Microhydrodynamics

The fluid dynamics of incompressible, Newtonian fluids is described by the Navier-Stokes equations, which represent the continuum version of Newton's second law of motion ($\mathbf{F} = m\mathbf{a}$):

$$\rho \frac{\partial \mathbf{u}}{\partial t} + \rho(\mathbf{u}.\nabla)\mathbf{u} = -\nabla p + \eta \nabla^2 \mathbf{u} + \mathbf{F}. \tag{2.5}$$

The terms on the right hand side represent the forces per unit volume and those on the left hand side represent inertial acceleration. Here, p is the pressure and $\mathbf{F}$ represents the body forces. In microfluidics, as inertial forces are small compared to viscous forces, Reynolds numbers are small. Microhydrodynamics involves the study of flow at low Reynolds number. As a consequence of these small Reynolds numbers, the nonlinear term in the Navier-Stokes equations can be neglected, resulting in the simplified equation (Hessel, 2004; Nguyen and Wereley, 2006; Li, 2008):

$$\rho\frac{\partial \mathbf{u}}{\partial t} = -\nabla p + \eta\nabla^2\mathbf{u} + \mathbf{F}. \tag{2.6}$$

2.1.3 Surface (or interfacial) tension

As the surface-to-volume ratio in droplet based microfluidic systems is large, surface tension is an important force that exists between two immiscible fluids. The term interfacial tension is used instead of surface tension when both immiscible fluids are liquids. The surface (or interfacial) tension has the units of energy per unit surface, and in an SI units is expressed as $\mathrm{J/m^2}$ or N/m. The total energy of a surface (an interface) is defined as

$$E = \sigma A_s, \tag{2.7}$$

where σ is the surface tension between the two fluids and A_s is the area of interface.

The existence of a surface tension force results in a pressure difference across a curved liquid surface or a drop. The magnitude of this differential pressure is

given by the Young-Laplace law which demonstrates that in order to maintain the interface in equilibrium, a high pressure needs to be exerted across the interface, This is defined as:

$$\Delta P = \sigma \left(\frac{1}{R_1} + \frac{1}{R_2} \right), \tag{2.8}$$

where R_1 and R_2 are the principle radii of curvature. If the curvature is spherical, then $R_1 = R_2$ and Eq. 2.8 reduces to:

$$\Delta P = \frac{2\sigma}{R}. \tag{2.9}$$

For a droplet moving forward in a microfluidic channel, the Laplace pressure depends on both the interfacial tension and contact angle:

$$\Delta P = \frac{4\sigma \cos\theta}{d}, \tag{2.10}$$

where θ is the contact angle that the droplet makes with the microchannel surface. (The term 'contact angle' is described in the subsequent section 2.1.4) and d is the width of the microchannel. This pressure is of importance during the droplet formation process in microchannels as droplet generation starts when the pressure difference applied between the two phases exceeds the Laplace pressure (Tong and Nakajima, 2000).

2.1.3.1 Pendant drop method

A number of different techniques exist for measuring the surface (or interfacial) tension between two fluid phases. The choice of the measurement technique in a particular case depends upon the nature of the liquid to be measured, the

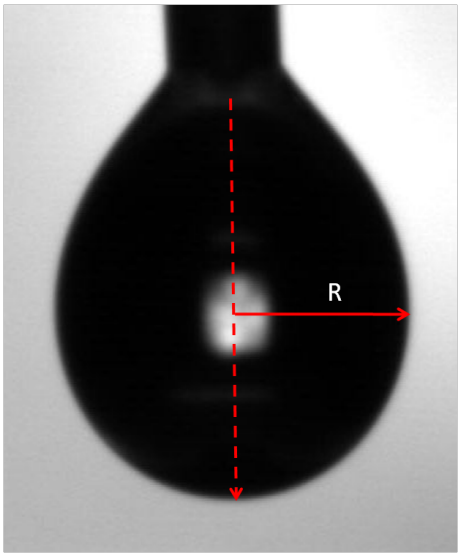

Fig 2.1. The pendent drop of water hanging down from a tip of syringe needle.

conditions for measuring its surface tension, and its surface stability during deformation. The pendant drop method involves analyzing the shape of drops. For example, the profile of a drop of a denser liquid being suspended from a syringe needle tip in a less dense medium (liquid or air) at an equilibrium (Fig. 2.1) can be determined. Gravity acts to elongate the drop whilst interfacial tension resists this elongation due to the increase in interfacial area. The profile of a drop of the liquid suspended in another medium is thus determined by a balance between gravity and surface forces. In order to get reliable results using a 2D drop shape analysis, the drop should be symmetric about a central vertical axis. This means the viewing direction of the drop is irrelevant. Secondly, the drop should not be in motion during the analysis in order to eliminate inertial effects. Therefore, the only forces responsible for shaping the drop are surface tension and gravity and hence the interfacial tension relates to the drop profile through the following equation (Bashforth and Addams, 1882; Hansen and Rodsrun, 1991):

$$\sigma = \frac{\Delta \rho g R^2}{\zeta}, \tag{2.11}$$

where R is the radius of curvature of the drop at its apex and ζ is the shape factor which determines the drop shape profile. The pendant drop method is useful for handling tiny amounts of liquids and accurate measurement of low surface (or interfacial) tensions.

2.1.4 Surface wetting

Wetting (or wettability) refers to a property that characterizes the spreading of a liquid on a solid surface and is quantified by the contact angle (θ). The bahaviour of a liquid drop when it comes in contact with a solid surface is of great importance. For instance, in two phase microfluidic systems, the wetting property of one liquid with respect to another liquid, gas or substrate is of key importance. In droplet formation processes the interaction of fluids with the solid surface of channel walls is governed by the wetting principle. A contact angle is the angle that a liquid/liquid or liquid/gas interface forms with the solid surface. Wetting can be categorized into two regimes: total wetting and partial wetting. Total wetting occurs when a liquid spreads out on a solid surface. Partial wetting refers to the case when the liquid remains in the form a drop. They can be distinguished by a parameter called 'spreading coefficient' (Gennes, 1985; Berthier and Silberzan, 2006).

$$S = \sigma_{SG} - (\sigma_{SL} + \sigma_{LG}), \tag{2.12}$$

where σ_{SG}, σ_{SL} and σ_{LG} denote the surface tensions of liquid/gas, solid/liquid and liquid/gas interfaces respectively. If the spreading coefficient (S) is positive,

the liquid completely spreads out over the solid surface and lowers its surface energy. In this case the contact angle $\theta = 0°$. On the other hand, if S is negative, the case is referred to as partial wetting. In this case, the liquid does not spread completely but instead forms a spherical cap sitting on a solid surface with a contact angle θ, where $0 < \theta < 90°$. In this latter case, a line exists where all three phases come into contact with each other. This line is called a triple line (Berthier and Silberzan, 2006). A schematic illustration of wetting phenomena is shown in Fig. 2.2. Generally, a liquid is "wetting" or "non-wetting" a solid surface depending on the contact angle that a liquid drop forms with that surface. The terms hydrophilic or hydrophobic depict the characteristics of the solid surface with reference to water. The surface is hydrophobic if the contact angle of a water drop with the surface θ is greater than $90°$, and is hydrophilic if $\theta < 90°$ (Fig. 2.3). The wetting criteria or the contact angle can be derived by considering the surface tensions of all the three phases. At the contact line (or triple line), the sum of the surface forces equates to zero. From projection of these equilibrium forces onto the plane (horizontal) of a solid surface, one can obtain the following relation:

$$\sigma_{SG} - \sigma_{SL} = \sigma_{LG} \cos\theta. \tag{2.13}$$

This relation is known as Young's relation or the Young-Dupre equation. Hence an expression for the contact angle can be written as:

$$\theta = \arccos \frac{\sigma_{SG} - \sigma_{SL}}{\sigma_{LG}}. \tag{2.14}$$

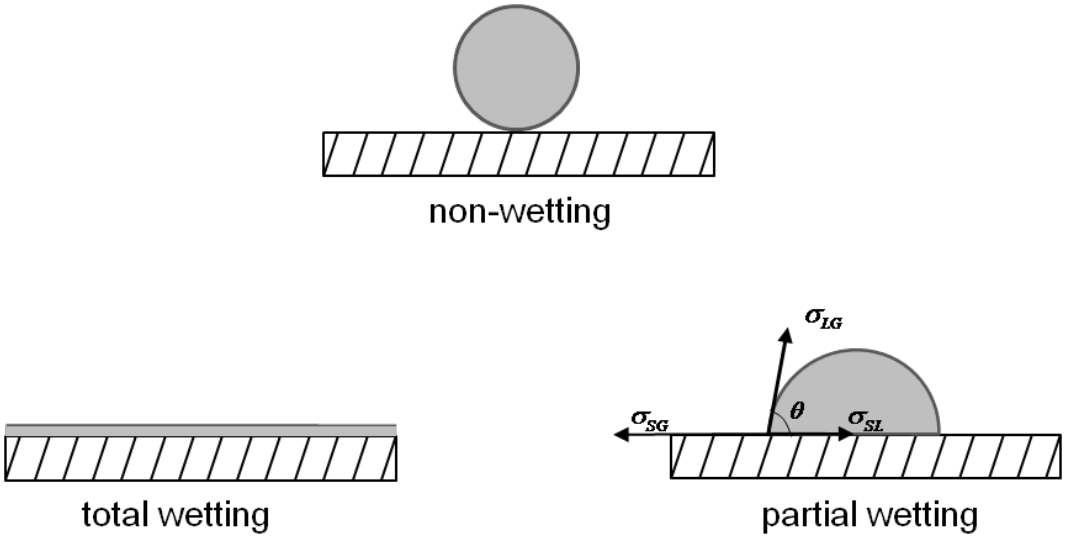

Fig 2.2. Schematic of wetting regimes.

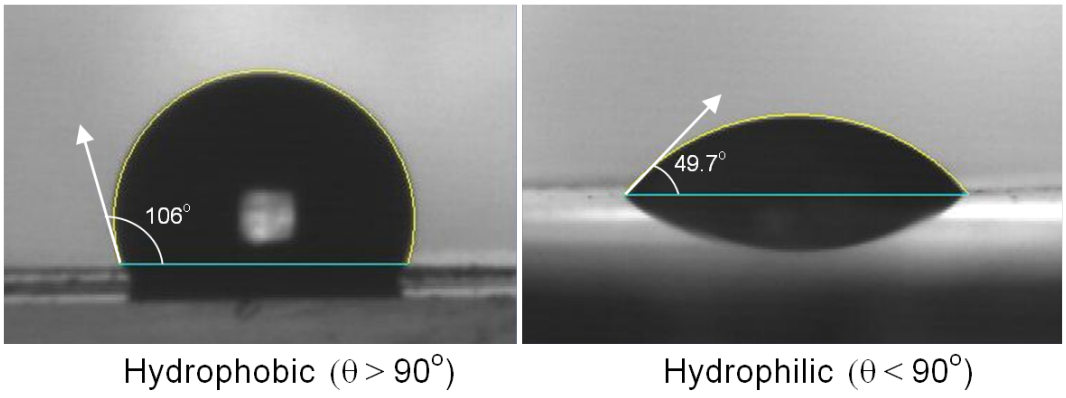

Fig 2.3. Water contact angles measured on hydrophobic (PDMS) and hydrophilic (glass) substrates.

2.2 Surfactants in emulsions

Emulsions consist of two immiscible liquids such that one liquid is dispersed in the form of droplets into the other. Emulsions comprising droplets of water in oil (W/O) and oil in water (O/W) are typically of the size of a few microns. Emulsions are usually thermodynamically unstable. In order to produce stable emulsions and to avoid several breakdown processes associated with them such as coalescence and ostwald ripening (Tardos, 2009), a third component is required, called a surface active agent (surfactant) or emulsifier. Practical applications of emulsions include pharmaceutical (such as lipid emulsion), cosmetics (such as skin creams, lotions) and food products (such as milk, mayonnaise).

Although emulsions formed in microfluidic devices are thermodynamically metastable and do not require surfactant for their preparation, the coalescence of droplets occurs extremely rapidly in the absence of surface active agents. Also, in order for droplets to act as sealed containers, the presence of surfactant at an interface is necessary. Therefore the use of surfactants in microfluidic droplet formation is unavoidable.

A surfactant molecule consists of two parts with different affinities: a hydrophilic part which forms a 'polar head' and a hydrophobic part which forms a 'non-polar' tail. The adsorption (accumulation) of surfactant at an interface (liquid/liquid or liquid/air) takes place in such a way that its hydrophilic part is oriented towards the hydrophilic phase (such as water) and its hydrophobic part is oriented towards the hydrophobic phase (such as oil) (see Fig. 2.4). This results in a lowering of the surface tension (or interfacial tension) between the two phases. For instance, adsorption of surfactant at a water/air interface reduces

the surface tension of water from 72.80 mN/m to $\sim$ 30 mN/m (Berthier and Silberzan, 2006). In microfluidic droplet formation, surfactant plays a vital role as the reduction of an interfacial tension favors the droplet breakup and reduces the droplet size. A specific type of emulsion (W/O or O/W) depends on the nature of a surfactant chosen. For water-in-oil (W/O) emulsions the surfactants should be more soluble in oil and for oil-in-water (O/W) emulsions surfactants should be more soluble in water. The choice of a particular surfactant that favors either O/W or W/O emulsion is based on the hydrophilic-lipophilic balance (HLB) concept which was introduced by Griffin (Griffin, 1949). HLB defines the criterion on the basis of whether the surfactant can be judged to be more soluble in oil or water. It is a numerical value that is derived from the relative proportion of both hydrophilic and hydrophobic (lipophilic) groups in the surfactant molecule and is given by the following relation:

$$HLB = 7 + \sum(No.\ of\ hydrophilic\ groups) - \sum(No.\ of\ lipophilic\ groups). \tag{2.15}$$

For non-ionic surfactants, HLB numbers ranges from 0-20. The higher the HLB value, the more hydrophilic the surfactant is and the lower the HLB value indicates the more hydrophobic the surfactant. If a surfactant is mostly soluble in an oil HLB $\sim$ 3 to 6, and if it is mainly soluble in water HLB $\sim$ 8 to 18. (Griffin, 1954; Davies, 1957).

2.3 Mechanism of microdroplet formation

As stated earlier, the droplet formation process can be classified into three regimes: squeezing, dripping and jetting (De Menech et al., 2008). The squeez-

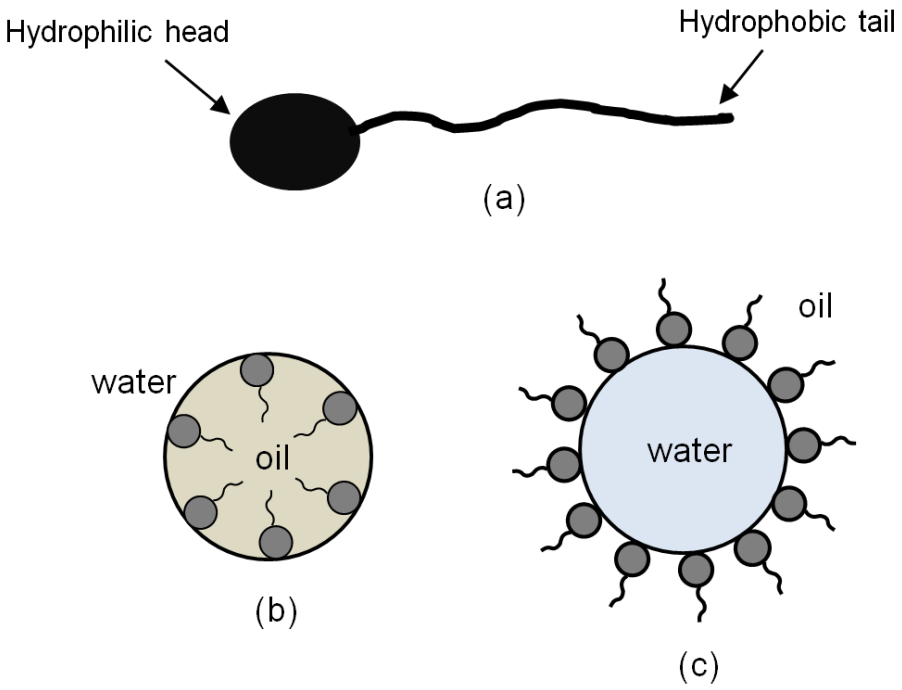

Fig 2.4. (a) Surfactant molecule, (b) O/W emulsion, (c) W/O emulsion.

ing and dripping mechanisms commonly occur in microchannel flows where droplet formation is influenced by the physical confinement of the microchannel walls. In the squeezing regime the upstream pressure exerts the primary influence on droplet formation, the value of the capillary number having only a small effect. In the dripping (shear-dominated) regime droplet size is influenced by the balance between interfacial and viscous stresses. The jetting regime occurs at high capillary numbers (low interfacial tension or very high flow rates) and is thus rarely observed in microchannel flows. In a T-shaped microfluidic device, which has been studied in this thesis, microdroplets can be generated at the T-junction intersection where two channels perpendicularly intersect each other. The main channel carries the continuous phase (e.g. oil) and the orthogonal channel is the inlet for the internal phase (e.g. water). The right angle intersection for both phases is chosen due to the highest shear rate occurring at

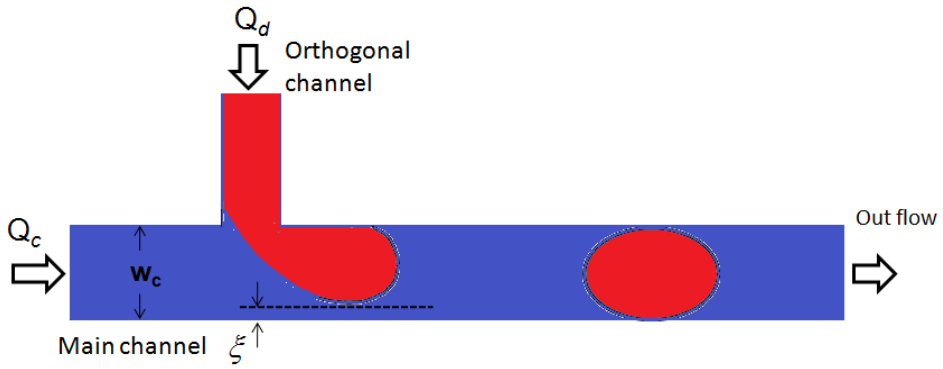

Fig 2.5. Droplet formation mechanism.

the emerging dispersed phase while turning the 90° bend to enter into the main channel, which results in a minimum droplet breakup time (Tan et al., 2009).

The two immiscible fluids form an interface at the junction. In the first stage of droplet formation, a stream of the dispersed phase fluid penetrates into the main channel. In the second stage, it forms a plug of length approximately equal to the width of the main channel w_c. This plug blocks nearly the entire cross-section of the main channel except for a small gap of width ξ (Fig. 2.5) between the blob and the opposite wall of the main channel (De Menech et al., 2008). As the interface moves downstream, there is an interplay between interfacial and shear forces. The relative effects of surface tension and viscosity acting across an interface between two immiscible liquids are represented by a capillary number (Ca). By convention for droplet formation this is based on parameters pertaining to the continuous phase:

$$Ca = \frac{\eta_c U_c}{\sigma},$$

where η_c is the viscosity of the continuous phase fluid, σ is the interfacial tension between the two immiscible fluids and U_c is the carrier fluid velocity. At low

values of Ca (typically less than 10^{-2}), interfacial forces dominate over shear stresses leading to instability in the flow. If the flow rate of the dispersed phase (Q_d) is higher than that of the continuous phase (Q_c), the droplet elongates in the main channel and the developing neck starts to thin. Eventually breakup occurs after the detachment of the dispersed phase from the T-junction due to the pressure drop across the droplet in the main channel. This pressure drop arises from high resistance to the flow of the continuous phase that separates the droplet from the walls of the microchannel by a thin layer. This regime is usually called a 'squeezing regime' (Garstecki et al., 2006). In the opposite case, when $Q_d < Q_c$ the droplet does not have time to elongate and breakup occurs immediately after a plug of length w_c is formed. In this study we consider the situation $Q_d < Q_c$ so that droplet detachment occurs at the junction. For $Q_d >> Q_c$, flow streamlines become close to parallel to the channel wall with breakup occurring far downstream. Droplet breakup in the vicinity of the junction is a more stable process and permits detailed investigation of the transition from squeezing to dripping regimes to be made. At high values of Ca (greater than 10^{-2}), shear forces play an important role. The continuous phase exerts a shear stress on the emerging droplet until it breaks off at the upper wall adjacent to the junction without blocking the cross-section of the main channel. This is called a 'shearing regime'. After breaking off, the droplet moves downstream in the main channel. At the same time the tip of the dispersed phase moves back to the end of the inlet channel and the process repeats itself. Therefore, the balance between the shear force and the interfacial tension determines the size of the droplet formed inside the microchannel.

3

Simulations of microfluidic droplet formation using the two phase level set method

Microdroplet formation is an emerging area of research due to its wide-ranging applications within microfluidic based lab-on-a-chip devices. Our goal is to understand the dynamics of droplet formation in a microfluidic T-junction in order to optimize the operation of the microfluidic device. Understanding of this process forms the basis of many potential applications: synthesis of new materials, formulation of products in pharmaceutical, cosmetics and food industries. The two-phase level set method, which is ideally suited for tracking the interfaces between two immiscible fluids, has been used to perform numerical simulations of droplet formation in a T-junction. Numerical predictions compare well with experimental observations. The influence of parameters such as flow rate ratio, capillary number, viscosity ratio and the interfacial tension between the two immiscible fluids are known to affect the physical processes of droplet generation. In this study the effects of surface wettability, which can be controlled by altering the contact angle, are investigated systematically. As competitive wetting between liquids in a two phase flow can give rise to erratic flow patterns, it is often desirable to minimize this phenomenon as it can lead to a disruption of the regular production of uniform droplets. The numerical simulations predicted that wettability effects on droplet length are more prominent when the viscosity ratio λ (the quotient of the viscosity of the dispersed phase with the viscosity of the continuous phase) is O(1), compared to the situation when λ is O(0.1). The droplet size becomes independent of

contact angle in the superhydrophobic regime for all capillary numbers. At a given value of interfacial tension, the droplet length is greater when λ is O(1) compared to the case when λ is O(0.1). The increase in droplet length with interfacial tension, σ, is a function of $\ln \sigma$ with the coefficients of the regression curves depending on the viscosity ratio.

3.1 Introduction

Microfluidics is a relatively recent interdisciplinary field, spanning only the last 20 years. The utilization of microfluidic systems for the generation of droplets is even more recent, as it has gained considerable attention only during the last decade. Rapid developments in the understanding of multiphase flows in microfluidics and in the broad range of applications of these miniaturized systems to the production of droplets forms the basis of numerous commercial applications (Tabeling, 2005).

Several numerical studies have addressed the issue of microdroplet generation. The formation of microdroplets of a dispersed fluid within a continuous fluid is an unsteady process involving moving fluid-fluid interfaces and is therefore a complex flow field. Consequently, the numerical modeling of droplet generation becomes a complicated and challenging task.

The process of microdroplet formation depends on several parameters, including the flow rates of the dispersed and continuous phases, the interfacial tension between the two immiscible fluids and the wetting properties of the channel wall. The physical properties of the continuous phase are also shown to influence droplet formation behavior and the final size and shape of the droplet (Kobayashi et al., 2005). Parametric studies of the interfacial tension between two immiscible fluids and the wetting properties of the channel walls are difficult to achieve experimentally as their optimization involves several complicated processes. Usually, surface active agents can be used to alter interfacial tensions. Chemical coatings can be applied to microchannel surfaces to alter the non-wettability of the dispersed phase.

Numerical studies on droplet formation with various computational schemes have been reported during the last few years. Van der Graaf et al. (2006) used the Lattice Boltzmann method (LBM) to model droplet formation at a T-junction incorporating wetting wall boundary conditions. Sang et al. (2009) used VOF to investigate droplet formation and found good agreement with the LBM simulations of Van der Graaf et al. (2006). They showed that the effect of contact angle on droplet size is not obvious for contact angles in excess of 165°. Rosengarten et al. (2006) used a VOF method to study the effect of wetting properties on the shape of a droplet as it moves through a contraction. They found that lower contact angles induced droplet breakup whereas at higher contact angles slugs formed in the contraction. The competitive wetting of the inner microchannel walls by two immiscible fluids can lead to irregular flow patterns, thus interfering with the uniform formation of droplets. De Menech et al. (2008) used a phase field method to investigate the dynamics of streams of immiscible fluids where a perfect wetting condition was taken for the continuous phase and it was assumed that the dispersed phase did not wet the walls. In this chapter we extend these earlier numerical studies by performing a detailed investigation of the effects of surface wettability, which can be controlled by altering the contact angle. We will examine the effects of contact angle for different flow rate ratios, viscosity ratios and interfacial tensions. The goal of this work is to further our understanding of the physics of droplet formation, and hence achieve better control over their generation.

Each of the above mentioned numerical methods have advantages and disadvantages. The level set method, used in this study, is advantageous in some respect over these methods. For instance, in the VOF method a discontinuous function (0 in one phase and 1 in the other) is used to identify the region

occupied by each phase. This discontinuity can lead to poor accuracy in determining the location of the interface. This can affect the calculation of the mean curvature which in turn can lead to errors in the surface tension force. In the level set method an interface is represented by a contour of a smooth function. According to Van der Graaf et al. (2006) variations in interfacial tension were difficult to simulate as this parameter cannot be set independently using LBM. This constraint can be overcome by the use of the two phase level set method which permits any value of interfacial tension to be chosen. Hence the effects of surface tension can be analyzed. The main drawback of LSM over LBM is that it is computationally more expensive. In the classical LSM, the main drawback is that mass is not conserved, and significant mass loss may occur. Olsson and Kreiss (2005) derived a mass-conserving LSM for the modeling of multiphase flows. For the simulations presented herein we used a modified LSM which possesses good mass conservation with better accuracy as compared to that of standard LSM.

In this chapter we define the droplet length by L_d. The droplet breakup time is taken to be the instant that the immiscible thread of the dispersed phase fluid detaches from the inlet channel. The time of formation of the stable droplets is taken to be the instant at which a droplet attains its final equilibrium shape. This does not occur instantaneously upon detachment as, particularly in the case of low hydrophobic contact angle, wall effects initially dominate for a longer time until they are exceeded by relative interfacial stresses. As the neck detaches from the inlet stream, interfacial forces increase rapidly due to a sudden increase in curvature as the droplet obtains its final stable form.

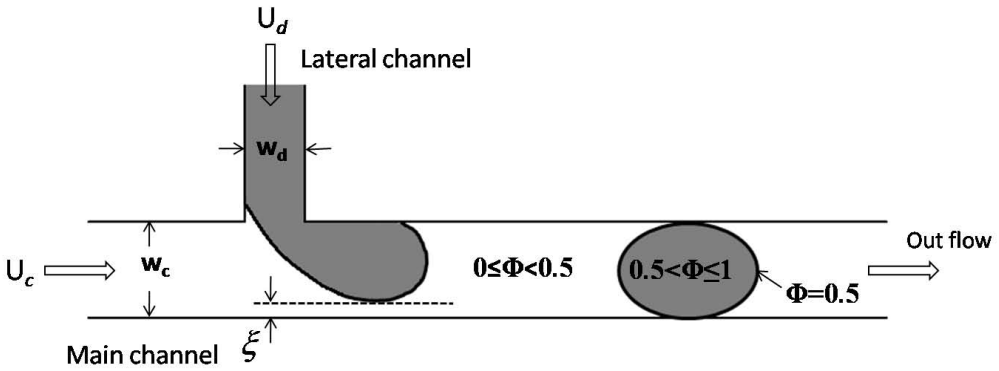

Fig 3.1. Schematic of the T-junction microchannel. The main horizontal channel contains the continuous phase (oil). The perpendicular inlet channel contains the dispersed phase (water).

3.2 Experimental procedure and equipment

This numerical study was motivated by our desire to produce monodisperse uniform droplets in the laboratory. Dimensions and parameters used in the numerical model were chosen to closely match those of our experimental system in order to facilitate comparison between data obtained and subsequent refinements of both the experiment and the model.

The microchips used in this study were produced in-house using photolithography. The width of the main channel is $w_c = 100$ μm and the width of the orthogonal channel is $w_d = 60$ μm. Note that subscripts c and d represent the continuous and dispersed phases respectively. The microchannel depth is 5 μm. The microchannels have inlet and outlet sections of around 10 mm in length, in which the flow is uniform and can therefore be approximated by analytical solutions if required. A schematic of the T-junction microchannel is shown in Fig. 3.1.

In the experimental study water is used as the dispersed phase and was de-

Table 3.1. Physical properties of liquids

Liquids	**Density** $\rho, (kg/m^3)$	**Viscosity** $\eta, (mPa.s)$
Water	1000	1.0
N-dodecane oil	750	1.34
Silicon oil (KF96-10)	935	9.4

livered through the perpendicular channel. N-dodecane oil was chosen for the continuous phase. Numerical simulations for model validation were based on N-dodecane oil (Fig. 3.2). However, some simulations based on silicon oil were also performed in order to simultaneously assess the effects of both viscosity and contact angle on droplet formation. Silicon oil was chosen as an example of a carrier fluid that is much more viscous than N-dodecane oil (Table 3.1). In the experiment the oil completely wetted the hydrophobic walls of the main microchannel (however, the numerical model readily permitted the effects of wetting on droplet formation to be studied). Both liquids were fed into the channels on the microchip through high precision syringe pumps. Droplet formation at the T-junction was observed using a microscope and images were recorded using a high speed CCD camera.

The dimensionless parameters other than capillary number considered are the flow rate ratio $Q = Q_d/Q_c$, the viscosity ratio $\lambda = \eta_d/\eta_c$ and the continuous phase Reynolds number $Re_c = \rho_c U_c w_c/\mu_c$. The flow velocities of the dispersed and continuous phases, U_d and U_c, can be described in terms of flow rates as $U_d = Q_d/w_d$ and $U_c = Q_c/w_c$. For all studies presented in this chapter the water flow rate is always held fixed, i.e. $U_d = 0.012$ ms^{-1}.

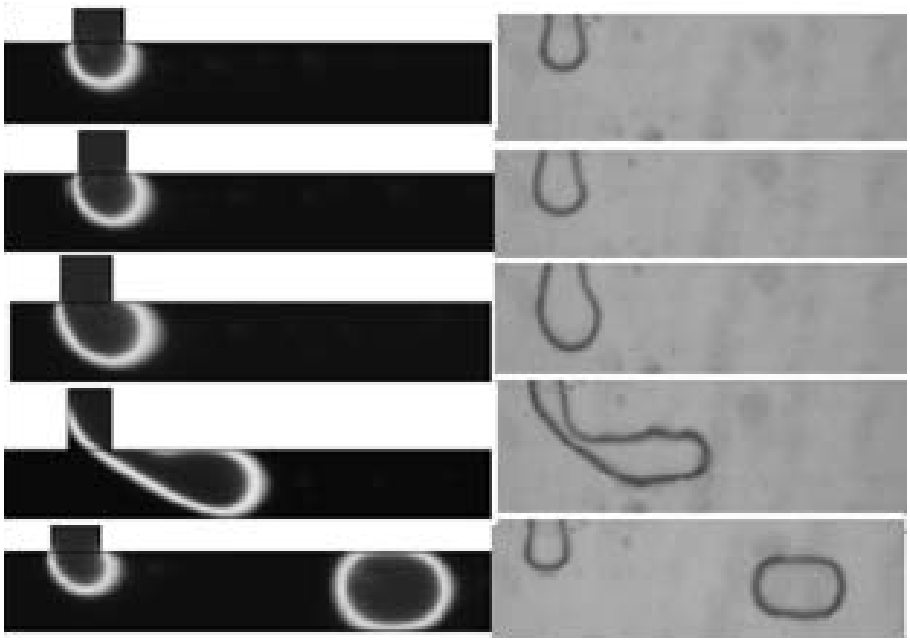

Fig 3.2. Comparison of water droplet breakup process in N-dodecane oil using (a) level set method (lefthand images) and (b) experiment (righthand images). Velocity of the water droplets is kept fixed at $U_d = 0.012$ ms^{-1}. The capillary number $Ca = 0.01$. Each pair of images correspond to the same time interval from the initiation of droplet formation.

3.3 Model description

3.3.1 The level set method

Several numerical techniques have been developed for tracking time-varying objects such as the interface between two immiscible fluids (e.g. the VOF method and the level set method), all of which have individual advantages and disadvantages. The level set method was developed in the 1980s (Osher et al., 1988). It permits numerical computations of such objects to be performed on a fixed Cartesian grid without having to parameterize them. It is a robust scheme that is relatively easy to implement. The principle on which is based is

the assignment of a so-called level set function $\phi(\mathbf{x}, t)$ to the space occupied by an interface, where $\mathbf{x}$ denotes the co-ordinates of a point within that space at a time t. The function is initialized at time t_0, and then a numerical scheme is used to approximate the value of $\phi(\mathbf{x}, t)$ over small time increments, thus enabling the propagation of the interface to be tracked in time.

In the originally proposed level set method $\phi(\mathbf{x}, t)$ is defined as signed distance function. The interface is represented by the zero contour of the level set function ϕ. $\phi > 0$ on one side of the interface and $\phi < 0$ on the other.

In the present study we have used the conservative level set method proposed by Olsson and Kreiss (2005). The level set function is chosen such that the position of the water-oil interface is described by the 0.5 contour of the level set function ϕ. The main channel is filled with the continuous phase (oil) and the dispersed phase (water) is placed in the inlet channel as shown in Fig. 3.1. For the continuous phase $\phi = 0$, and for the dispersed phase $\phi = 1$.

3.3.2 Governing equations

The governing equations consist of the incompressible Navier-Stokes Eq. 3.1 and continuity Eq. 3.2, coupled with the level set Eq. 3.3 for the advection of the level set function ϕ.

$$\rho\frac{\partial \mathbf{u}}{\partial t} + \rho(\mathbf{u}.\nabla)\mathbf{u} = \nabla.[-p\mathbf{I} + \eta(\nabla\mathbf{u} + (\nabla\mathbf{u})^T)] + \sigma\kappa\delta\mathbf{n}, \tag{3.1}$$

$$\nabla \cdot \mathbf{u} = 0, \tag{3.2}$$

$$\frac{\partial \phi}{\partial t} + \mathbf{u} \cdot \nabla\phi = \gamma\nabla \cdot \left(\epsilon\nabla\phi - \phi(1-\phi)\frac{\nabla\phi}{|\nabla\phi|}\right), \tag{3.3}$$

where ρ is the density, η is the dynamic viscosity, σ is the surface tension coefficient, δ is the dirac delta function concentrated at the interface between the two fluids. p denotes pressure, $\mathbf{I}$ is the identity matrix and $\mathbf{n}$ is the unit normal vector to the interface pointing into the droplet. γ and ϵ are numerical stabilization parameters such that ϵ determines the thickness of the interface and γ is the reinitialization parameter. The first term on the right side, that is the divergence of $\epsilon\nabla\phi$, acts as an artificial diffusivity in order to prevent discontinuities at the interface. The second term on the right is described as a compressive flux (Olsson and Kreiss, 2005).

The curvature of the fluid-fluid interface, κ, can be defined as

$$\kappa = -\nabla \cdot \mathbf{n}, \tag{3.4}$$

where $\mathbf{n}$ can be written in terms of the level set function as

$$\mathbf{n} = \frac{\nabla\phi}{|\nabla\phi|}. \tag{3.5}$$

The term $\sigma\kappa\delta\mathbf{n}$ in Eq.(3.1) defines the surface tension force acting on the interface between two fluids.

Eqs. 3.1 and 3.2 are solved to obtain the velocity field $\mathbf{u}$ which is then used in Eq. 3.3 for the advection of the level set function (Deshpande and Zimmerman, 2006; Zimmerman, 2006). The level set function ϕ is used to smooth the fluid properties across the interface as follows:

$$\rho = \rho_c + (\rho_d - \rho_c)\phi, \tag{3.6}$$

$$\eta = \eta_c + (\eta_d - \eta_c)\phi. \tag{3.7}$$

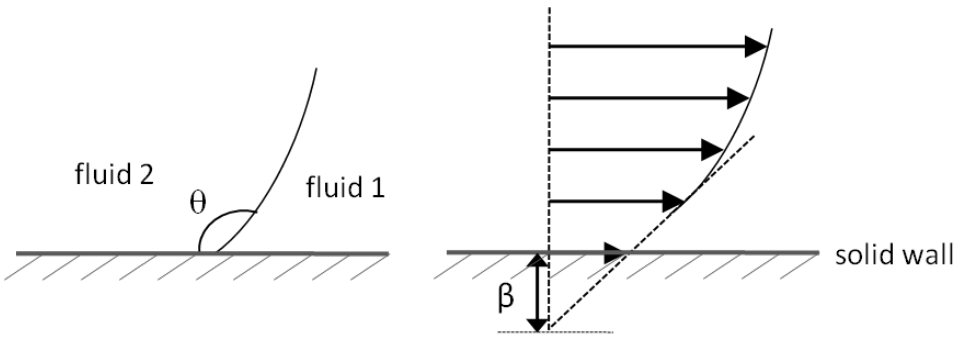

Fig 3.3. (a) Contact angle θ (b) Slip length β.

This smoothing minimizes numerical oscillations in the solution of the Navier-Stokes equations. The equations were solved using the level-set two-phase flow application mode of the commercially available software package COMSOL Multiphysics®. In the implementation of two phase flow in Comsol Multiphysics, the wetted wall boundary condition requires the user to define the slip length β and the contact angle θ. The slip length β is a measure of slip, which is defined to be the distance behind the wetted wall where the fluid velocity can be extrapolated to zero and is suggested to take a value equal to the mesh size (Comsol, 1994). It is defined in terms of the frictional force, $\mathbf{F}_{fr}$ as

$$\mathbf{F}_{fr} = -(\eta/\beta)\mathbf{u}. \tag{3.8}$$

The contact angle θ is the angle between fluid-fluid interface and the solid wall. It is employed as:

$$n.n_{interface} = \cos(\theta). \tag{3.9}$$

where $n_{interface}$ is the vector normal to the interface.

As the two fluids are immiscible the model assumes that almost no particle of one fluid is present in the other fluid. Therefore, in particular there is no mass

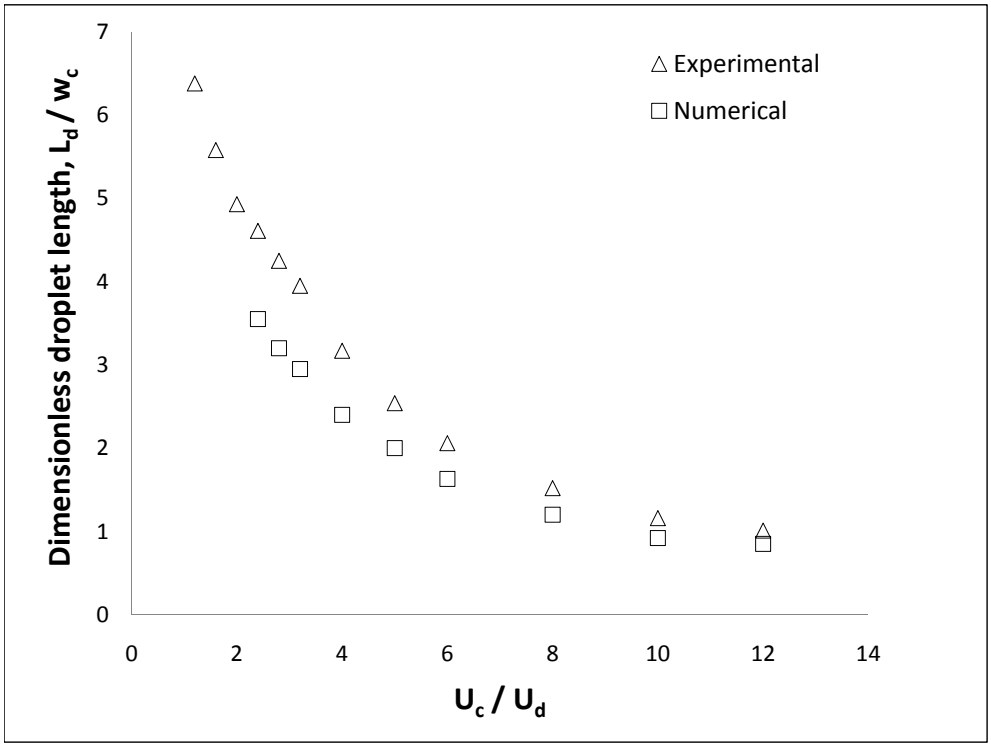

Fig 3.4. Comparison of the droplet length between numerical simulations and experimental results for different flow velocity ratios.

transfer across the interface. Hence the velocities are equal at the interface. Moreover, the force balance at the initial fluid interface (boundary condition) is defined in this model as,

$$[-P\mathbf{I} + \eta(\nabla\mathbf{u} + \nabla\mathbf{u}^{\mathbf{T}})]\mathbf{n} = \mathbf{0}. \tag{3.10}$$

3.4 Numerical simulations and model validation

Numerical simulations of the formation of water droplets in oil in a T-junction microchannel are presented. Simulations were carried out using the two phase

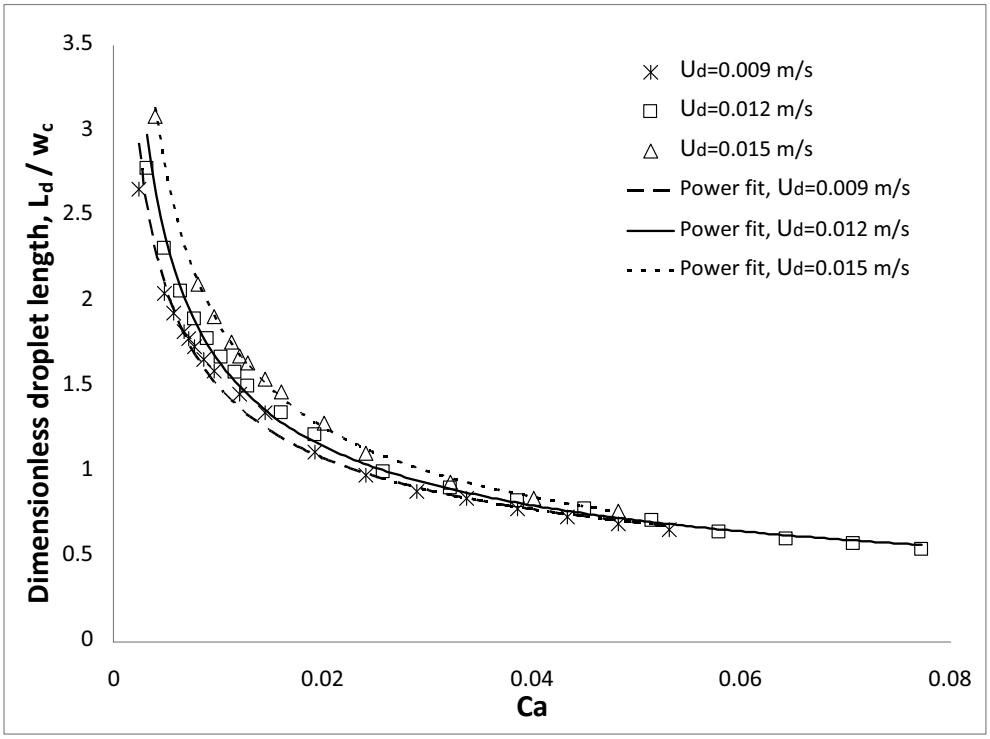

Fig 3.5. The influence of capillary number on dimensionless droplet length at dispersed phase flow velocities U_d of 0.009 ms^{-1}, 0.012 ms^{-1} and 0.015 ms^{-1} respectively. The lines represent a power law fit: $L_d/w_d = 0.170Ca^{-0.47}$, $L_d/w_d = 0.150Ca^{-0.52}$ and $L_d/w_d = 0.136Ca^{-0.56}$ to the predicted results correspondingly. For each simulation λ=0.8.

level set method (LSM) and were found to give qualitative agreement for droplet size versus flow ratios U_c/U_d when compared with the laboratory experiments (Fig. 3.4.) The droplet sizes in the experiment were measured by counting pixels in images from a CCD camera. From both experimental and numerical results it is predicted that droplet size decreases as U_c/U_d increases. The results are also in satisfactory agreement with previous findings (Nisisako et al., 2002; Thorson et al., 2001).

Droplet sizes predicted from the level set simulations are smaller than those obtained from the experiment for low values of U_c/U_d. However, at higher flow ratios this difference decreases as the degree of confinement reduces at higher

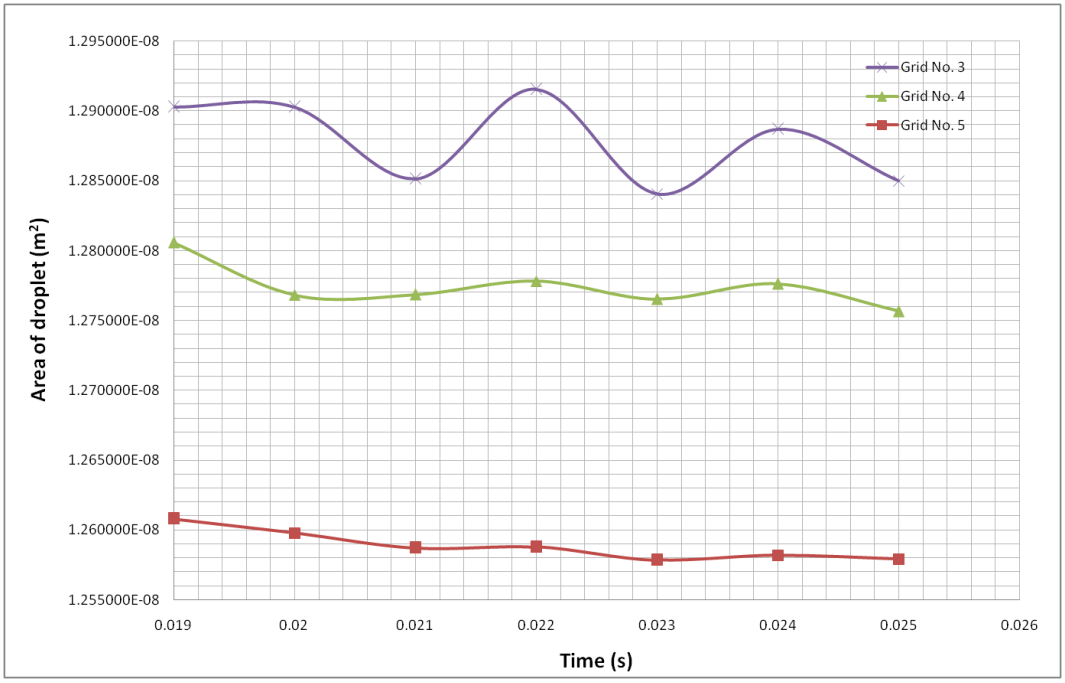

Fig 3.6. Mass conservation of droplet area corresponding to different grid sizes.

flow velocities of the continuous phase fluid. It is possible that some variation in physical properties of the experiment (e.g. small fluctuations in temperature or flow speed, or channel walls that are not perfectly straight) may have contributed to the deviation between simulated and observed droplet sizes. The roughness of the channel downstream might also affect the length of larger droplets or plugs. Also, it was assumed in the experiment that the flow rate remains unchanged from the point of injection of the liquid at the syringe through to the inlet of microchannel. Although the roughness effects are practical complexities, however the mathematical model assumes the microchannel walls as smooth surfaces and hence does not include these rough surface effects which cause the deviation of the numerical results from experimental observations.

Profiles of dimensionless droplet length versus Ca shown in Fig. 3.5 were obtained from numerical simulations with a viscosity ratio $\lambda = 0.8$. (This ratio

was chosen for initial simulations as it is close to the value consistent with the formation of water droplets in a carrier fluid of N-dodecane oil.

In section 3.5 we will also present results from simulations using $\lambda = 0.1$, consistent with a more viscous carrier oil, e.g. silicon oil.) The simulated profiles are consistent with findings from other numerical studies (Van der Graaf et al., 2006) and experimental studies (Husny and Cooper-White, 2006; Nisisako et al., 2002). Note that the flow velocity of water was held constant at U_d =0.012 ms^{-1} throughout these simulations. Furthermore, the value of the critical capillary number for distinguishing between the squeezing and dripping regimes was found to be 0.019. This critical value of Ca was difficult to identify in the experiments performed by Christopher et al. (2008) as they considered a much smaller viscosity ratio of 0.01. At such a small viscosity ratio the detachment point always occurs downstream from the corner of the T-junction. This effect will be explained later in section 3.5.

The accuracy of the numerical scheme was assessed by means of a grid convergence study (see Appendix). Convergence of one of the key measures, the droplet breakup time, to three significant figures was achieved for grid meshes containing 2926 elements or more. The numerical error in mass conservation of droplet area, $A = \int_{\phi>0.5} d\Omega$, for the final grid considered is 0.01% (Fig. 3.6). Simulations were performed using a timestep of 0.0005 s.

3.5 Results

3.5.1 Effect of contact angle on size and generation rate of droplets

Due to the high surface-to-volume ratios that are characteristic of microchannel flows, surface effects play a key role in droplet formation. The surface of the microchannel directly affects the droplet formation process as it determines the magnitude of the wettability. The contact angle determines the characteristics of the interaction of the droplet with the channel wall. It affects the droplet formation process as it influences the ease with which a droplet forms and propagates downstream, and it influences the shape of a droplet.

In the process of droplet formation the continuous phase fluid should wet the channel wall in order to break the dispersed phase fluid into stable droplets consistently. The interaction between water molecules and the solid wall of the microchannel decreases as the contact angle (θ) gets larger (Haynes et al., 1968). Hence, we can model the effects of changing the wetting properties of the channel walls by altering θ in the numerical model. If the carrier fluid perfectly wets the channel walls then water droplets will develop out of the junction without spreading along the surface of the main channel and will stabilize. The minimum length of the droplets achieved by Garstecki et al. (2006) in their experiment was equal to the width of the continuous phase channel ($L_d \approx w_c$). They concluded that this lower limit to droplet length suggests a strong dependency of the breakup process on the geometry of the device. Here, we will probe further into this concept by investigating the dependence of droplet size and generation

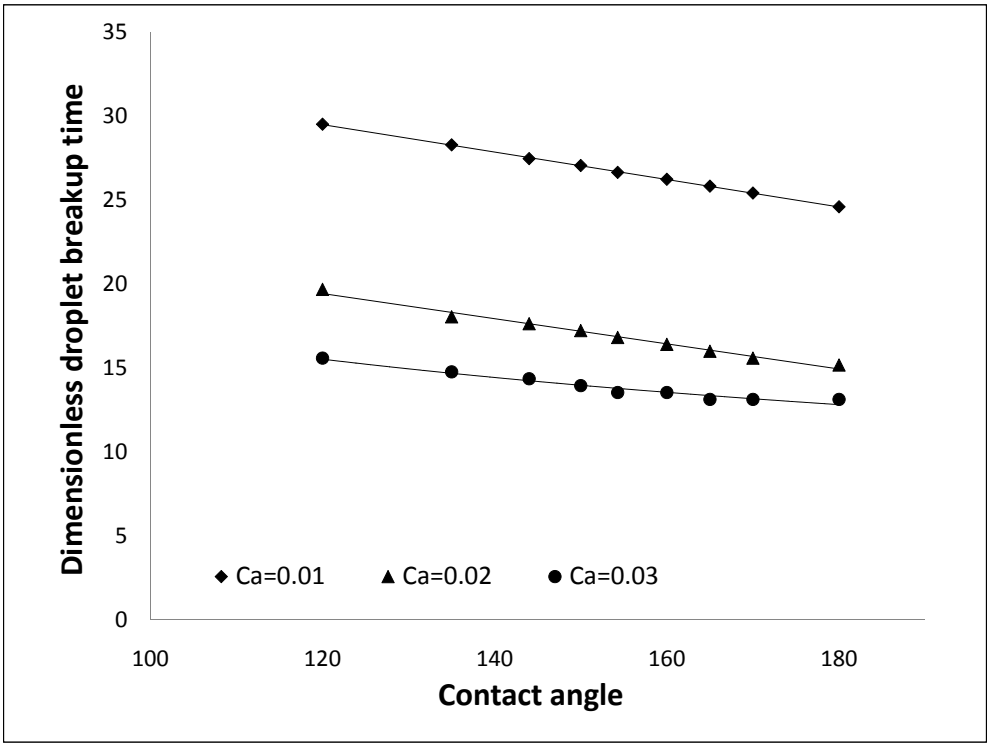

Fig 3.7. Effect of contact angle on droplet breakup time for capillary numbers of 0.01, 0.02 and 0.03. Corresponding flow rate ratios are 0.2, 0.1 and 0.05, and Reynolds numbers (Re_c) are 2.4, 4.7 and 7.1 respectively. U_d =0.012 ms^{-1}, σ=5 mNm^{-1} and λ=0.8. Time is rescaled by U_c/w_c.

rate with contact angle. The contact angle of water droplets with the channel walls was varied from 120° to 180°. This range of contact angles extends over the regime for hydrophobic surfaces incorporating partial wetting through to complete wetting of the channel surface with oil (Dreyfus et al., 2003). In our simulations we have taken $Q_c > Q_d$ in order for droplet detachment to occur at the junction (Nisisako et al., 2004; De Menech et al., 2008; Peng et al., 1998; Husny and Cooper-White, 2006).

It can be predicted from Figs. 3.7 and 3.8 that the droplet breakup time (the period of droplet formation) decreases as the contact angle increases from 120° to 180°. We can also interpret this as the frequency of droplet formation in-

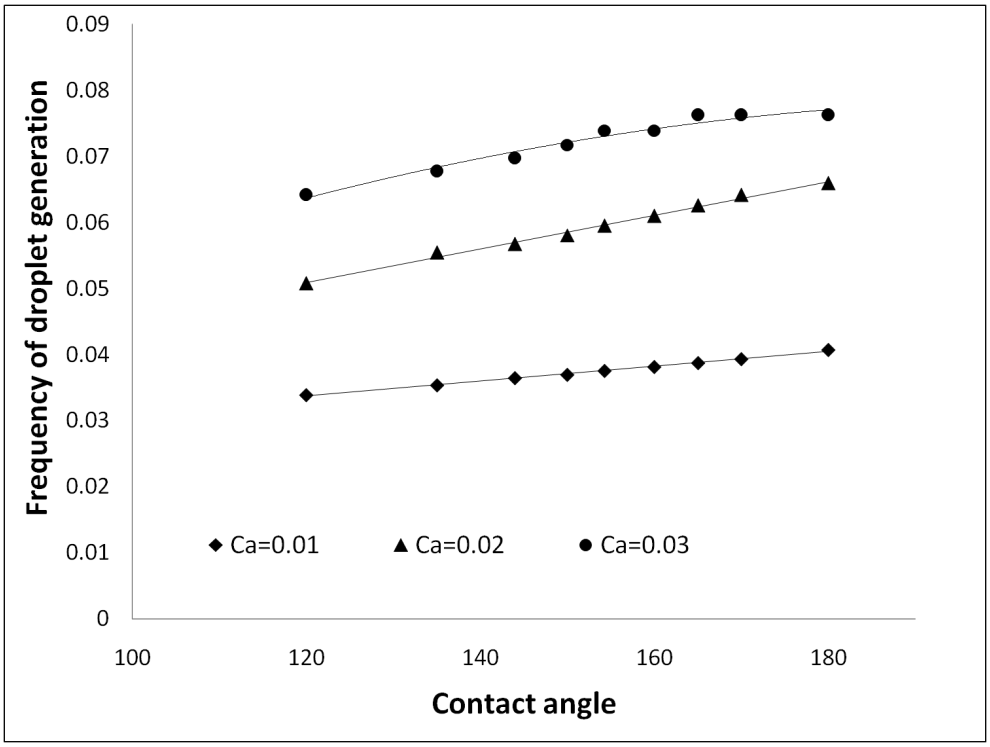

Fig 3.8. Effect of contact angle on non-dimensional frequency of droplet generation for capillary numbers of 0.01, 0.02 and 0.03. Corresponding flow rate ratios are 0.2, 0.1 and 0.05, and Reynolds numbers (Re_c) are 2.4, 4.7 and 7.1 respectively. U_d =0.012 ms^{-1}, σ=5 mNm^{-1} and λ=0.8. Frequency is rescaled by w_c/U_c.

creases with the contact angle. This effect was predicted for all three capillary numbers considered. The flow in a microchannel becomes faster as the surface contact angle is increased. This is because the overall resistance to flow decreases due to a reduction in the adhesive forces on the channel walls. This phenomenon allows us to explain why the predicted droplet breakup occurs at earlier times as the contact angle is increased. For larger contact angles the elongated immiscible thread of the dispersed phase moves faster at the junction due to the reduced resistance to the flow. Consequently, the thread separates away from the inlet stream more quickly compared to the situation for lower contact angles.

The effect of wall contact angle on droplet length for different values of Ca is shown in Fig. 3.9. For the highest value of Ca considered, i.e. 0.03, which falls within the shearing regime, the droplet length is essentially independent of the contact angle due to the shear force dominating over the adhesive force of the channel walls, thus reducing the degree of confinement of the droplet. However, as Ca is decreased, a growing dependency of droplet length on contact angle is predicted. This is particularly marked for the case of $Ca = 0.006$ for contact angles between $120°$ and $150°$. For small values of Ca, the droplet generated has a relatively large contact area with the channel walls. Consequently wall surface adhesive forces play a significant role during droplet formation. In the superhydrophobic regime, where the contact angle is greater than about $165°$, the droplet length remains roughly constant for all Ca values considered. Sang et al. (2009) studied the droplet formation of 1, 6-hexanediol diacrylate in polyvinyl aqueous solution using the VOF method and also found that increasing the contact angle in excess of $165°$ had a negligible effect on droplet length.

3.5.2 Combined effects of viscosity of carrier fluid and contact angle

A schematic view of a microdroplet is shown in Fig. 3.10, with the advancing and receding contact angles, θ_a and θ_r, labeled. The combined effects of carrier fluid viscosity and contact angle were examined by considering the two aforementioned carrier oils with $\lambda = 0.8$ and $\lambda = 0.1$. The lefthand images in Fig. 3.11 show numerical simulations of the droplet at the instant of detachment for contact angles of $120°$ (top), $150°$ (middle) and $180°$ (bottom). The

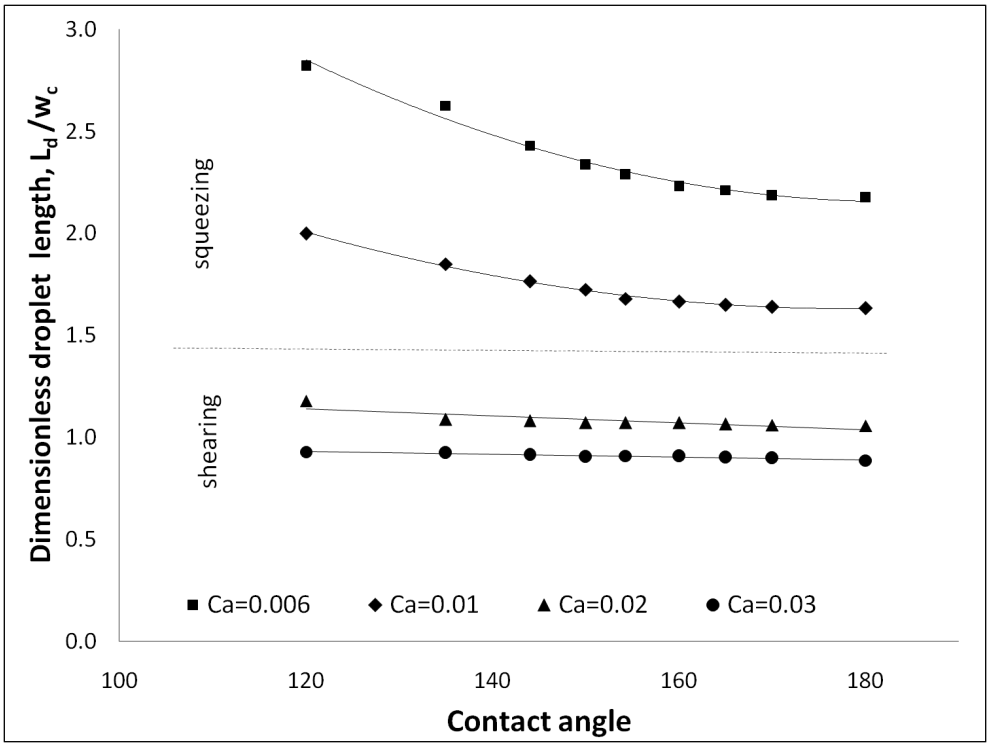

Fig 3.9. Effect of contact angle on droplet length for capillary numbers of 0.006, 0.01, 0.02 and 0.03. Corresponding flow rate ratios are 0.3, 0.2, 0.1 and 0.05, and Reynolds numbers (Re_c) are 1.7, 2.4, 4.7 and 7.1 respectively. U_d =0.012 ms^{-1}, σ=5 mNm^{-1} and λ=0.8.

righthand images show the corresponding droplets at a downstream position once they have become stable. Table 3.2 shows the time taken for the droplet to detach, and also the time taken for the droplet to become stable (measured from the time that the water was introduced into the main channel). For both carrier oils considered, the droplet length decreases as the contact angle, θ, increases. This is due to the fact that the increase in contact angle accelerates the overall flow in the microchannel as its walls provide less resistance. The penetration length of the oil from the main channel into the water phase in the inlet channel increases correspondingly. Consequently, the droplet breakup time is decreased and smaller droplets are produced. In the case of the lower

Table 3.2. Time taken for detachment and for formation of stable water droplets.

Viscosity ratio (λ)	**Contact angle** (θ)	**Detachment time** (s)	**Time of formation for stable droplet (s)**	**Droplet length** (microns)
0.8	120°	0.026	0.031	200
	150°	0.022	0.027	169
	180°	0.0205	0.0255	163
0.1	120°	0.015	0.02	113
	150°	0.0135	0.0185	104
	180°	0.013	0.018	99

Fig 3.10. Schematic view of droplet in a microchannel with advancing contact angle (θ_a) and receding contact angle (θ_r).

viscous carrier oil with $\lambda = 0.8$, the resulting droplets produced possess a line of symmetry perpendicular to the length of the channel, that is, the advancing and receding contact angles of the droplets formed are similar (Fig. 3.11(a)). At small values of θ in the hydrophobic regime the curvature of the interfaces becomes small, and hence the interfaces become approximately normal to the length of the channel. For the case of $\lambda = 0.1$ (Fig. 3.11(b)) the droplet shapes are different to those produced with the lower viscosity carrier fluid considered. This phenomenon is particularly marked for a contact angle of 120°. The droplets formed lack the symmetry predicted in those for $\lambda = 0.8$, the advancing contact angle θ_a now being greater than the receding contact angle θ_r. Thus the advancing front has more contact with the surface than the receding one. This prediction is in line with the theory of contact angle hysteresis (Kamusewitz and Possart, 2006).

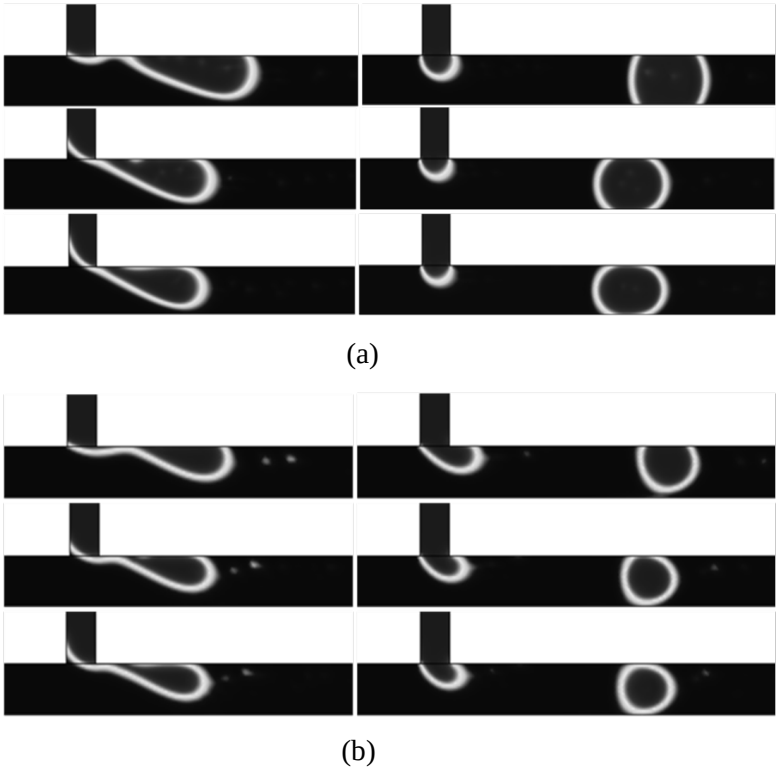

Fig 3.11. Effect of contact angle on droplet formation and sizes for (a) oil with low viscosity ($\lambda = 0.8$) and (b) oil with high viscosity ($\lambda = 0.1$) with U_d=0.012 ms^{-1} and σ=5 mNm^{-1}. $\theta = 120°, 150°$ and $180°$ respectively from top to bottom for both (a) and (b). For each contact angle the lefthand figure illustrates the droplet detachment point and the righthand figure depicts the formed droplet. The elapsed time between each lefthand image with the corresponding righthand image is 5 ms.

For the case where $\theta = 120°$, the detachment point has moved in the downstream direction. The smaller droplet lengths predicted in the case of $\lambda = 0.1$ compared to those predicted for $\lambda = 0.8$ are due to the relative increase in the cross-flow shear force over the interfacial force at the channel junction.

In order to examine the combined effects of the viscosity of the carrier fluid and contact angle on drop size quantitatively, we have plotted droplet length against contact angle in Fig. 3.12 for $\lambda = 0.1$ and $\lambda = 0.8$. The droplet length shows a larger increase as contact angle decreases in the case of $\lambda = 0.8$ compared with

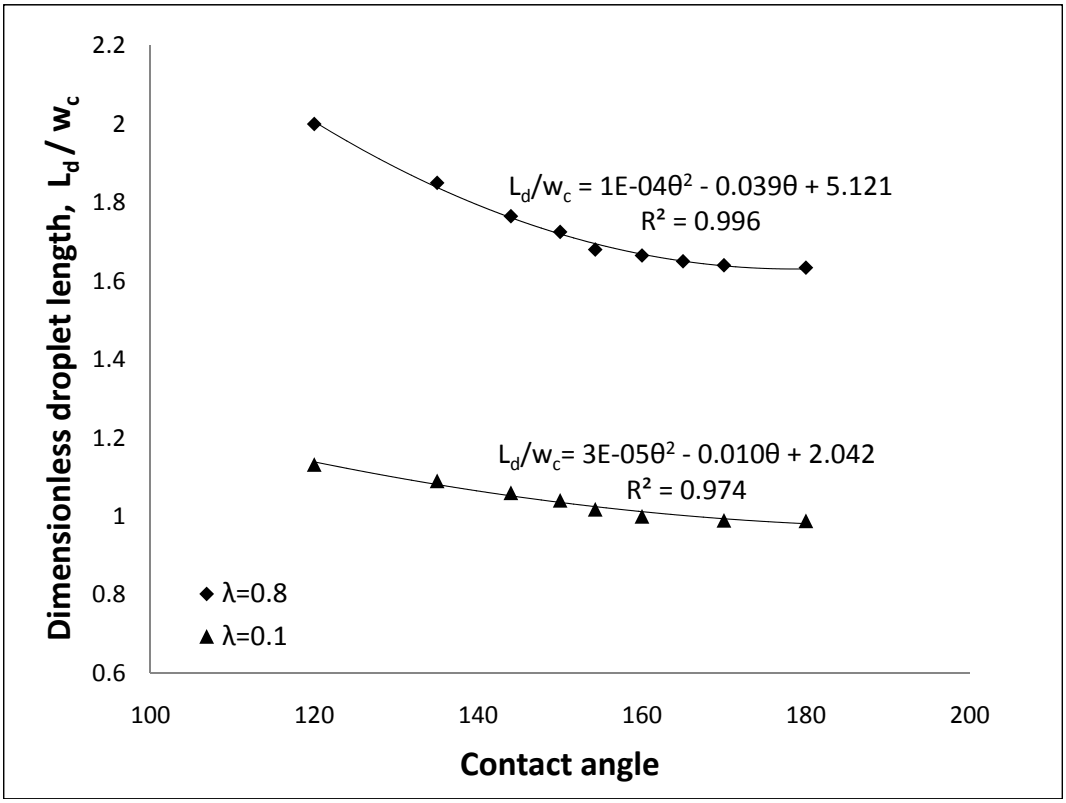

Fig 3.12. Effect of contact angle on droplet length for $\lambda = 0.1$ and $\lambda = 0.8$. $U_d = 0.012$ ms^{-1} and σ=5 mNm^{-1}. For the lower viscosity carrier oil ($\lambda = 0.8$): $Ca = 0.01$, Re=2.4. For the higher viscosity carrier oil ($\lambda = 0.1$): $Ca = 0.08$, Re=0.4. R^2 is the goodness of fit parameter for the quadratic.

$\lambda = 0.1$. In the case of the less viscous oil, droplet sizes were found to decrease quadratically with the contact angle. In the case of the higher viscosity oil this decrease was closer to linear as the coefficient of the θ^2 term in the fitted curve is $O(10)$ smaller.

3.5.3 Effect of interfacial tension

Interfacial tension plays an important role in influencing the breakup and stability of droplets in microchannels. This is the only conservative force which keeps the droplet attached at the junction (i.e., it acts so as to resist the de-

tachment of the droplet from the incoming dispersed phase stream), therefore an equilibrium of forces is reached earlier at lower values of interfacial tension, resulting in faster droplet formation and hence the droplet length gets smaller. Interfacial tension at a fluid-fluid interface may introduce strong nonlinearities into the flow (De Menech et al., 2008). It could, therefore, have a significant effect on microdispersion processes at the T-junction. One of the key benefits of the level set method for modeling droplet formation over LBM, for example, is that it is possible to perform simulations where the interfacial tension, σ, is explicitly controlled by altering the relevant model parameter. Fig. 3.13 shows the effect of the water-oil interfacial tension on the droplet length for three different values of flow rate ratios which are obtained by altering the flow velocity of carrier oil. The simulations predict that droplet size increases as the interfacial tension is increased. This increase in droplet length is particularly marked at lower values of interfacial tension of around 0.002 Nm^{-1} in case of $Q = 0.2$.

At low Ca shear forces alone may not be sufficient to break off the droplet and the role of interfacial tension forces will become significant. For lower values of σ (interfacial tension) the pressure drop across the droplet may not be sufficient to cause the droplet to detach at the junction as the incoming dispersed phase stream elongates for some distance downstream (typically at a location two or three times the width of the main channel, w_c), before it breaks off. This elongation is greater for more viscous carrier oils as interfacial elasticity and viscous drag both cause breakup to occur further downstream. In Fig. 3.14 we compare the influence of interfacial tension on droplet length for viscosity ratios of $\lambda = 0.1$ and $\lambda = 0.8$. For both viscosity ratios considered the droplet length is a function of $\ln \sigma$. In the case of $\lambda = 0.1$ the viscous forces are strong enough

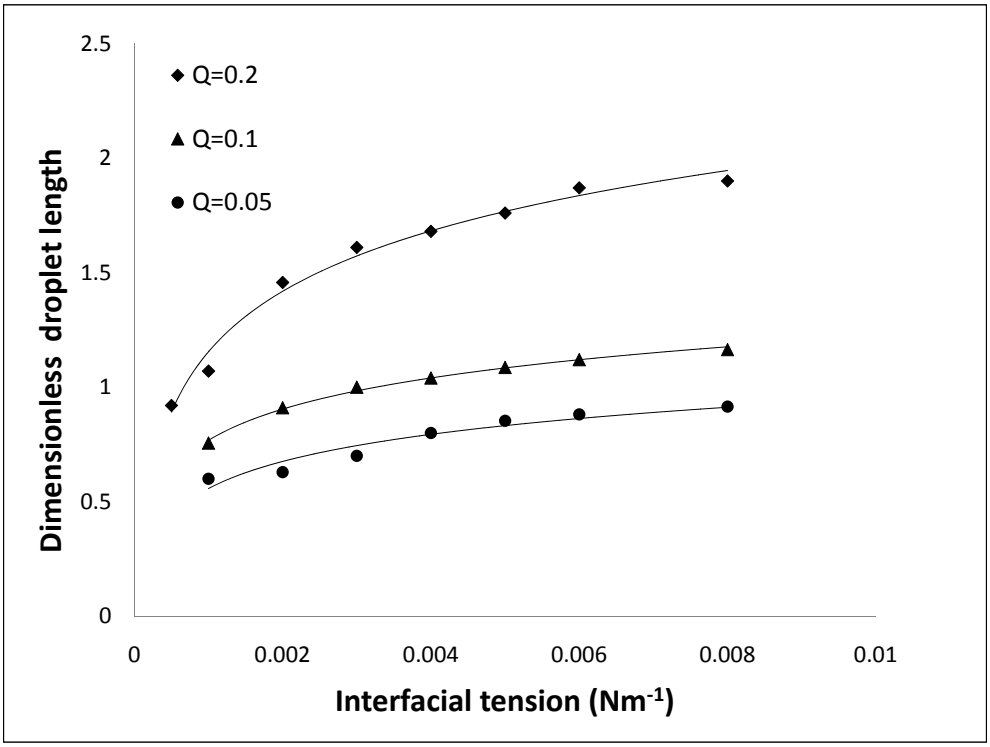

Fig 3.13. Effect of interfacial tension on droplet length for for flow rate ratios of $Q = 0.05$, 0.1 and 0.2. $U_d = 0.012$ ms^{-1}, $\lambda = 0.8$ and $\theta = 144°$

to compete with the surface tension forces. Breakup time (at a particular value of interfacial tension) occurs earlier when compared to that for $\lambda = 0.8$. The droplet generation frequency increases correspondingly. Thus at a specified value of σ the length of water droplets in the more viscous carrier oil is less than those in the less viscous oil. For the case of λ=0.8, where the viscous forces applied on the droplet are less strong, interfacial forces tend to delay the instant of breakup, resulting in the formation of larger droplets. At higher values of $\sigma(\sigma > 0.008\text{Nm}^{-1})$, breakup occurs immediately at the junction due to a build up of high pressure upstream of the droplet in the continuous phase as a result of an increased degree of confinement of the droplet in the microchannel.

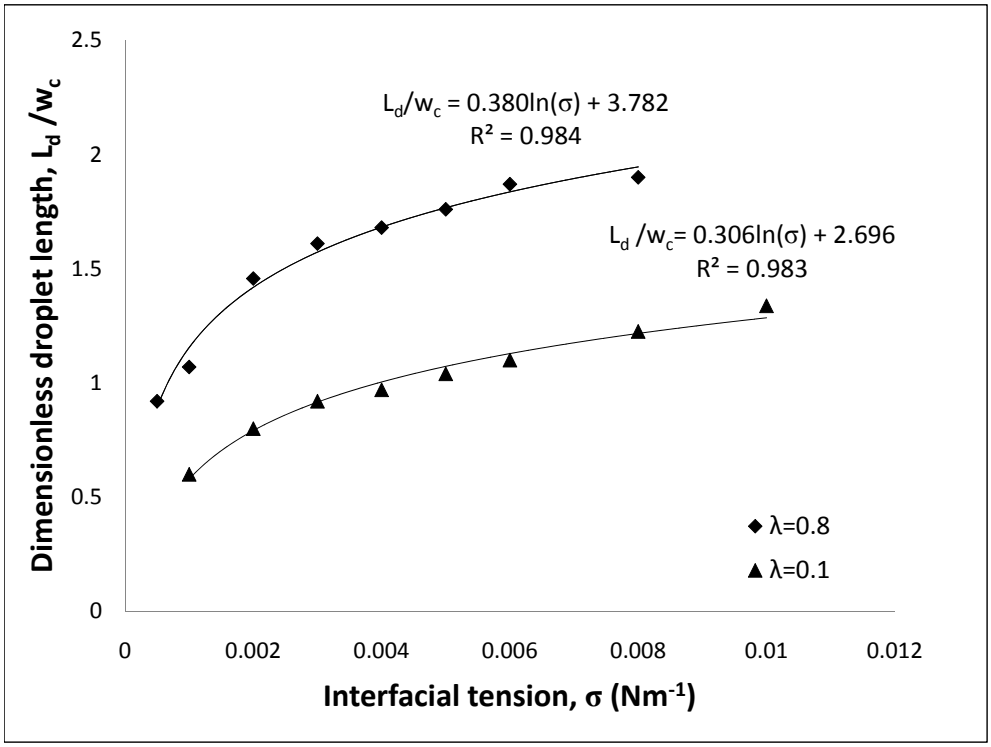

Fig 3.14. Effect of interfacial tension on droplet length for viscosity ratios $\lambda = 0.1$ and $\lambda = 0.8$ for fixed values of $Q = 0.2$, $U_d = 0.012$ ms^{-1} and $\theta = 144°$.

3.6 Conclusions

Numerical simulations of the formation in a microchannel T-junction of aqueous droplets in an oil-based continuous phase have been carried out using a conservative two phase level set method. The model was validated by comparison with laboratory experiments and also gave results consistent with numerical studies of droplet formation from the literature. Detailed understanding of the physical processes affecting droplet formation is desirable since the production of uniform, regular droplets has many applications in microprocess engineering, for example, for the production of biological molecules.

The particular focus of this study was to examine the effects of wettability of

the channel walls on droplet formation. This is of importance as if the carrier fluid does not completely wet the channel walls due to competition from the dispersed phase, irregularities are predicted in droplet formation.

The conclusions from this study can be summarized as:

1 Droplet breakup time decreases approximately linearly with contact angle. Conversely, the frequency of droplet generation increases as the contact angle increases from 120° to 180°.

2 For capillary numbers greater than about 0.02, the effect of changing the contact angle has negligible effect on droplet size. However, for capillary numbers less than 0.02, the influence of contact angle becomes increasingly significant, particularly for angles corresponding to the region of hydrophobic wetting.

3 The numerical simulations predicted that the droplets possess a line of symmetry perpendicular to the length of the channel in case of $\lambda = 0.8$. However, if the viscosity of the carrier fluid is of order 10-fold greater than that of the dispersed phase, then the droplets produced lose their symmetry, the advancing contact angle now being greater than the receding contact angle.

4 Droplet length increases for higher values of interfacial tension. At a given value of interfacial tension, the droplet length is greater for the higher value of viscosity ratio considered ($\lambda = 0.8$) than for $\lambda = 0.1$.

5 The increase in droplet length with interfacial tension, σ, is a function of $\ln \sigma$, where the coefficients of the regression curves depend on the value of the viscosity ratio.

Appendix

A grid convergence test was performed to assess the resolution fidelity. The effect of mesh size was evaluated by increasing the number of elements from 1374 to 3559 as shown in Table 3.3.

Table 3.3. Mesh statistics for grid convergence test.

Grid No.	No. of elements	Degrees of Freedom	Droplet length (microns)	Relative % error
1	1374	9551	172.69875	2.91253
2	1498	10399	167.66884	2.00922
3	1757	12135	164.30000	1.66057
4	2102	14437	161.57168	1.23186
5	2461	16830	159.58135	0.73898
6	2926	19933	158.40208	0.41201
7	3559	24156	157.74945	

The dependence of droplet breakup time on the number of mesh elements is shown in Fig. 3.15. Consistent values are obtained for the finest two meshes considered. It was predicted that the interfaces are contorted on the coarsest grid but are more accurate on the finer grids for which the droplet shapes are geometrically more similar (Fig. 3.16). As the number of mesh points was increased, the predicted relative error in droplet length reduced, achieving an acceptable level of 0.4% in the case of grid number 6.

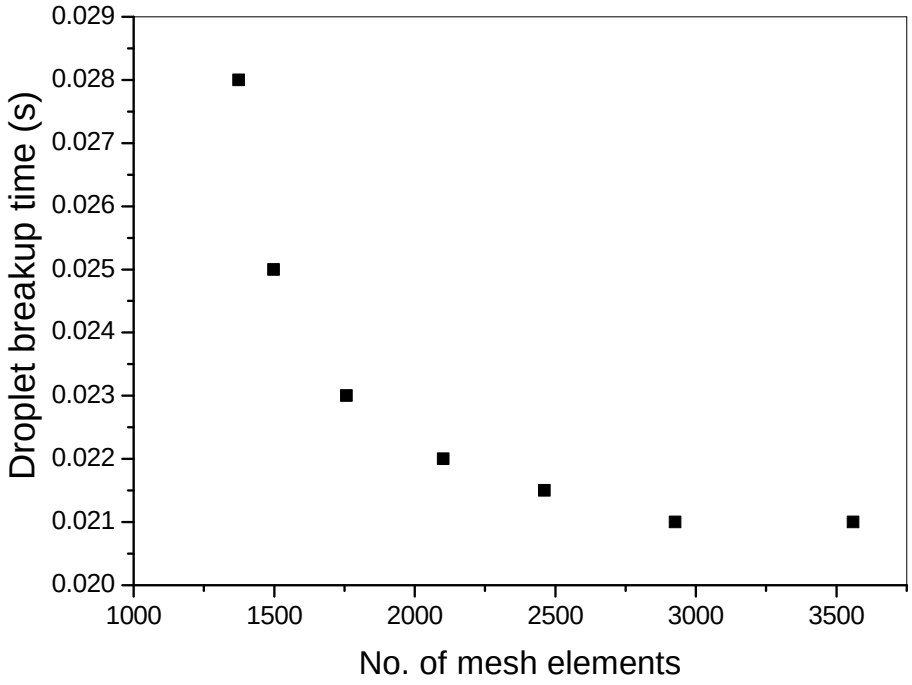

Fig 3.15. Results from grid convergence study showing the dependence of the droplet breakup time on the number of mesh elements.

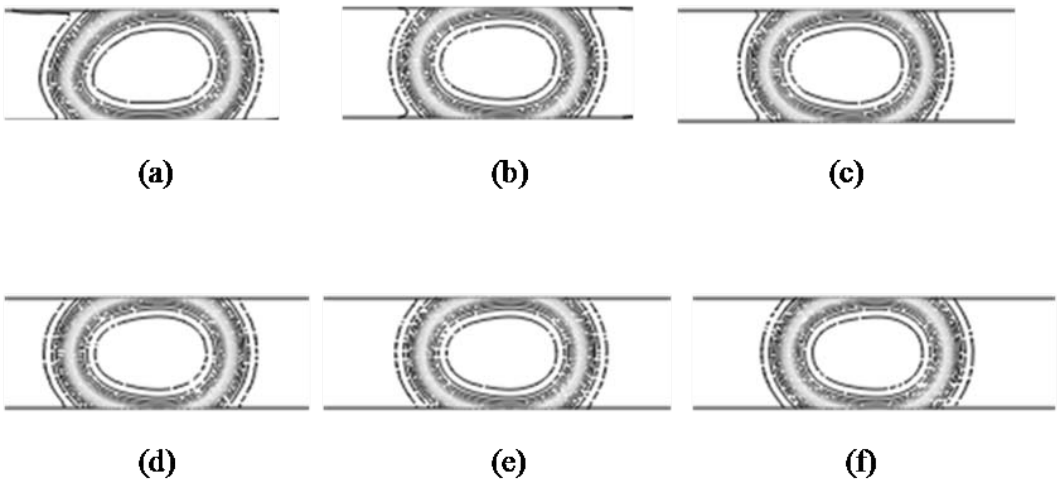

Fig 3.16. Contours of droplets formed using different grid meshes (a) 1 (b) 2 (c) 3 (d) 4 (e) 5 (f) 6, as defined in Table 3.3.

4

Investigation of pressure profile evolution during confined microdroplet formation using a two-phase level set method

The formation of droplets at a T-junction in a microchannel network is primarily influenced by the pressure difference across the interface in the squeezing regime. Accurate measurements of droplet velocity and pressure profiles are difficult to obtain experimentally, yet these are the basic parameters required for understanding the physics governing the droplet formation process and for shaping the optimum design of microfluidic devices. The current work presents predictions from numerical simulations of microdroplet generation at a T-junction. Detailed profiles of the predicted pressure evolution across the channel upstream of the T-junction indicate that the pressure variation is sensitive to small changes in the wetting properties of the continuous phase. This result is significant as due to limitations of fabrication processes, it can never be expected for a contact angle to be exactly 180° in microfluidic devices.

4.1 Introduction

Precise control of the generation of droplets is desirable in droplet-based microfluidics, providing our motivation for better understanding the dynamics of the droplet formation process. Droplet formation process can be characterized into three main regimes: squeezing, dripping and jetting (De Menech et al., 2008). The squeezing regime occurs at low values of the continuous phase capillary number ($Ca \lesssim 0.01$). The droplet is confined by the geometry of the channel. Droplet breakup occurs solely due to the build up of upstream pressure. Shear is the dominating force in the dripping regime ($Ca \gtrsim 0.02$). Breakup occurs when the viscous shear exerted by the cross-channel flow dominates over the interfacial tension. The jetting regime refers to droplet breakup into an unbounded fluid, which occurs at high values of Ca. The precise value of Ca above which transition from dripping to jetting occurs is presently unknown, and is almost impossible to explore, as the jetting regime could transform to that of a stable jet at any value of Ca above $\sim$0.1.

The velocity gradient in the vicinity of a droplet induces additional viscous stresses on the droplet. The interfacial tension at an oil-water interface gives rise to a pressure drop across the interface. A pressure drop is required for the flow along a microchannel of aqueous droplets in water-oil emulsions. This pressure drop is important even if the viscosity of the oil is small, as it contributes to increase the overall pressure drop in the microchannel. Therefore, in order to achieve precise manipulation of droplets, a key goal is to investigate the pressure profiles in the vicinity of the droplet.

The four key phases of droplet formation are (a) intrusion, where the dispersed

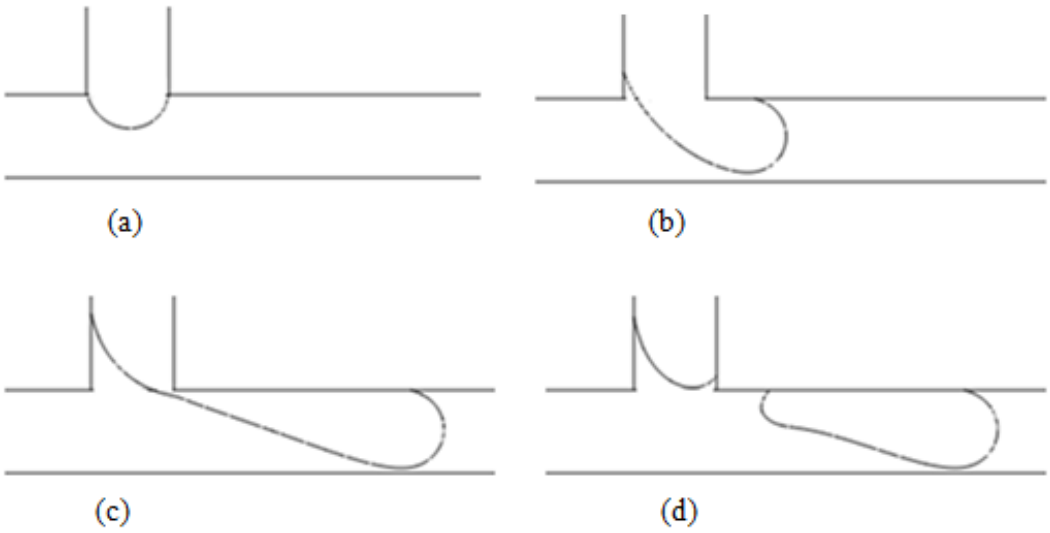

Fig 4.1. Schematic illustrating the four phases of droplet formation: (a) the dispersed phase penetrates into the main channel; (b) the discontinuous stream nearly blocks the main channel; (c) the emerging droplet elongates downstream into the main channel; (d) the droplet separates from the inlet stream.

phase begins to penetrate into the main channel, (b) blocking, where the dispersed phase could extend across the whole width of the main channel, (c) squeezing or elongation, where the emerging droplet is stretched in the downstream direction, and (d) breakup, when the droplet finally detaches from the inlet stream (Fig. 4.1).

De Menech et al. (2008) performed a systematic study of the pressure profile in relation to variations in interfacial tension. However, they did not investigate the dependency of the pressure profile with respect to the flow rate of the continuous phase or contact angle. Garstecki et al. (2006) investigated the evolution of the continuous phase pressure P_c in a study that assumed that the dispersed phase pressure P_d remained constant during the droplet breakup process.

In our previous work (Bashir et al., 2011) (chapter 3), it was predicted using

numerical simulations that the droplet length in the squeezing regime is influenced by the contact angle. In this chapter, numerical simulations are used to predict the effects of the continuous phase flow rate, Q_c, interfacial tension and wettability on the pressure profiles, thus providing a more complete description of the underlying physics of the droplet formation process. The numerical model is described in Section 4.2. The system setup and a grid convergence study are presented in Section 4.3. Results are presented in Section 4.4 and conclusions are summarized in Section 4.5.

4.2 Model description

4.2.1 The level set method

In the current study we have used a conservative level set method (Olsson and Kreiss, 2005) where the level set function is chosen such that the interface between the two immiscible fluids is represented by the 0.5 contour of the level set function ϕ. $\phi = 0$ in the continuous phase (main channel) and $\phi = 1$ in the dispersed phase (lateral channel) as shown in Fig. 4.2. The detail description of the method and governing equations is given in previous chapter 3.

4.3 System description

Predictions from chapter 3 show that influence of wetting property of channel walls on droplet formation is significant in squeezing regime. As the squeezing mechanism can be promoted by strictly confining the droplet in microchannel, therefore the width of the lateral channel was taken to be equal to the width of

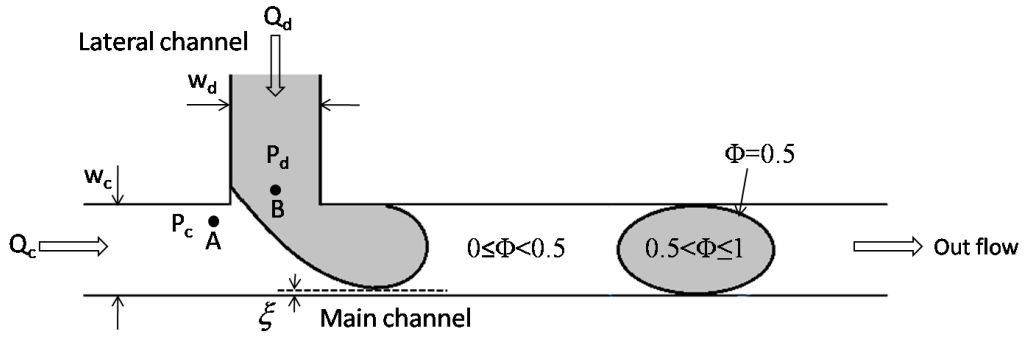

Fig 4.2. Schematic of the flow scenario in the microfluidic T-junction. The widths of the lateral and main channels are denoted by w_d and w_c respectively. A is the point at which the continuous phase pressure, P_c, is evaluated over time. The dispersed phase pressure, P_d is evaluated at the location marked by B. The diagram illustrates a typical process where the droplet is emerging from the lateral channel and is being distorted due to the cross-flow of the continuous phase fluid.

the main channel ($w_d = w_c = 100$ μm) for the T-junction microchannel used in this chapter in order to systematically investigate the physical properties of confined droplet breakup. The densities and viscosities of the dispersed and continuous phase fluids were taken to be the same for simplicity i.e., $\rho_c = \rho_d =$ 1000 kg/m^3 and $\eta_c = \eta_d = 1$ mPs s. For a confined droplet breakup, the effect of the viscosity ratio is almost negligible (Garstecki et al., 2005; De Menech et al., 2008) and therefore the viscosity of the continuous phase is taken to be the same as that of the droplet phase. In addition, the reason for the selection of equal viscosities for both the phases was to examine the contact angle effects independent of any viscous effects that might arise from the presence of the continuous phase flow at the rear interface of the emerging droplet. Usually, at microfluidic scale the difference in densities of the carrier and dispersed fluids is not of importance as buoyancy effects can be neglected since any buoyancy force will be balanced by the opposite force exerted by the channel walls (Wang, 2011).

In general, four dimensionless numbers could be used to describe the droplet breakup system, viz. the capillary number (Ca), the Reynolds number (Re), the flow rate ratio (Q) and the viscosity ratio. As mentioned above, the viscosity ratio is kept constant. As Re is low, its influence is negligible. Thus our droplet generation system can be characterized by just two dimensionless numbers:

- the continuous phase capillary number, defined as $Ca = \frac{\eta_c U_c}{\sigma}$.

- the flow rate ratio, which is defined as the ratio between the dispersed and continuous phases, i.e. $Q = \frac{Q_d}{Q_c} = \frac{w_d U_d}{w_c U_c}$.

In all simulations presented in this chapter pressure is non-dimensionalized using the Stokes scaling $P^* = \frac{P}{(U_c \eta_c)/w_c}$. Henceforth, for convenience of notation, the asterisk is dropped and all results are presented in non-dimensional form. The dimensional pressure P is measured in Pascal (Pa). The accuracy of the numerical scheme was assessed by means of a grid convergence study based on predictions of the evolution of the continuous phase pressure profile P_c from the location indicated by point A in Fig. 4.2. A is chosen to be located at the position where the continuous fluid affects on the emerging droplet interface as well as turns into the lateral channel. Position B is chosen to be located in dispersed phase at the mid position directly above the initial interface position to observe the evolution of P_d with respect to P_c. Mesh statistics are given in Table. 4.1. The pressure evolution profiles are plotted in Fig. 4.3. With reference to these profiles grid mesh (c) was selected for the simulations presented herein.

Table 4.1. Statistics for meshes used in grid convergence study.

Grid	a	b	c	d
No. of elements	1883	2261	2612	3132
No. of degrees of freedom	17559	21015	24219	28971
No. of meshpoints	1044	1242	1425	1697

4.4 Results

4.4.1 Effect of flow rate on droplet length

In the low capillary number (or squeezing) regime, the cross-section of the main channel becomes completely blocked by the tip of the dispersed phase and thus the flow of the continuous phase is obstructed. The small gap ξ between the emerging droplet and the opposite wall of the main channel (Fig. 4.2) is almost negligible. This results in a build up of pressure upstream of the emerging droplet. Hence droplet breakup is activated by the pressure drop across the emerging droplet resulting from the dominance of the interfacial forces over the shear forces. Consequently, the length of the droplet is completely determined by the ratio of the volumetric flow rates of the two immiscible fluids (Garstecki et al., 2006).

During the first two stages of droplet formation as depicted in Fig. 4.1 (a) and (b), the droplet attains a length that is approximately equal to the width of the main channel, w_c. In the elongation phase, when squeezing of the emerging droplet begins, the growth rate of the droplet is proportional to the flow velocity of the dispersed phase ($U_{growth} \propto U_d$) and the neck thins at a rate determined by the continuous phase flow velocity, i.e. $U_{squeeze} \propto U_c$. The duration of the

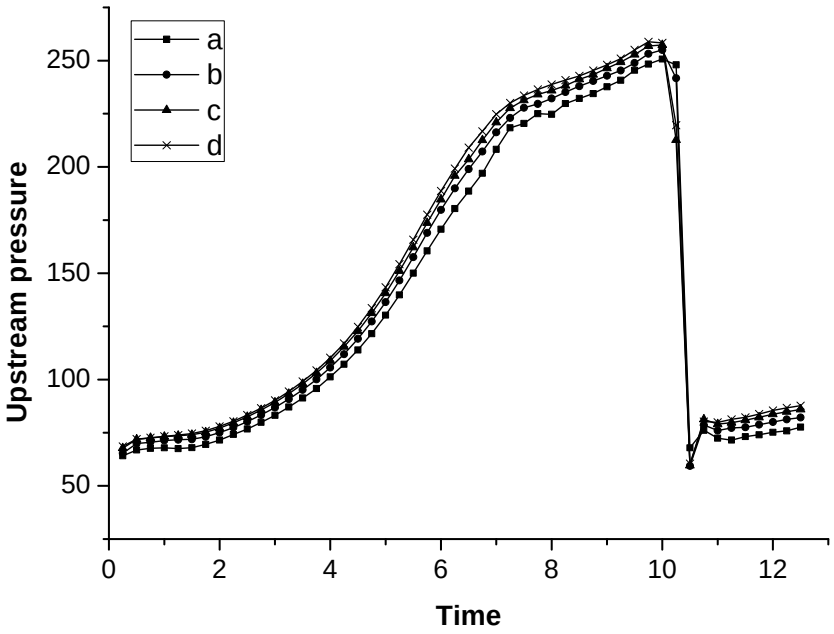

Fig 4.3. Pressure evolution P_c at location A in the main channel upstream of the droplet formation site for a contact angle of $\theta = 150°$ and $Ca = 0.01$. Simulations from the four grids described in Table 4.1 are compared.

squeezing phase, $t_{squeeze}$, can be approximated by the ratio between the width of the neck, w_n, which keeps the droplet connected to the stream of the dispersed phase until it eventually breaks off, and the squeezing velocity. Thus,

$$t_{squeeze} \approx \frac{w_n}{U_{squeeze}}.$$

The scaling law that predicts the final droplet length, L_d, at the point of detachment is

$$L_d = w_c + w_n \frac{Q_d}{Q_c}, \tag{4.1}$$

where Q_c and Q_d are the flow rates of the continuous and dispersed phases

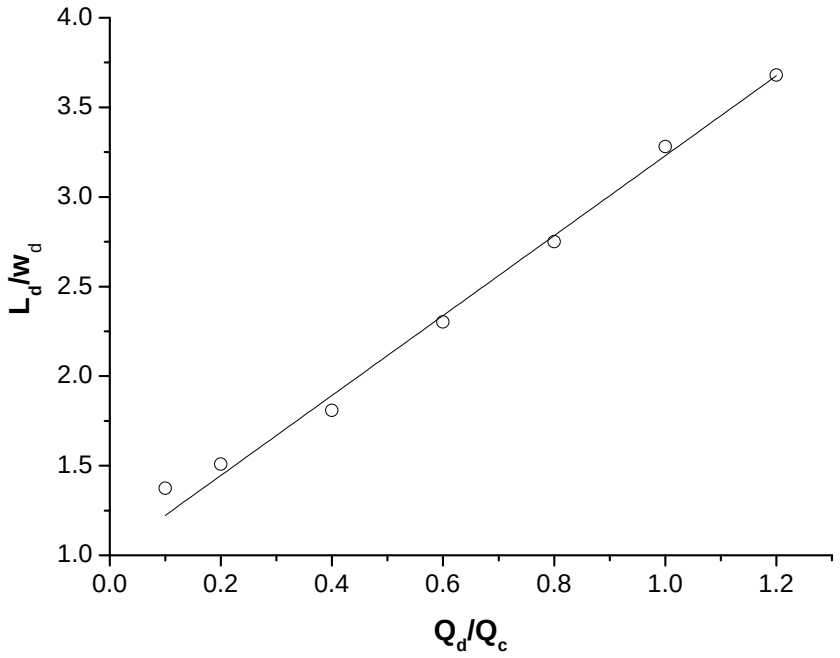

Fig 4.4. The dimensionless length of the droplet as function of flow rate ratio for $Ca = 0.006$. The fitted line is given by the equation $L_d/w_c = 1+2.23Q_d/Q_c$.

respectively. In nondimensional form, Eq.(4.1) can be expressed as

$$L_d/w_c = 1 + \alpha Q_d/Q_c, \tag{4.2}$$

where $\alpha = w_n/w_c$ is a positive constant, its value depending on the geometry of the T-junction. This scaling law suggests that the droplet length depends only on the variation of the flow rate ratio of the two immiscible fluids and is almost independent of the capillary number (De Menech et al., 2008; Garstecki et al., 2006). Eq.(4.1) can be used to predict the droplet length for various flow rate ratios at fixed values of Ca provided $\frac{w_d}{w_c} \geq \frac{1}{2}$. In order to verify that our numerical simulations satisfied this law, we chose a small capillary number ($Ca = 0.006$) and varied the value of Q_d. The full hydrophobic wetting

condition ($\theta = 180°$, where θ denotes the contact angle) was used for these model verification simulations. Thus, in these simulations, the continuous phase completely wetted the walls of the microchannel, whilst the dispersed phase remained nonwetting in order to produce stable droplets (Dreyfus et al., 2003). Results from the our numerical simulations (Fig. 4.4) satisfied the relation $L_d/w_c = 1 + 2.23Q_d/Q_c$. Hence the value of α in Eq.(4.2) is estimated as 2.23. In two other recent studies of microdroplet formation in a T-junction, similar scaling laws were derived experimentally by Tice et al. (2003): $L_d/w_c = 1.9 + 1.46Q_d/Q_c$, and by Xu et al. (2008): $L_d/w_c = 1.38 + 2.52Q_d/Q_c$.

4.4.2 Evolution of upstream pressure profile during the droplet formation process

A series of numerical simulations, with Ca taking the fixed values 0.004, 0.006, 0.008 and 0.01 respectively, was performed to investigate the evolution of the upstream pressure P_c at the location marked A in Fig. 4.2. All four of these values correspond to the squeezing regime. Since $Ca = \frac{\eta_c U_c}{\sigma}$, varying its value can be achieved either by changing the flow velocity of the continuous phase fluid (U_c), or by changing the interfacial tension, σ, between the two immiscible fluids. Firstly, we have kept the interfacial tension constant and varied Ca by altering U_c. The upstream pressure P_c at location A plotted against time is shown in Fig. 4.5 for each of the four values of Ca considered. The inlet pressure of the continuous phase fluid remains almost constant at the beginning of the expansion stage (intrusion) when the internal phase has little influence on the continuous phase. The blocking stage occurs when the internal phase expands across the main channel and causes a reduction in the continuous phase flow.

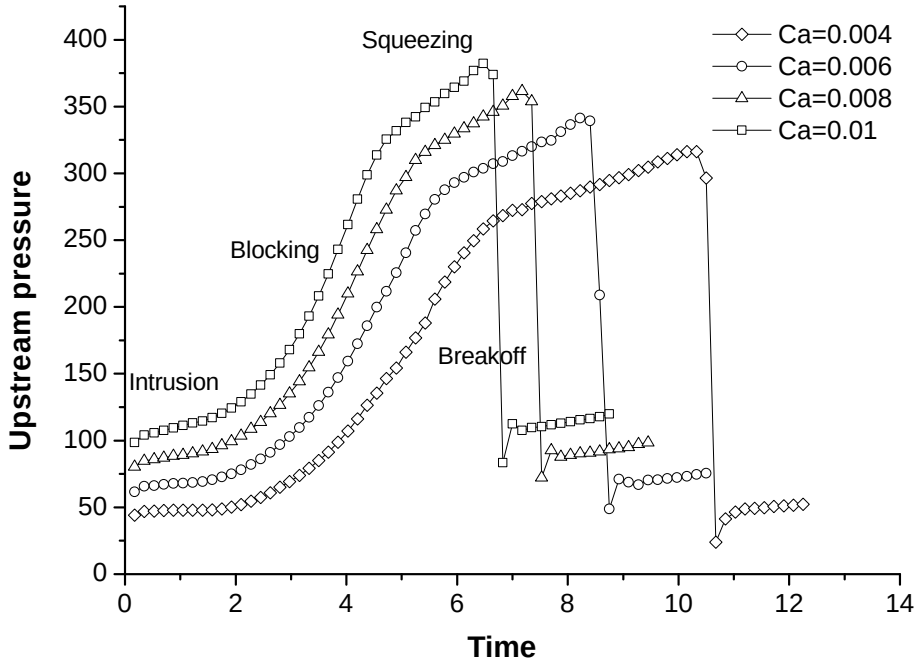

Fig 4.5. Non-dimensional pressure P_c at location A as a function of Ca (the value of which was changed by modifying the flow rate of continuous phase), σ is fixed at 0.005 Nm^{-1} and $U_d = 0.006\,\mathrm{ms}^{-1}$. Pressure was rescaled using the Stokes scaling, $U_c\eta_c/w_c$ and time was nondimensionalized by U_c/w_c.

This obstruction causes the pressure P_c to rise gradually at first, and then sharply, which causes squeezing of the neck to commence. The maximum value (P_{max}) of pressure is achieved when the neck width approaches zero ($w_n \to 0$) which occurs at the end of the squeezing phase. It can be seen in Fig. 4.6 that the value of P_{max} is predicted to increase linearly with Ca. The linear fit is given by $P_{max} = 274 + 10926Ca$. At the moment of break off, the pressure falls abruptly across the interface. At this instant the droplet completely detaches from the incoming dispersed phase, overcoming the wall adhesion. The curvature of the droplet increases until a stable drop is formed. A sharp drop in pressure at breakup occurs because when the neck of the immiscible thread breaks,

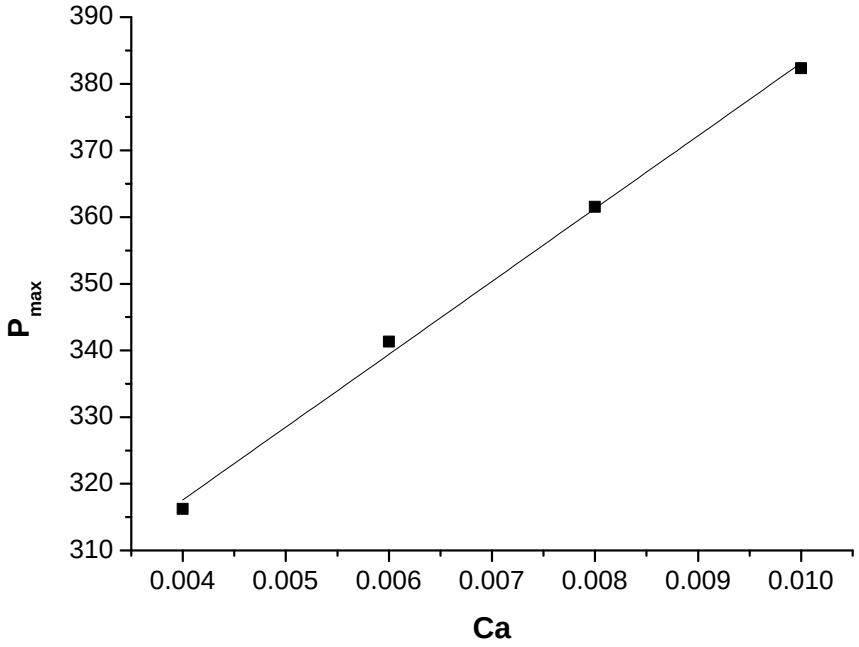

Fig 4.6. Maximum nondimensional pressure as a function of Ca.

the internal phase recoils back into the inlet channel and the droplet moves downstream in the direction of the flow, providing resistance to the flow of the continuous phase and transforming pressure energy to kinetic energy. The durations of the blocking and squeezing periods increase as the velocity of the continuous phase flow decreases. Hence the overall time for droplet formation increases as Ca decreases. This effect becomes more prominent as we move towards lower capillary numbers as shown in case of $Ca = 0.004$ (Fig. 4.5). As expected, the numerical simulations predicted that the pressure drop across the interface was the same for all four cases as the interfacial tension was set at a fixed value. Secondly, the flow rate ratio $Q = Q_d/Q_c$ was fixed to a value of 0.25 and Ca was varied by altering the interfacial tension. The pressure profiles P_c at the upstream location A are plotted in Fig. 4.7. As the flow rate is fixed,

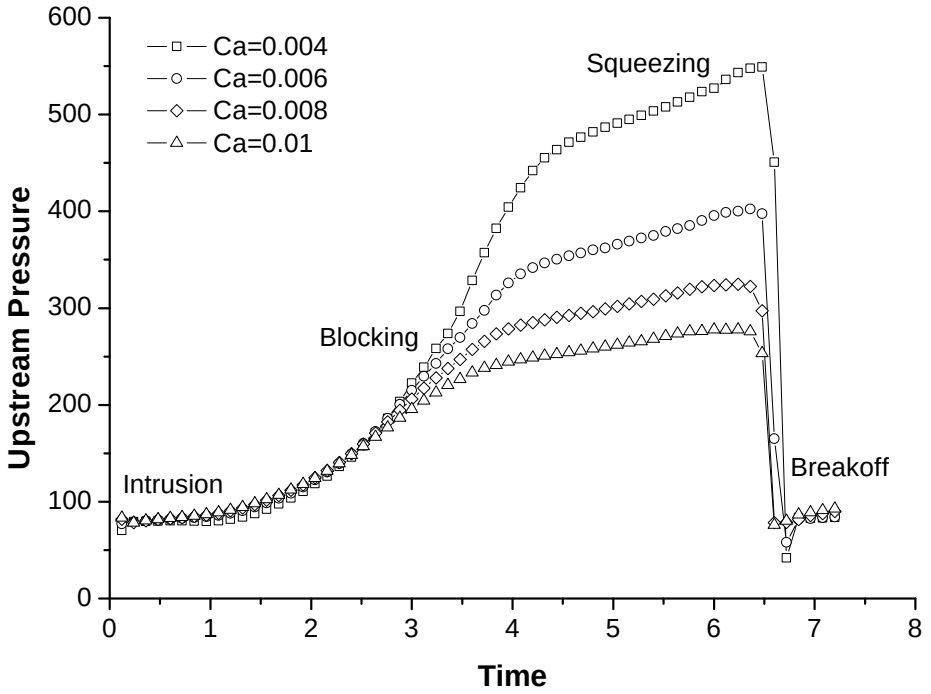

Fig 4.7. Nondimensional upstream pressure P_c at location A as a function of Ca (whose value is changed by altering the value of σ) plotted against nondimensional time. $Q = 0.25$.

it follows that the initial pressure in the intrusion phase is the same for all four values of capillary number considered which is in contrast to the previous case in which U_c was varied. The blocking time is predicted to increase with interfacial tension, but the squeezing time remains roughly constant which indicates that it is nearly independent of the interfacial tension, consistent with the findings of De Menech et al. (2008). Thus the squeezing time is influenced only by the flow rate of continuous phase fluid. The pressure drop across the interface in this case decreases as Ca increases from 0.004 to 0.01 as shown in Fig. 4.8 as a consequence of interfacial tension effects. The power law fit suggests that this pressure drop varies inversely with Ca. This implies that it is directly proportional to σ which is consistent with the Young-Laplace law which states

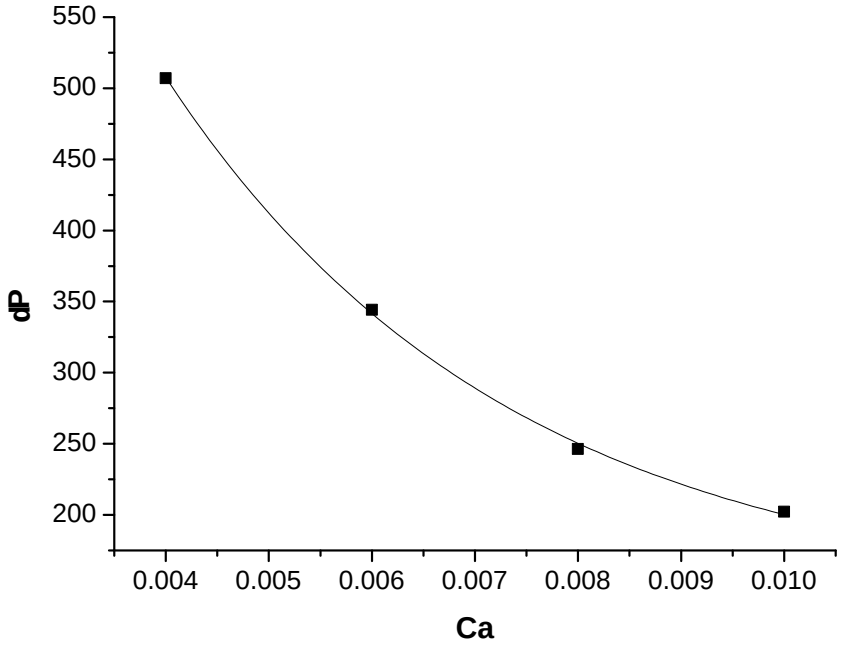

Fig 4.8. Pressure drop across the interface as a function of Ca. $Q = 0.25$.

that

$$\delta P = \frac{2\sigma|\cos\theta|}{(w_c/2)}. \tag{4.3}$$

The simulations predicted that the droplet length is unchanged by the length of the main channel. This result was also found by De Menech et al. (2008). However, we found that the pressure profiles are sensitive to changes in the length of the microchannel due to the resistance exerted on the flow by the channel walls (Fig. 4.9). However, if these profiles are rebased, for example scaled on the 3 mm pressure curve, the three curves collapse to a single profile, indicating that the channel length has no effect on the dynamics of the droplet formation process.

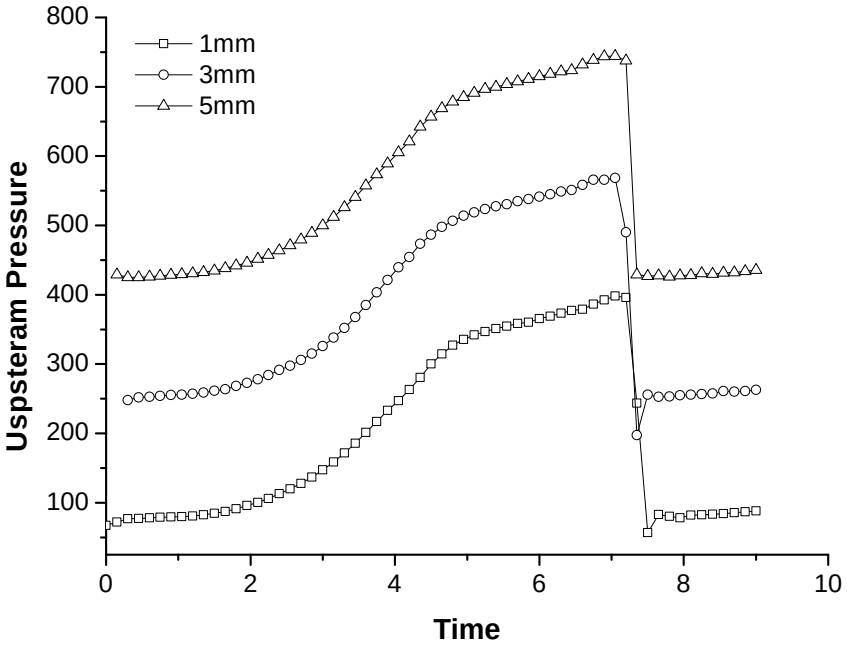

Fig 4.9. The upstream pressure P_c at point A for main channel lengths of 1 mm, 3 mm and 5 mm for $Ca = 0.006$.

4.4.3 Pressure difference between the continuous and dispersed phase fluids

Fig. 4.10 shows the evolution of pressure profiles in both the continuous and dispersed phases together with the pressure drop $P_d - P_c$. The simulations predict that the pressure in the dispersed phase is always higher than the pressure in the continuous phase, i.e. $P_d > P_c$. At the start of the droplet formation process when the dispersed phase begins to intrude into the main channel, the pressure P_d remains approximately constant as at this stage it is largely unaffected by the presence of the continuous phase. The pressure difference $P_d - P_c$ decreases gradually at first, and then more sharply during the blocking phase.

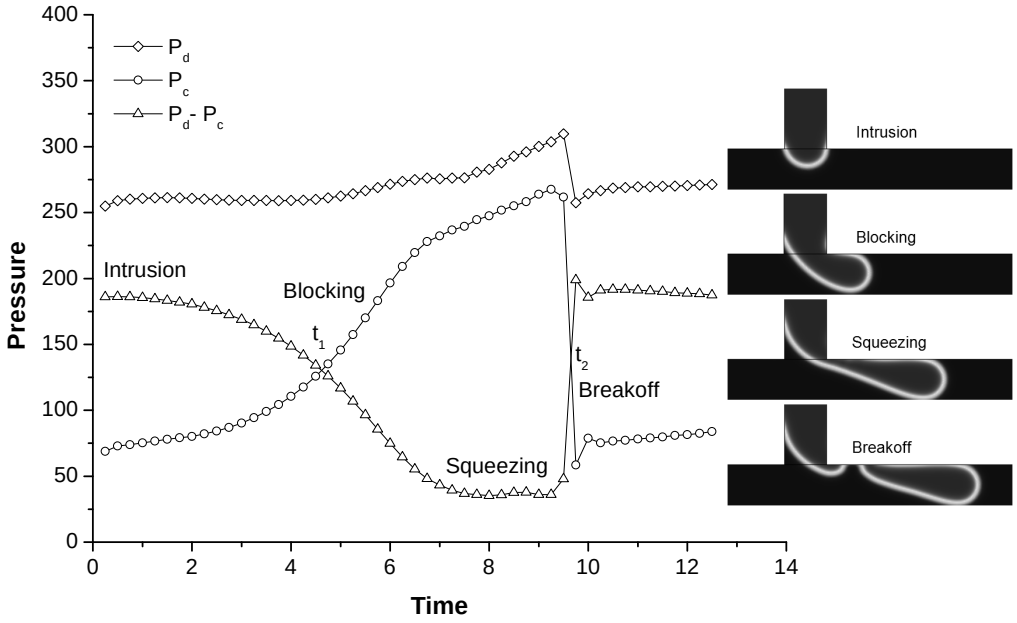

Fig 4.10. Time evolution of the dispersed phase pressure P_d, continuous phase pressure P_c and the pressure difference $P_d - P_c$ for $Ca = 0.01$, $\sigma = 0.005\text{N/m}$ and $Q = 0.25$.

The pressure profiles P_c and $P_d - P_c$ intersect each other at time $t_1 = 4.5$. At this stage the continuous phase begins to have a noticable influence on the incoming dispersed phase via the sharp increase in P_c which exerts stress on the developing interface at the junction. This leads to an increase in P_d and the droplet starts growing in the direction of the main channel, rather than being pushed back into the inlet channel. Consequently, it begins to obstruct the continuous phase flow. Thus P_c starts to increase sharply and at the same instant P_d begins to increase slowly. At a nondimensional time of around 9.5, indicated by t_2, a sharp increase is predicted as the neck of the developing droplet is squeezed. At a nondimensional time of 7.5, the P_d profile becomes parallel to P_c in the squeezing phase due to the intrusion of the continuous phase into the lateral channel and consequently $P_d - P_c$ remains almost constant during that period. At time t_2 when the two pressure lines P_c and $P_d - P_c$ cross again,

the droplet finally separates from the incoming dispersed phase. During this breakup phase, the pressures P_c and P_d fall to their minimum values, at which point the difference between their values, $P_d - P_c$, attains its maximum value (i.e. $P_d - P_c$ returns to its value at the start of intrusion). These variations in P_d contradict the assumption made by Garstecki et al. (2006) that P_d remains constant during the droplet formation process. This assumption simplified the analysis of the pressure evolution during the droplet breakup process. However, improved understanding of the physics of the breakup process is likely to be beneficial for the precise control of droplet production in the laboratory. The time period t_2 is important as it determines the droplet formation time. At time t_2 the pressure drops in both phases to levels dependent on the force with which the recoiling of the tip back into the inlet channel takes place. The Laplace equation gives the relationship between capillary pressure (this is the pressure difference across the interface of two fluids), surface tension and the principal radii of curvature, R_1 and R_2, of the interface between two immiscible fluids. The behavior of the pressure difference $P_d - P_c$ follows the Laplace equation in a qualitative sense. Thus

$$P_d - P_c \sim \sigma \left(\frac{1}{R_1} + \frac{1}{R_2} \right). \tag{4.4}$$

This indicates that the droplet can be considered to be in a series of equilibrium states during its formation process, and as such, at small Ca, the pressure difference between the two immiscible fluids should not be ignored.

4.4.4 Effect of contact angle on upstream pressure in the continuous phase

The sensitivity of the pressure upstream of the junction in the continuous phase flow (i.e. at the location A) to the hydrophobicity of the microchannel walls is examined by plotting the pressure profiles for different values of the contact angle (θ) as shown in Fig. 4.11. Values of θ studied range from 90° (non-wetting) through to 180° (complete wetting). It was observed that for all values of θ considered, the pressure remains almost constant in the intrusion phase. Again this is because the flow rate is kept fixed. The channel becomes blocked more quickly in the case of $\theta = 180°$ as the adhesive forces are very low (due to the superhydrophobicity of the channel walls) which in turn increase the cohesive forces in the inlet channel. As a result, the continuous phase fluid intrudes further towards the inlet channel, which applies additional stress on the internal phase to squeeze as shown in Fig. 4.12. As θ decreases, the time over which the blocking process occurs becomes longer as the adhesive forces between the channel walls and the droplet decrease (Fig. 4.11). This effect is particularly noticeable for $\theta = 90°$ and $\theta = 120°$. The duration of the squeezing process remains about the same for all four cases studied as once the main channel has become blocked by the dispersed phase, then the roles of interfacial tension (cohesive forces) and shear forces from the continuous phase fluid become dominant over the adhesive forces. For $\theta = 90°$, there is a smooth transition of pressure from the blocking phase towards the end of squeezing phase. For this contact angle, the pressure drop across the interface is smaller than that associated with the other three contact angles considered. This implies that non-wetting might induce an additional pressure drop due to

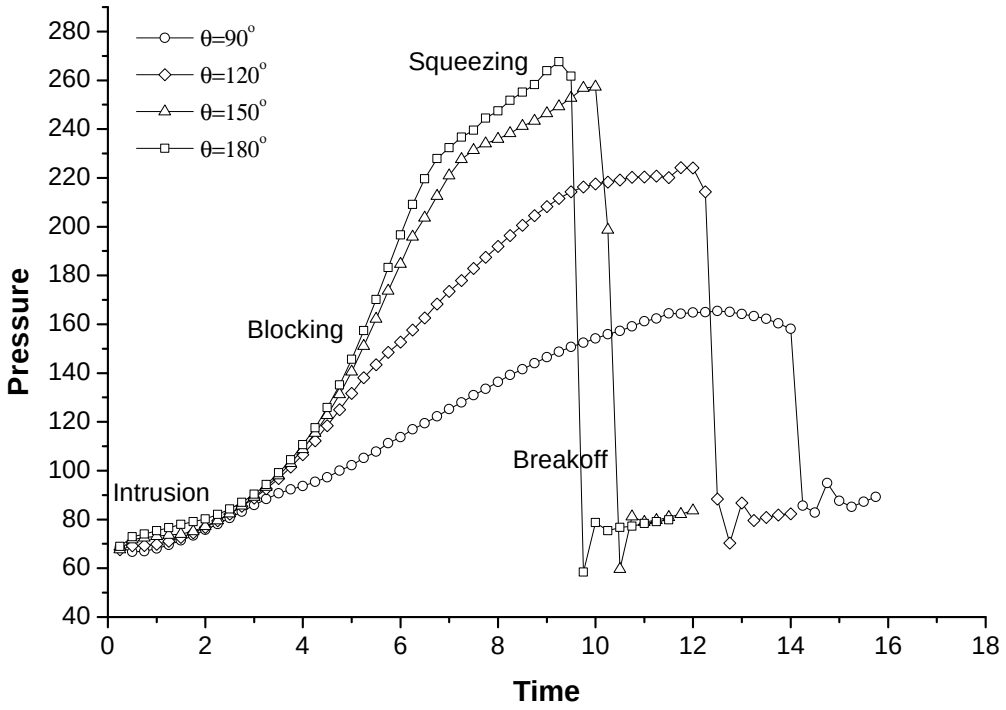

Fig 4.11. Pressure P_c at location A in the main channel upstream of the droplet formation site as a function of contact angle. Ca is 0.01 in all four cases.

the additional repulsive forces between the channel walls and the droplet.

The static pressure difference (Laplace pressure) between the interior of the droplet and the surrounding continuous phase liquid is given by the Young-Laplace equation (4.3). The pressure difference is related to the contact angle, θ, which in turn affects the shape of a droplet in the microchannel. Consequently, the curvature of a droplet interface can be inferred from a function of the Laplace pressure. From equation (4.3) it is clear that δP increases as θ is increased from 90° (nonwetting) to 180° (wetting). Thus an increase in θ from 90° to 180° corresponds to a reduction in the radius of curvature, thus producing a more curved interface. This effect of contact angle on droplet shape is shown in Fig. 4.13.

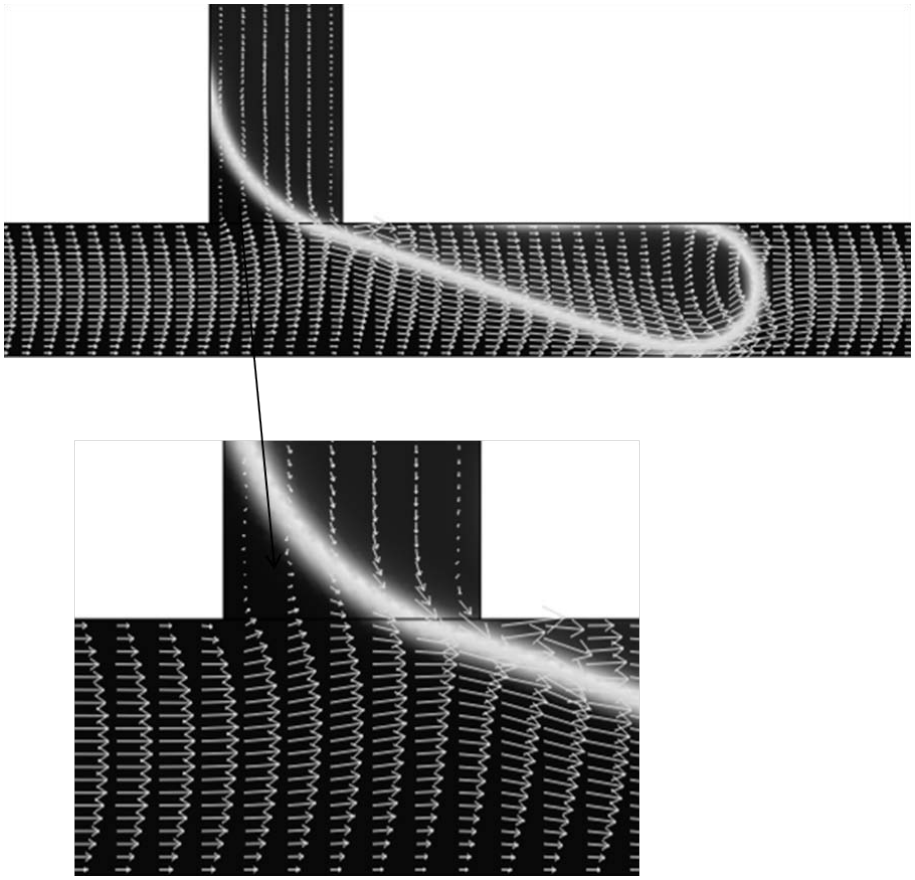

Fig 4.12. Intrusion of continuous phase into the internal phase.

4.5 Conclusions

Numerical simulations of the droplet formation process in a microchannel T-junction have been carried out using a conservative two phase level set method. Detailed analyzes of the pressure profiles at a point upstream of the junction have been presented for a range of different physical parameters falling within the squeezing regime, i.e. for $Ca =\lesssim 0.01$. The effects of varying Ca by (i) keeping the interfacial tension constant and varying the flow rate of the continuous phase, and (ii) keeping the flow rate of the continuous phase fluid fixed and varying the interfacial tension, have been presented. We have shown that the

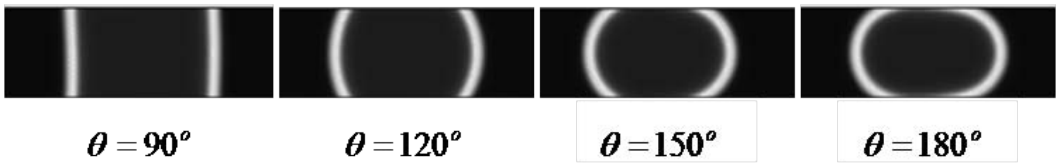

Fig 4.13. Effect of contact angle on droplet shape, $Ca = 0.01$, σ=0.005, $w_d = w_c$.

time required to squeeze the neck during the process of droplet formation is dependent on the flow rate. The pressure drop across the droplet during breakup is also shown to be affected by the wetting properties of the microchannel. Examination of the evolution of the pressure profiles in the continuous and dispersed phases enabled us to distinguish the four phases (intrusion, blocking, squeezing and break off) of the droplet formation process. The pressure profiles predict that the time required for the main channel to become blocked by the dispersed phase increases as hydrophobicity of the microchannel walls is reduced. Thus the time to breakup is longer for partially hydrophobic surfaces. The pressure drop associated with droplet breakup is decreased for channel walls that are more hydrophilic. Although multiphase processes are very complex and their accurate description via numerical methods is still challenging we have shown that the conservative level set method has the potential to predict details of the physics behind the droplet formation process in a microchannel.

5

Dynamic wetting in microdroplet formation

The preferential wetting of the walls of microfluidic device by the continuous phase fluid is critical to the droplet formation process and can be influenced by modification of the microchannel walls. The addition of a surfactant to a liquid dynamically modifies the microchannel surface and consequently effects the droplet formation process. The current work aims to study the effect of surfactants on an oil-water interface during droplet formation in a T-shaped microchannel geometry. The surfactant Span 80 was used in combination with mineral oil in order to observe the effect of surfactant on droplet formation and to characterize the wetting properties of the microchannel wall

5.1 Introduction

Technology based on droplet microfluidics offers a novel approach for the controlled preparation of monodispersed microemulsions. These monodispersed microemulsions have been widely used to obtain high quality pharmaceuticals (Zheng et al., 2003), food products (Skurtys and Aguilera, 2008) and cosmetics. They also have potential uses in a number of other chemical and biological applications (Teh et al., 2008; Theberge et al., 2010; Schaerliab and Hollfelder, 2009). The ability to precisely control the dynamics of droplets containing nanolitre volumes of fluids is required to further exploit our usage of microemulsions. Increased understanding of the behaviours of multiphase flows is also central to this goal.

Microemulsions are thermodynamically metastable. In order to exploit their properties for chemical and industrial purposes it is necessary to stabilize them over a long period of time. These emulsions can be stabilized by the use of surfactants. Surfactant molecules accumulate on the interface between liquid/liquid and liquid/gas due to their amphiphilic nature, causing a reduction in the interfacial tension between the two immiscible fluids. The interface becomes saturated with surfactants above a critical concentration called the critical micelle concentration (CMC).

T-junction microfluidic devices are the most popular droplet generation devices. Droplets are formed when the dispersed phase stream is sheared off by the carrier fluid at the junction (Thorson et al., 2001; Nisisako et al., 2002; Garstecki et al., 2006; Husny and Cooper-White, 2006). A significant amount of work has been dedicated towards understanding droplet controlling parameters such

as flow rate and the viscosity ratios between two immiscible fluids, However, further investigations into the effects of surfactants on interfacial tension and wetting properties are still required in order to fully control and understand the dynamics. Hence we obtain the motivation for the present study. It has been suggested quantitatively that for the stable formation of W/O emulsions, the contact angle of a water droplet with the microchannel surface should be 180° (Dreyfus et al., 2003). Typically, the water droplet contact angle with a hydrophobic surface is between 90° and 120° (Armani et al., 1999) where the oil phase is the surrounding media. If a surfactant is added to the continuous oil phase, the contact angle gradually increases and the surface properties change from hydrophobic to superhydrophobic (Dreyfus et al., 2003). Dreyfus et al. (2003) studied the wetting characteristics of droplet formation of deionized water/tetradecane-Span 80 systems in a microfluidic device and identified different flow regimes for various flow rate ratios between oil and water that were similar to those identified by Thorson et al. (2001). They concluded that to achieve stable formation of droplets, the surfactant concentration should be well above the critical micelles concentration (CMC). These investigations were further confirmed by Xu et al. (2006a,b) who emphasized the importance of wetting properties by generating W/O and O/W emulsions using a single microfluidic device.

The current work reports on an experimental investigation comprising a systematic study of the effects of wettability of microchannel walls on droplet formation including the addition of a surfactant into the microfluidic T-junction device. We have considered relatively low flow rates of the dispersed phase fluid. The flow rate ratio was altered by varying the cross shear flow of the continuous oil phase in order to closely monitor the relative effects of interfacial tension and

shear force on the droplet break up process. The effect of surfactant concentration on droplet lengths within the contact angle transition region were studied. Furthermore, dynamic contact angles (advancing and receding) formed by the aqueous phase with the microchannel surface were measured in order to characterize the dynamic wetting characteristics of two phase microchannel flows.

5.2 Materials and measurements

DI-water was used as the aqueous phase for all experiments. The non-aqueous phase used was a light white mineral oil obtained from Sigma Aldrich Chemical company (M5904). The density of the mineral oil measured at room temperature (25°C) was found to be 843.1 kg/m^3 by weighing the solution in a specific gravity bottle using a sensitive mass balance with precision up to 5 significant figures. Viscosity was measured to be 24.1 mPa s using an Ostwald viscometer. The Ostwald viscometer was calibrated by measuring the flow time of DI water thrice. The measurements were repeated three times and the error was found to be ± 0.06 mPa s. The viscometer was cleaned with acetone and dried with compressed air in a clean room. All measurements were made in a controlled temperature room with variation of less than ± 1°C. Values of fluid viscosity were determined from the viscometer observations by means of the relationship:

$$\mu = \mu_w \frac{\delta t}{\delta t_w} \frac{\rho}{\rho_w}, \tag{5.1}$$

where μ is the viscosity of the mineral oil, μ_w is the viscosity of DI-water. The ratio ρ/ρ_w is the mineral oil density relative to that of water. The flow time δt is the time that elapses as the meniscus passes between two marked locations

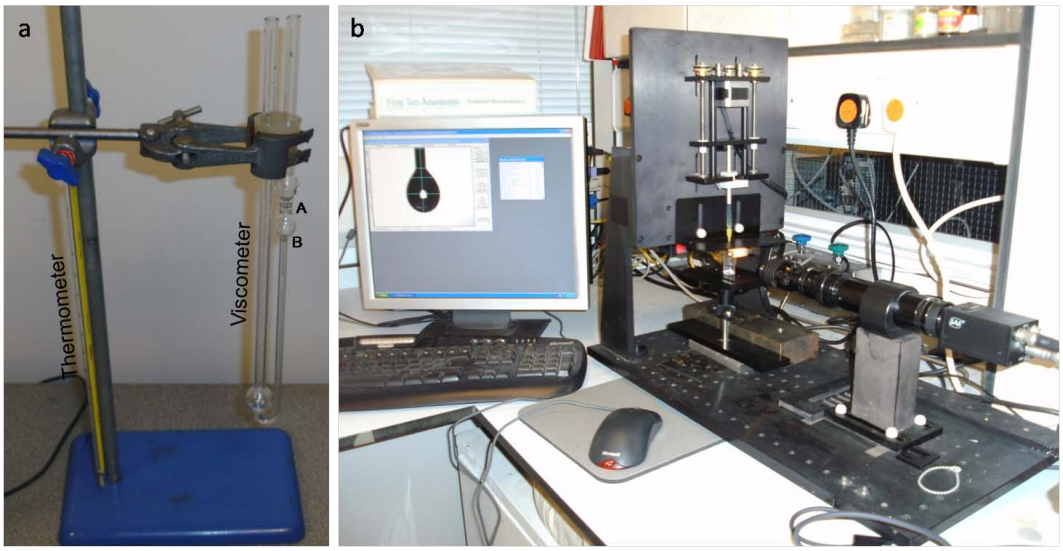

Fig 5.1. (a) Ostwald viscometer, (b) FTA200 tensiometer.

on the viscometer in case of mineral oil and δt_w represents the same in case of water (Fig.5.1 (a)).

The surface active chemical tested was Span 80 (sorbitan mono-oleate: $C_{22}H_{44}O_2$) obtained from Sigma Aldrich Chemical Co. (S6760). Span 80 is one of the most commonly used surfactants in microfluidics. It is a hydrophobic nonionic surfactant that contains a mixture of fatty acid components in addition to the predominant oleic acid component. Its hydrophilic lipophilic balance (HLB) is 4.3. The density of Span 80 was measured to be 986 kg/m^3 at room temperature (25°C), and it has a nominal molecular weight of 428 g/mol. Span 80 was dissolved in the mineral oil and was found to be readily soluble at all concentration levels. The surfactant was used in its original form without further purification. To make a solution of a desired concentrations, a known volume of surfactant was added with a micropipette to a known volume of solvent. The oil-surfactant solutions were allowed to equilibrate in the laboratory for 24 h.

The interfacial tension of DI water and mineral oil was determined via the use of

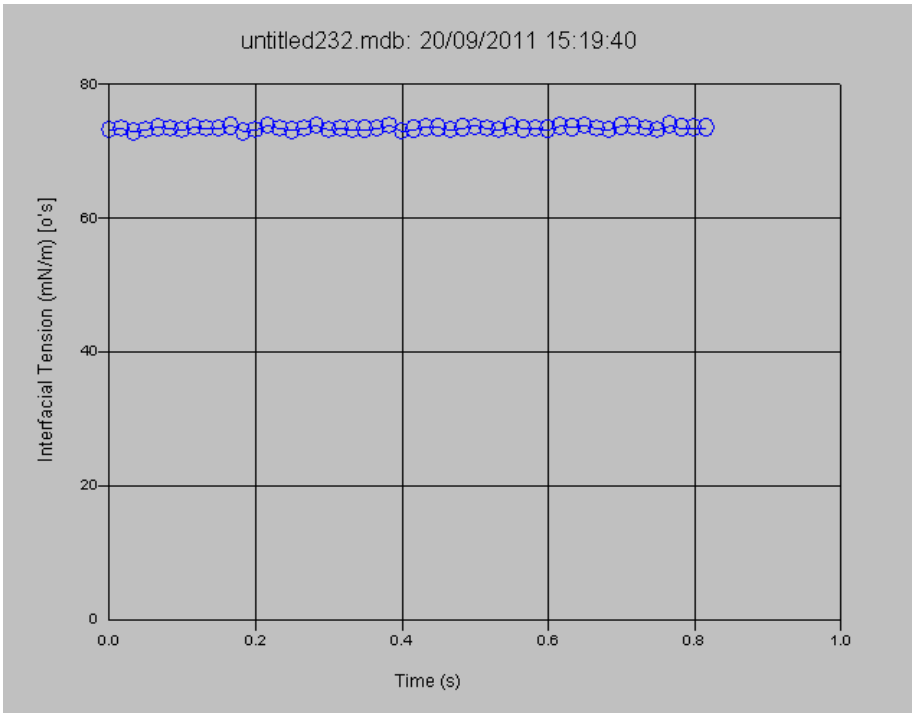

Fig 5.2. Calibration image of tensiometer corresponding to surface tension of DI water.

a fully automated commercial tensiometer (FTA200, First Ten Angstrom) using the drop shape method (Fig.5.1(b))(Woodward., 2008b). The calibrations were made using a water droplet emerging from a needle of known diameter for which the interfacial tension is known (as shown in Fig. 5.2). Although a range of syringe sizes can be used in the pump, it was found that small volume syringes (1 mL or lower) produced data with the lowest relative standard deviation. Therefore, for all the experiments in this study, a 1 mL syringe is used.

The equilibrium value of the surface tension of DI water after calibration was found to be 72.89 mN/m and that of mineral oil (without the addition of surfactant) was found to be 34 mN/m with a standard deviation of 0.03. Droplets were formed at the tip of a flat needle using an inflow at rate of 1 μl/s which was maintained in a programmable syringe pump. The software provided with

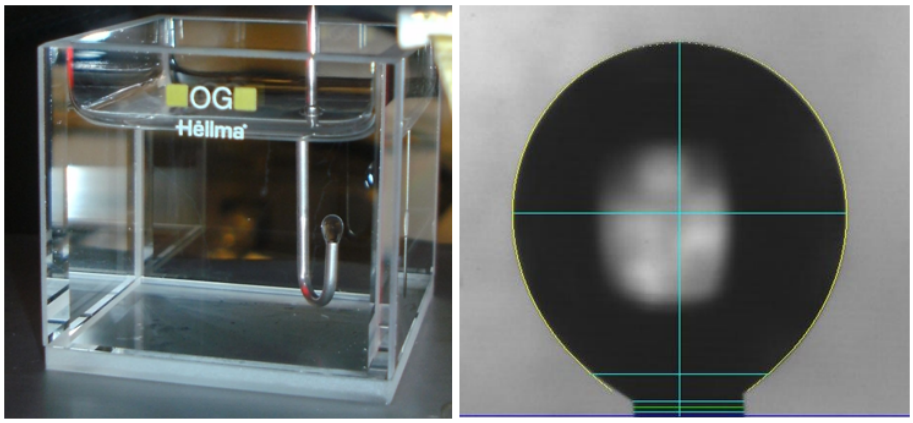

Fig 5.3. Oil drop emerging from U-shaped needle in water contained in a glass cuvette.

the tensiometer used the Laplace equation to calculate the interfacial tension. The interfacial tensions between sample solutions and water were measured using the arrangement shown in Fig. 5.3. A pendant drop of oil floating up from the dispense tip into the water phase in shown. The values of interfacial tension were measured after the system achieved equilibrium state. Each experiment was repeated 3 times. The standard deviation in each case remained below 1.0 mN/m which confirmed the accuracy of the measurements.

The viscosity of mineral oil is sufficiently high to ensure the likelihood of droplet formation in the microchannel due to the existence of a high viscous shear. The viscosity of the oil did not change significantly with the different surfactant concentrations. All the reagents were filtered through millipore microfilters with pore size of 0.45 μm before injecting them into the microchannel to minimize contamination, e.g. by foreign particles. Droplet images obtained from the microfluidic experiments were processed using the image processing software packages FTA32 and ImageJ to obtain measurements of the advancing and receding contact angles.

Table 5.1. Interfacial tension between water and mineral oil corresponding to different surfactant concentrations.

Concentration of Span80(% w/w)	Interfacial tension between water and mineral oil(mN/m)
0	24.56
0.01	18.07
0.05	12.43
0.1	9.58
0.2	6.42
0.4	4.77
0.8	4.61
1	4.55
2	4.37
4	4.29
6	4.17
8	4.09
10	4.02

The degree of wettability of a PDMS surface caused by the addition of surfactant to a mineral oil were characterized via contact angles measurements made using a tensiometer. A small piece of PDMS slab was placed in a flat and optically transparent cuvette. The cuvette was filled with mineral oil containing different concentrations of surfactant ranging from 0 to 10% w/w. A small volume of water was pumped through a syringe needle, which was already immersed in an oil, onto the PDMS surface at very slow flow rate of 0.1 μl/s. A snapshot of a water droplet on a PDMS surface in an oil media is shown in Fig. 5.4. All contact angles were measured using the sessile drop method. The measured values of water contact angles on the PDMS surface are shown in Fig. 5.5 along with the interfacial tension data. It shows that the contact angle of water with the PDMS surface increases from hydrophobic to superhydrophobic as the concentration of surfactant (C_s) in the surrounding oil media increases. The corresponding interfacial tension between water and oil decreases with sur-

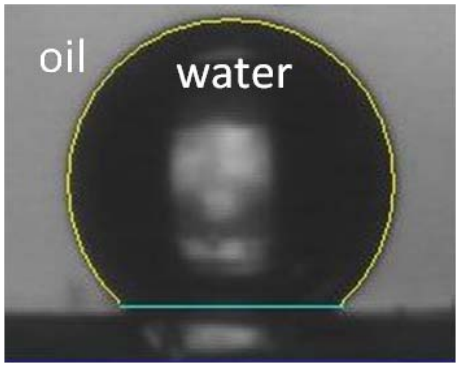

Fig 5.4. Water contact angle with PDMS surface with oil as the surrounding medium measured in equilibrium as 146°, 0.1% w/w concentration of Span 80 added into the oil.

factant concentration and does not change significantly when the critical micelle concentration (CMC) of $\sim$ 0.5 % w/w is exceeded.

5.3 Microfluidic device

The microfluidic chip design consists of a T-junction followed by a diverging channel via 180° return bends. The channel dimensions are about 100 μm wide $\times$ 50 μm high. The purpose of the return bends is to elongate the channel thus providing increased residence times for long time chemical reactions. Practical examples of such reactions within droplets include incubation of cells and protein crystallization. Droplet breakup occurs by a cross shear flow method and then emerging droplets pass through a divergence in order to increase the surface to volume ratio. This divergence of the outflow has several advantages:

- Droplets are not restricted by the channel wall and hence the droplet shape relaxes to a spherical shape due to minimization of the surface tension forces around the droplets up to an extent that depends on the

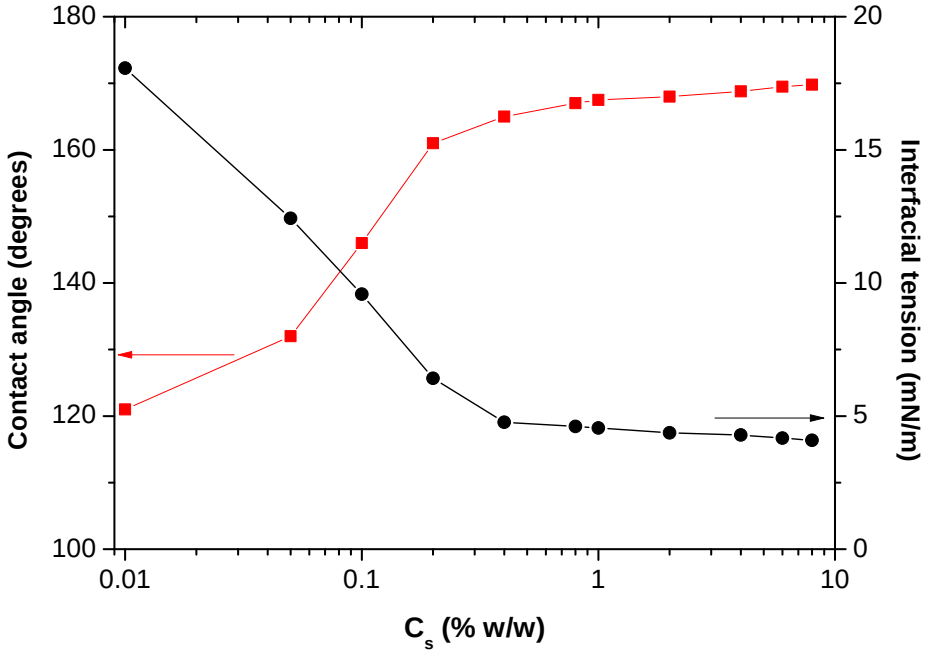

Fig 5.5. The interfacial tension between DI water and mineral oil (shown by circles) and contact angle of a water droplet on PDMS surface in an oil (shown by squares) at varying surfactant concentrations of Span 80.

flow rate ratio and the ratio of the width of the diverging channel to that of the main channel.

- It confines the contents of aqueous droplets more readily as the continuous phase has more available area to flow around the droplet which prevents the contents of droplet from sticking to the walls of the microchannel.

- It facilitates the removal of formed droplets from the channel for storage purposes as the flow resistance decreases in the diverging channel section.

The cross-section of the outlet channel was double than that of the main channel. This diverging chamber was not made so wide as to disrupt the original sequence of droplets. If the channel is too wide then the precise control of the position

Fig 5.6. Schematic of microfluidic chip.

each droplet is compromised. When a droplet enters into the divergent section, the shear stress decreases and drop deforms.

5.4 Microchip fabrication

The fabrication process of the PDMS microchip consisted of the standard photolithography method using SU-8 negative photoresist mould (Duffy et al., 1998; McDonald et al., 2000, 2002; Ng et al., 2002; Sia and Whitesides, 2003). The PDMS curing agent and base (Sylgard 184;Dow Corning) were mixed rigorously in the ratio of 1:10 for 5 minutes. The mixture was degassed using a vacuum desiccator and then poured onto the patterned SU-8 master. It was then cured in an oven at 65°C for 1 hr and then was peeled off from the master. The inlet and outlet holes were punched using a 1 mm biopsy punch. The resulting channel structure was then bonded onto another flat PDMS slab. The bonding of a PDMS replica with a 2 mm thick PDMS slab was carried out using the laboratory made plasma chamber shown in Fig. 5.8. Both the PDMS replica (with feature side up) and the slab were placed into an air plasma for 6 min and then were brought in contact with each other. After 5 min the sealed microchip was placed in an oven for about 2 hr to enhance the bonding strength.

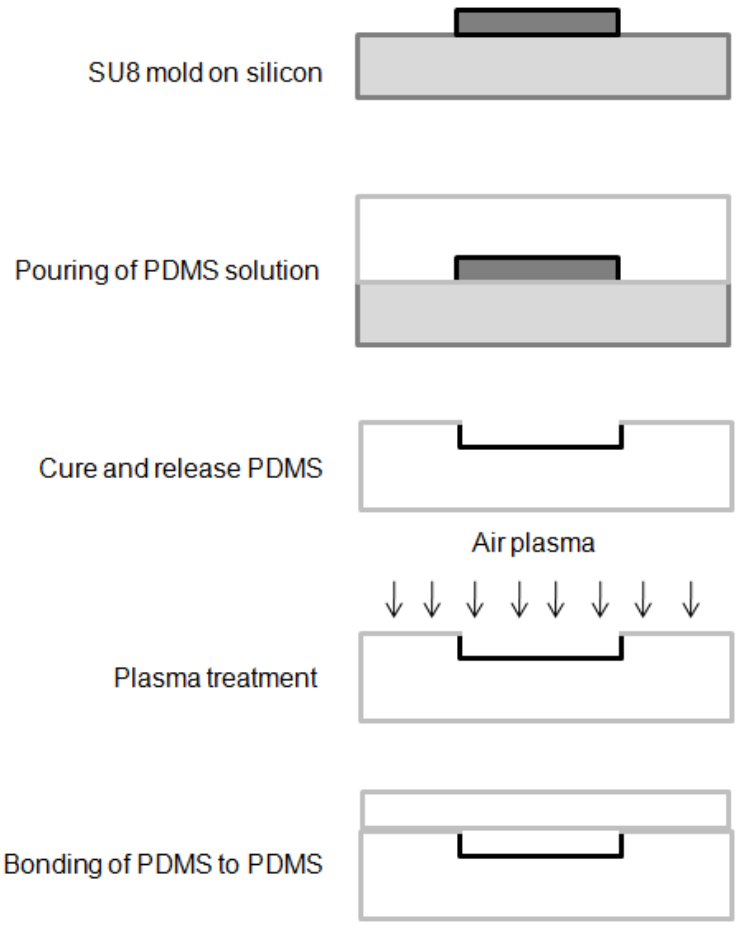

Fig 5.7. PDMS microchip fabrication using soft lithography.

The bonding setup consisted of a jet plasma generated in a vacuum flask. A steel rod in the center of the flask was fixed to a rubber bung at the top of the flask and connected to the high voltage. The rubber bung seals the flask in order to create the vacuum. The ground electrode, made of copper sheet, was placed underneath the flask. The bottom glass wall of the flask acts as a dielectric barrier for plasma generation. The distance from the lower end of steel rod to the bottom of flask can be adjusted according to the thickness of the substrates. A concentrated high voltage electric field emits from the lower end of the high voltage electrode and breaks down the air in vacuum flask. Plasma

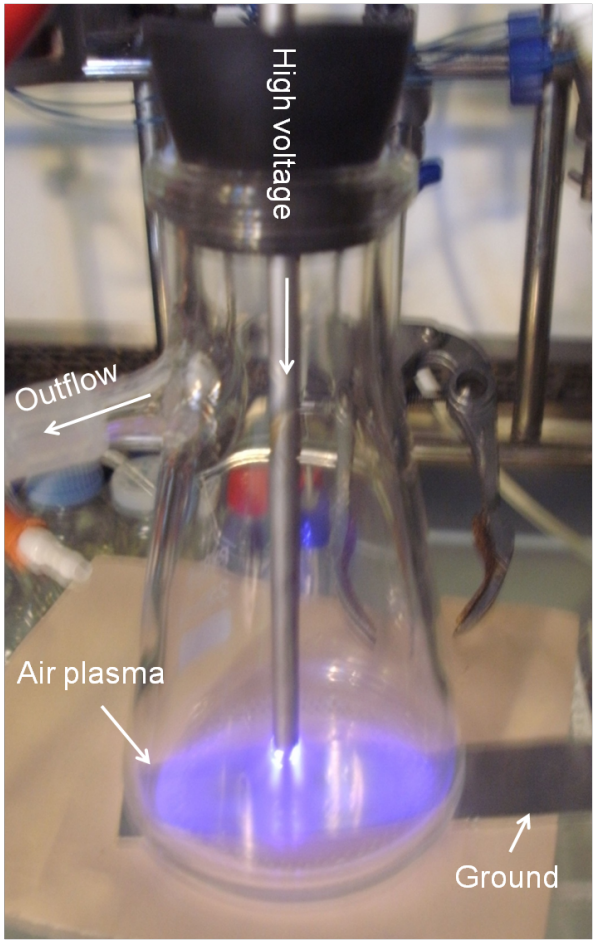

Fig 5.8. Bonding of microfluidic chip using laboratory made plasma setup.

was ignited in the form of a jet.

5.5 Experimental setup and analysis

Mineral oil containing surfactant and DI-water kept in 1ml syringes, were loaded into the two inlets of microfluidic chip via PTFE tubing for the purpose of droplet formation. Each of the syringes was driven by an individual syringe pump in order to control the flow rate ratio as required. Small volume syringes ($\leq$ 1ml) were used in order to attain tight control over the accuracy of the

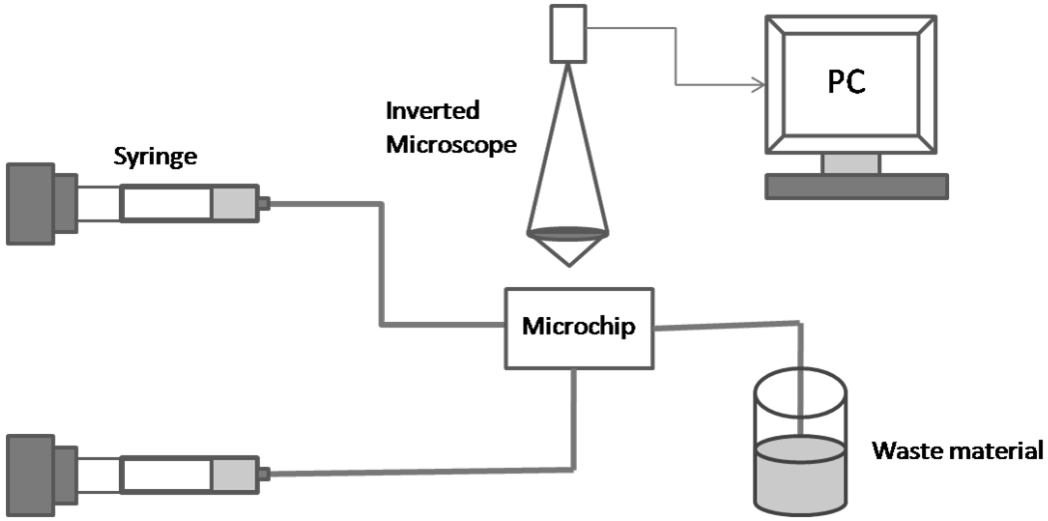

Fig 5.9. Schematic of the experimental setup for droplet formation in microchip.

volumes of liquids dispensed. PTFE tubing was carefully inserted into both inlets to avoid distortion of the PDMS channel. The outlet was connected to a waste container with a section of tubing. The pumps were connected in series and controlled via the use of a personal computer (PC) over a serial cable RS232. An inverted microscope (Zeiss Axiovert 100) and a 1280 $\times$ 1024 resolution charge coupled device (CCD) camera (Sensicam QE, PCO Co., Ltd.) were used for acquiring droplet images. An objective lens with a 2.5 times magnification power was used to capture the flow field near the walls of the microchannel. The channel dimensions and droplet lengths were measured by counting pixels. The system was calibrated against a true length scale. The image of a graticule with 0.05mm graduation marks was captured with a 2.5$\times$ objective lens onto the CCD array. By comparing the number of pixels in horizontal direction on an imaged graticule with its corresponding mm scale units, 1 pixel was calculated to be equivalent to 0.002577 mm=2.577 μm. In order to fully wet the microchannel with the continuous phase, we first introduced oil into the channel. Once the continuous phase filled the entire microchannel, the dispersed

phase was introduced from the lateral channel whilst maintaining the flow of continuous phase from the main channel in order to facilitate the generation of microdroplets. Changes to any of the operating parameters necessitated a minimum delay time of about 5 min for the purpose of equilibrating the system.

5.6 Results and discussion

5.6.1 Influence of surfactant on droplet length

Experiments of droplet formation in the microfluidic device were performed with surfactant concentrations in mineral oil of above 0.1 wt.% as ordered flow patterns were obtained above the transition concentration of Span 80 at 0.1 wt.% similar to those obtained by Xu et al. (2006a) for a system comprising DI-water/octadecane-Span 80. In Fig. 5.11 the droplet length is presented for different surfactant concentrations ranging from 0.1 to 4% w/w at three different continuous phase flow rates 0.1 μl/min, 0.2 μl/min and 0.8 μl/min, and a constant aqueous phase flow rate of 0.2 μl/min. It was observed that the droplet length decreases with an increase in surfactant concentration primarily due to a decrease in the interfacial tension between the two immiscible phases.

The influence of the flow rate of the continuous phase on the length of droplets produced at above 0.8% surfactant concentrations was investigated. Fig. 5.12 shows the effect on droplet length of surfactant concentrations in the range 0.8 % to 4 % by weight over a range of flow rates of continuous phase. The purpose of this study was to focus on the transition of wettability of PDMS. The droplet length was found to be approximately independent of the surfactant concentration for concentration levels in excess of 2 wt.%. This is due to the

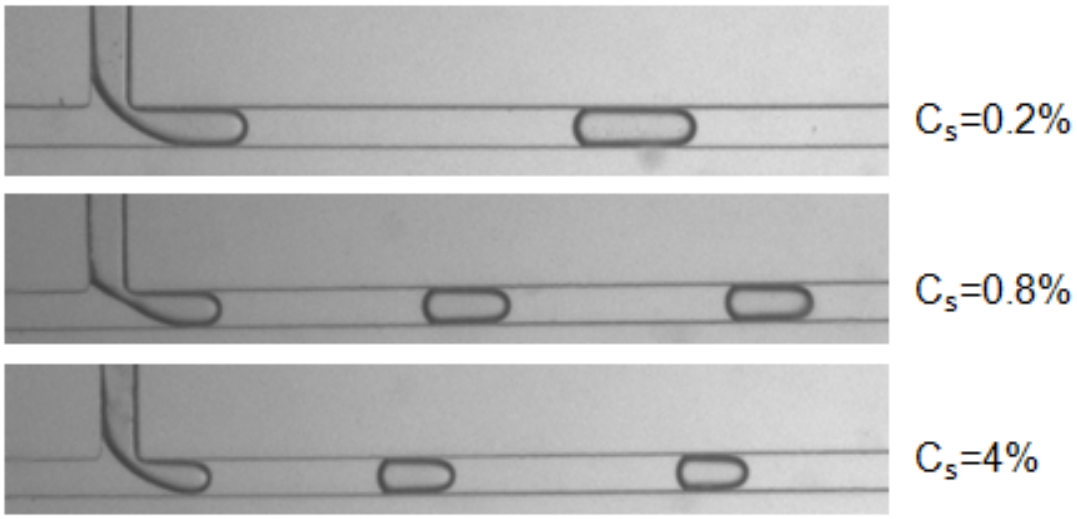

Fig 5.10. Photographic image showing the variation of the droplet length corresponding to the concentration of surfactant in the oil phase. The dispersed phase flow rate was Q_d=0.2μl/min and the continuous phase flow rate was Q_d=0.8μl/min.

fact that the interfacial tension reaches its minimum value when the surfactant concentration is higher than critical micelle concentration (CMC). The effect seems to be more prominent as we move towards the higher oil flow rate (Q_c $>$ 0.4 μl/min). Hence, we can also qualitatively describe the CMC for the microchannel which is otherwise quite difficult to determine accurately as the interfacial tension measurement between the two phases in a microchannel is still not well developed compared to those on macroscale.

It was observed that the surfactant effect is more prominent at high flow rate ratios ($Q \gtrsim 1$) or lower oil flow rates than for high oil flow rates. This is due to the fact that for lower oil flow rates the interfacial forces dominate over the shear forces and therefore the difference in droplet size achieved by altering the surfactant concentration is prominent. The same effect is not significant for high oil flow rates or for low flow rate ratios ($Q \lesssim 1$) due to the dominance of shear forces over interfacial forces. Therefore, the generation of uniform, stable

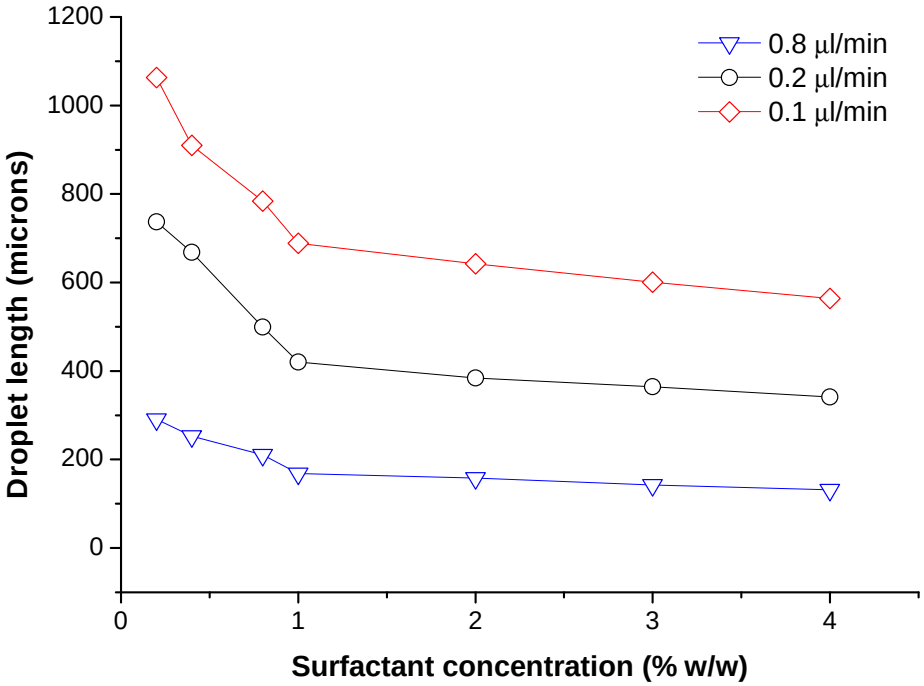

Fig 5.11. Droplet length plotted against surfactant concentration for three different oil flow rates. A constant dispersed phase flow rate of Q_d=0.2μ l/min was used.

droplets at low oil flow rates without surfactant is difficult.

5.6.2 Effect of flow rate ratio on droplet length for different surfactant concentrations

Fig. 5.13 presents the droplet lengths for different flow rate ratios. The concentration of surfactant in mineral oil was kept fixed at 4%. Fig. 5.14 shows the micrographs of droplets generated in mineral oil containing 4% surfactant with different flow rate ratios. It was observed from both figures that the droplet length decreases as the flow rate of the continuous oil phase is increased. The curve fitting analysis in Fig. 5.13 shows that the length of droplets scales with

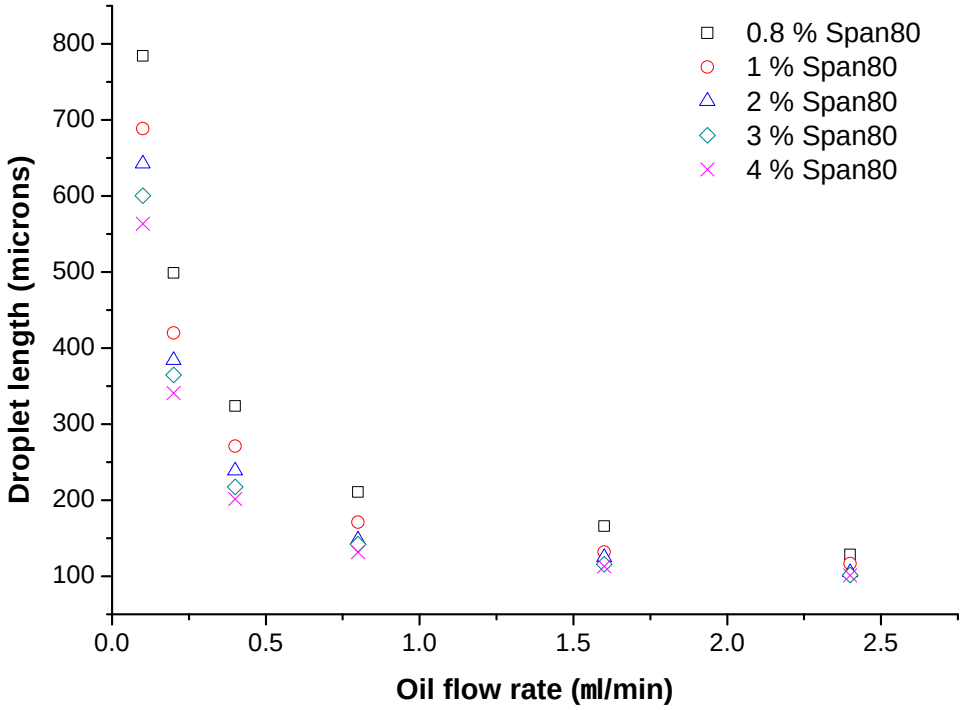

Fig 5.12. Length of droplets versus flow rate of mineral oil with added higher concentrations of Span 80 with constant dispersed phase flow rate of Q_d=0.2μl/min.

$Ca^{-0.25}$ which corroborates with the scaling obtained in experiments performed by Van der Graaf et al. (2006).

The ease of movement of droplets due to the increased thickness of the thin film between the droplet interface and the channel wall as a consequence of increasing surfactant concentration reduces the distance between two droplets at a given fixed flow rate ratio between two phases as shown in Fig.5.15.

5.6.3 Surface wetting

Dynamical processes occur at the region of intersection of the main channel with the lateral channel of the microdevice due to interfacial instabilities. The

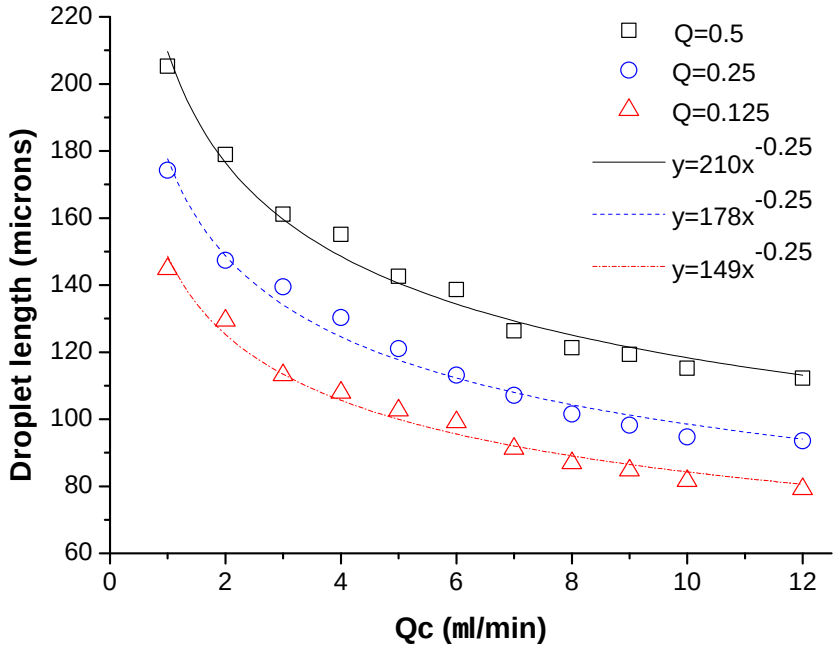

Fig 5.13. Length of droplets plotted against flow rate of mineral oil containing 4%w/w of Span 80 surfactant for three different values of flow rate ratio, Q.

addition of a surfactant such as Span 80 to a carrier oil changes the wetting properties of the microchannel walls. Therefore, in order to achieve stabilized initial conditions, for each of our experiments, the carrier fluid of oil containing a known concentration of surfactant was pumped into the main channel at least 1 hr before the dispersed phase was released. Also, before each experiment the channels were cleaned with ethanol and dried in order to reduce the risk of contamination.

The adsorption of surfactants and their mixtures on solid surfaces can modify their hydrophobicity. Thus the addition of surfactant to a mineral oil can enhance the capability of the oil to wet the hydrophobic solid surface of a microchannel. Most surfactant molecules consist of two parts, a hydrophilic head

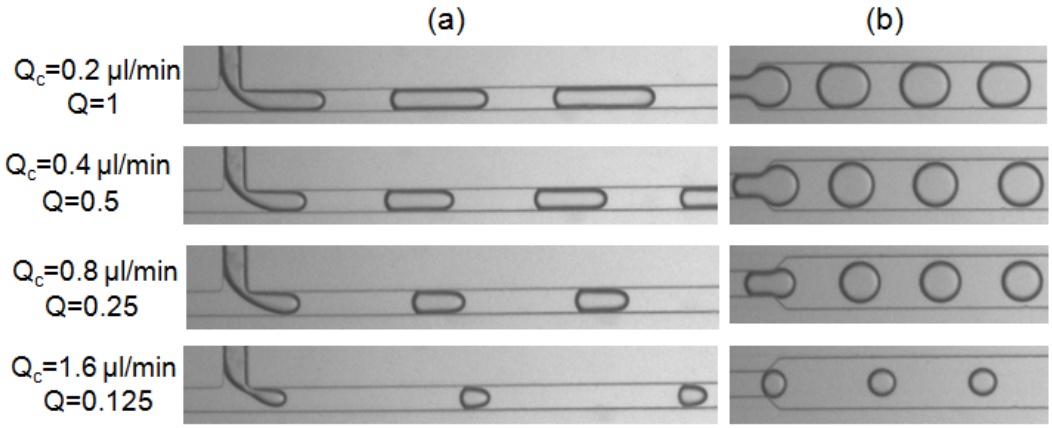

Fig 5.14. Droplet formation images using Cs=4% and for fix flow rate Q_d=0.2μ l/min. (a) T-junction where droplets of water are shear off by oil phase (b) flow focussing section where droplets are subsequently relaxed to the spherical shape.

group and one to four hydrophobic tails. Span 80 comprises a hydrophilic head (sorbitan) and a single hydrophobic tail (oleic acid). The orientation of surfactant molecules at a surface or interface determine how that surface or interface will be affected by the adsorption, i.e., whether it will become more hydrophobic or more hydrophilic. If the hydrophobic tail group of an adsorbed surfactant points away from the surface or along the surface the result will be decrease in water wetting and an increase in oil-wetting (Paria and Khilar, 2004).

The wettability of microfluidic channel walls can be quantified by the 'contact angle' the liquid forms with the channel surface. During the motion of a droplet the contact angle it forms with the channel wall on the upstream, or de-wetting side, is referred to as the receding contact angle. The angle formed on the downstream, or wetting side, is referred to as advancing contact angle (Dussan, 1979). The advancing and receding contact angles are usually denoted as θ_a and θ_r respectively. The advancing contact angle is always greater than or equal to the receding contact angle i.e., $\theta_a \geq \theta_r$. The difference $\theta_a - \theta_r$ is known as the

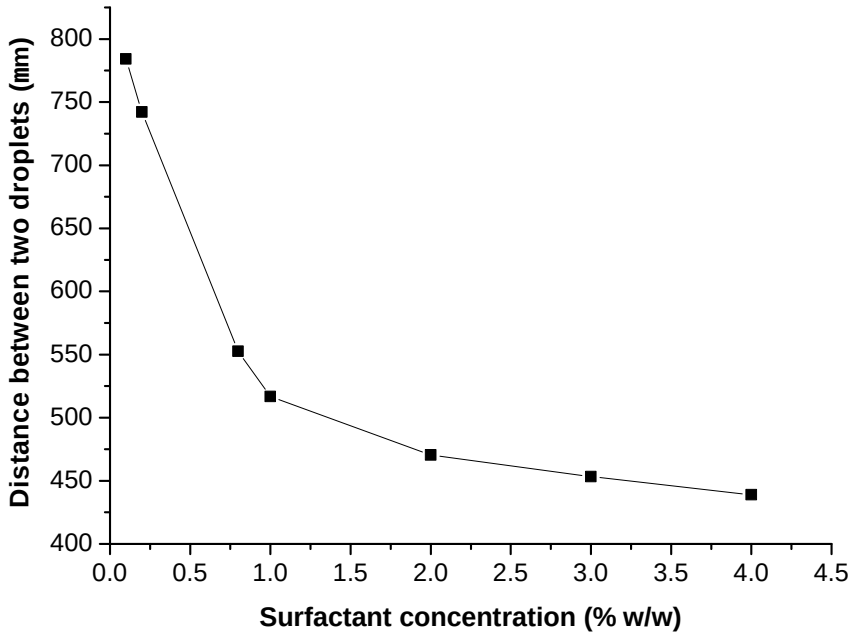

Fig 5.15. Distance between two consecutive droplets plotted as a function of the concentration of surfactant. Dispersed and continuous phase flow rates were kept fixed at Q_d=0.2 μl/min and Q_c=0.8 μl/min respectively. The flow rate ratio was Q=0.25.

contact angle hysteresis (Dorrer and Ruhe, 2006). The underlying mechanisms of hysteresis and of dynamic contact angles are not yet fully understood and depend on a number of parameters including surface roughness and surface chemistry (Extrand, 2002). However, in experiments incorporating a moving contact line, it is possible to observe the existence of these two contact angles.

Figs. 5.16 and 5.17 show the receding and advancing contact angles of detached droplets in a microchannel corresponding to carrier oils containing different surfactant concentrations at constant flow rate ratios of Q=1 and Q=0.125 respectively. Both receding and advancing contact angles increase as the surfactant concentration is increased. At a given surfactant concentration level

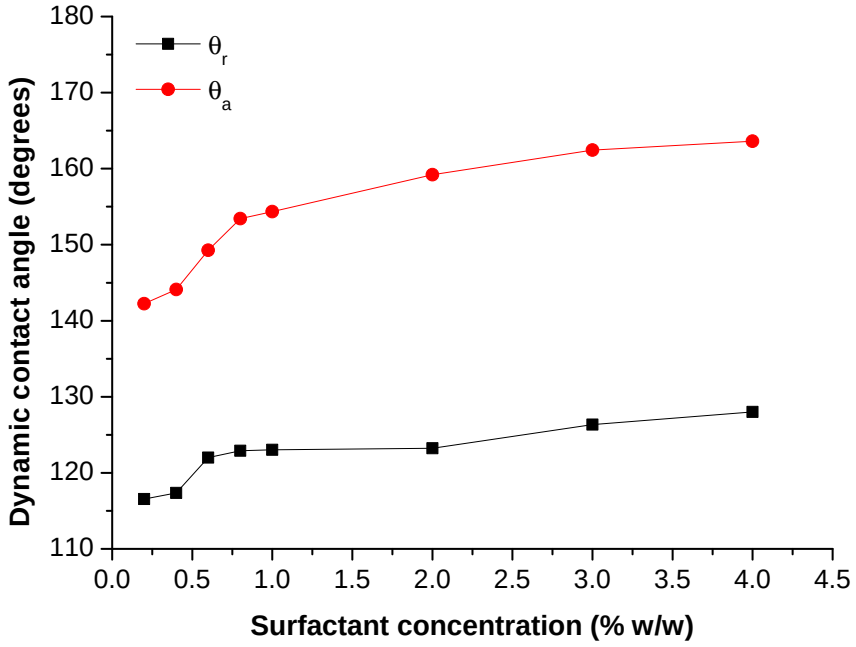

Fig 5.16. Advancing and receding contact angles plotted against surfactant concentration for a flow rate ratio of Q=1.

lower values of θ_r and θ_a were observed at a flow rate ratio of Q=1 than at Q=0.125.

Beyond the transition surfactant concentration which was observed at a 1 % w/w of surfactant concentration, stable and uniform water droplets were observed. This might be due to the dynamic surfactant adsorption on both liquid-liquid and liquid-solid interfaces in the microfluidic channel. Also, the uniformity of droplets is observed to be altered gradually beyond Q >2 at all surfactant concentrations and eventually the two phases flow parallel to each other such that neither of the phase completely wets the microchannel walls. In this case, when the aqueous phase exhibits stratified wetting instead of confined dispersion, the dynamic contact angles are assumed to be 0°.

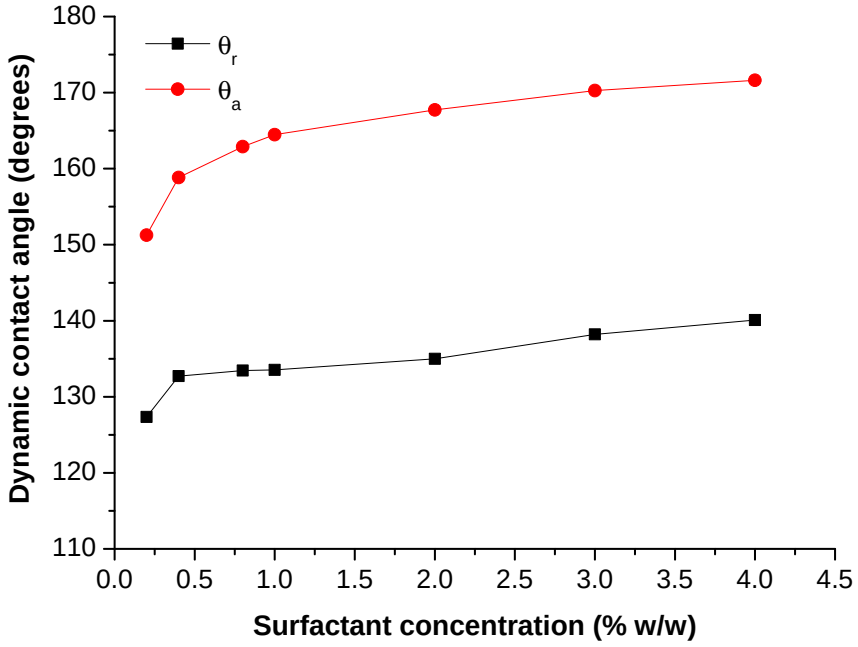

Fig 5.17. Advancing and receding contact angles plotted against surfactant concentrations for a flow rate ratio of Q=0.125.

5.7 Conclusions

In this chapter we have performed direct measurements of interfacial tensions between DI-water and mineral oil and static contact angles of DI-water on a PDMS surface surrounding an oil media, across range of concentrations of Span 80. The data provide a basis for the dynamic flow experiments that were conducted in a T-shaped PDMS microfluidic device. The effects of wetting properties between the mineral oil and DI-water on droplet formation were investigated. Droplet lengths were measured for different surfactant concentrations (C_s) and it was observed that droplet length decreases as C_s increases and eventually becomes almost independent of C_s at the CMC level. The value

of the CMC level at microscales is $\sim$ 1% w/w which is slightly higher than that measured at macroscales due to large surface to volume ratio associated with microscale flows. Therefore, it can be concluded that at microscales where accurate interfacial tension measurements are difficult to obtain, an alternative way to estimate CMC is from the behaviour of changing droplet length with C_s. This is an important original finding which can be applied to different combination of surfactants and oils.

From the dynamic contact measurement, it was found that dynamic contact angles decrease as the flow rate ratio between the dispersed and continuous phase fluids is increased. Dynamic contact angles were observed to increase as the level of surfactant concentration in the carrier oil increased. Stable and uniform water droplets were observed in the microchannel and concentrations in excess of the transition surfactant concentration level. The wetting dynamics of droplets in the presence of a surfactant mixture depend on a number of factors, such as the quality of microchannel surface, viscous effects, interfacial tension between liquid-liquid interfaces and the adsorption of surfactant at solid-liquid interfaces.

6

Hydrophilic surface modification of PDMS microchannel for O/W and W/O/W emulsions

A surface modification method for PDMS microchannels is presented herein. The method is based on an inline microplasma polymerization technique. The surface treatment changes the PDMS microchannel surface wettability from hydrophobic to hydrophilic. This is a challenging task due to the fast hydrophobic recovery of PDMS. The hydrophilic modification of a PDMS device allows the formation of highly monodispersed droplets of oil in water (O/W). Furthermore, the generation of monodispersed water-in-oil-in-water (W/O/W) double emulsions was successfully achieved by connecting in series a hydrophobic microchip with the modified hydrophilic microchip. A novel channel blocking technique to spatially pattern the surface wettability of a single microchip is also presented for generating W/O/W emulsions.

6.1 Introduction

Due to the large surface to volume ratio characteristic of microfluidic devices, the channel surface plays a vital role in a wide range of applications. Conventional methods such as high shear homogenizers (McClements, 1999) and rotor/stator systems (Urban et al., 1999) are usually inadequate for generating high quality microemulsions due to the large drop size distribution. The resultant large droplet size distributions are problematic for sorting and detection which require uniformity of droplets. Preparation of double emulsions using these methods is even more complex as high shear rates result in coalescence of internal droplets by the external phase. However, with the advent of microfluidic droplet systems, several problems that arise in conventional emulsion formulation systems have been resolved. The microdroplets can be prepared and controlled precisely in microfluidic chips such that their splitting, merging and sorting can be easily achieved. In addition to single emulsions, microfluidic plateforms are capable of producing highly uniform double emulsions (Utada et al., 2005). Both types of double emulsions, oil-in-water-in-oil (W/O/W) and water-in-oil-in-water (W/O/W) have their potential usage in food, cosmetics and pharmaceuticals (Matsumoto et al., 1976; De Luca et al., 1991). W/O/W are the most commonplace double emulsions where small water droplets are enclosed within the larger oil droplets, dispersed in a continuous water phase. These emulsions can be utilized in drug delivery systems (Shum et al., 2008a,b).

Besides controlling emulsion production through geometrical constraints, control of wettability of microchannel walls is also a necessary requirement. Hydrophobic surface modifications of glass based microchannels have been carried out in the past few years to form water-in-oil emulsions. Okushima et al. (2004)

prepared both water-in-oil-in-water (W/O/W) and oil-in-water-in-oil (O/W/O) double emulsions in a channel geometry that comprised two T-junctions fabricated in series on a single glass microchip, and also in two-separate T-shaped microchips connected in series. In each of these arrangements, the surface of one of the T-junctions was hydrophobically modified in order to enable the formation of water-in-oil droplets. Although, well developed methods exist for the modification of glass microchips, the fabrication of glass microchips is costly and time consuming. PDMS devices, however, are reusable and can be readily replicated due to the low cost of the fabrication technology which is based on photolithography. In addition, PDMS is a highly transparent, non-toxic and biocompatible material. It should be noted, though, that despite its numerous advantages, limitation occur in the use of PDMS for the formation of oil-in-water droplets and for several other applications where the wetting of the microchannel surface with aqueous streams is essential. Due to the intrinsic hydrophobic property of PDMS, hydrophilic surface modification poses a great challenge. Stable coatings are usually regarded as the most effective way of achieving hydrophilic surface modification. Ideally permanent coatings should be stable and unlike dynamic coatings, should not need to be regenerated. Typically, modification of PDMS surfaces is based on oxygen plasma treatment. The modified surface is short lived with hydrophobic recovery initiated after a few hours. Barbier and co-workers (Barbier et al., 2006) deposited plasma polymerized acrylic acid coatings onto unbonded PDMS microchips and were the first to implement them to form double emulsions. Their experiments were performed in a vacuum with limitations for implementing on a laboratory scale due its expense. Recently plasma treatment at atmospheric pressure has become a promising technology due its reduced equipment cost and the possibility of in-line and batch sys-

tem processing. In this work, a rapid and high-precision method for localized plasma-treatment of bonded PDMS microchannels at atmospheric pressure is demonstrated. The atmospheric pressure plasma polymerized PDMS channel remained hydrophilic for a relatively long period of time. The microchannels were successfully modified to produce oil droplets in water and water-in-oil-in-water double emulsions.

6.2 Experimental setup

6.2.1 Coating setup

The plasma coating system for the microchannel is schematically presented in Fig. 6.1. The main flow of helium (He) gas is controlled by a mass flow controller (MFC2). The gas bubbler contains an acrylic acid (AA)(Sigma-Aldrich, 99%). The monomer vapors were introduced into the plasma via a bubbler carried by a secondary He flow. The secondary He flow rate was controlled by another mass flow controller (MFC1). The upper electrode (stainless steel hollow tube) was connected to a high voltage AC power source and a ground electrode was placed below the microchip.

6.2.2 Emulsification setup

Deionized (DI) water was used as the innermost phase in the formation of water-in-oil-in-water emulsions. The middle phase comprised mineral oil containing 4% w/w of Span 80. The outermost phase was DI water. In addition to this, fluorinated oil and sunflower oil were also used to form single oil in water emul-

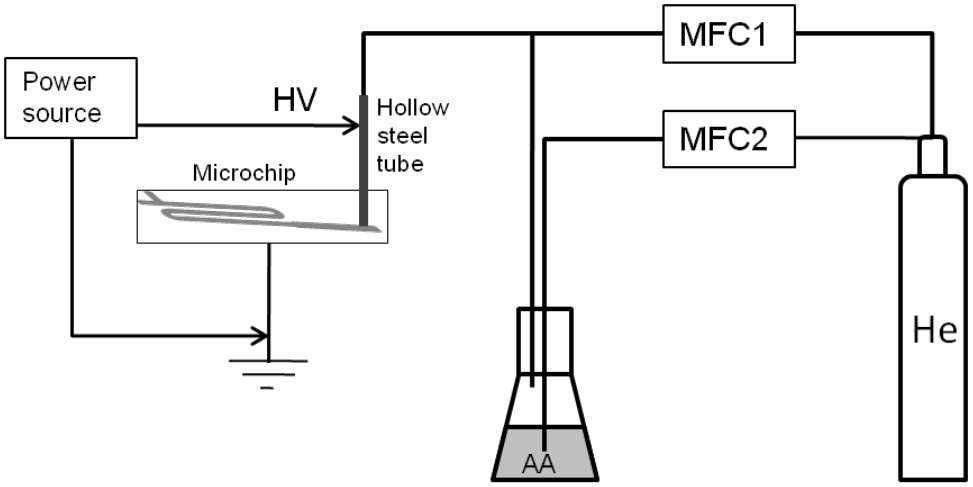

Fig 6.1. Schematic of the plasma coating setup for modification of the surface of the PDMS microchip at atmospheric pressure.

sions. All chemicals were purchased from Sigma-Aldrich except the sunflower oil which was obtained from a local supermarket. Details of the equipment used for the droplet formation experiment were described in chapter 5. In brief, two syringe pumps were used to control the internal and intermediate flow rates in order to form water-in-oil droplets, and an additional syringe pump was used to control the external water phase flow rate to form water-in-oil-in-water double emulsions. A CCD camera mounted on an inverted microscope was use to record the single and double emulsion images. Images were analyzed afterwards using ImageJ (http://rsb.info.nih.gov/ij/) software. A photograph of the experimental setup is shown in Fig. 6.2.

6.3 Coating of PDMS surface

Flow parameters of the monomer and He gas were chosen so as to optimize the plasma coating of a PDMS slab with acrylic acid. These reference samples were

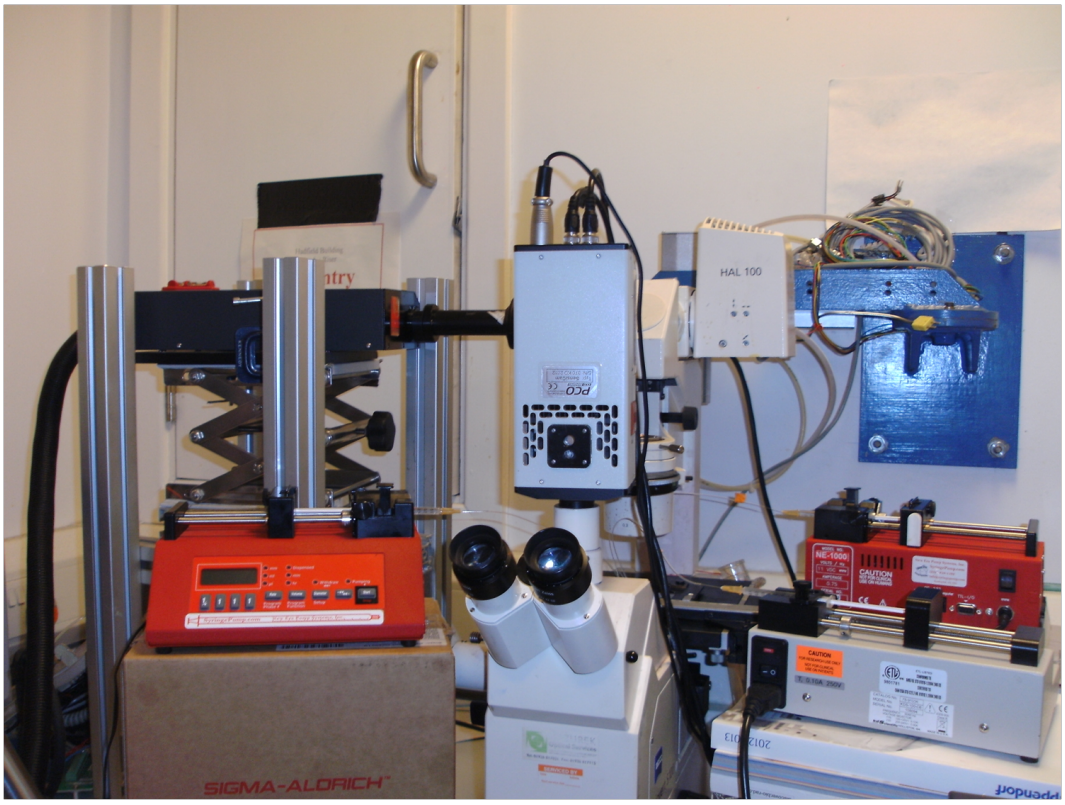

Fig 6.2. Experimental setup for the preparation of double emulsion.

deposited in order to characterize the plasma polymerized films. The process was carried out using a dielectric barrier discharge (DBD) plasma jet which was obtained using a simple configuration of electrodes as shown in Fig. 6.3. Plasma was generated in the form of a jet in the main tube of the polypropylene T-connector which had an outer diameter of 4.76 mm. The side tube of the T-connector was used to feed the monomer-gas mixture. The polypropylene T-connector was safely used to generate the plasma jet due to the low temperature of the plasma ($\sim 46^\circ$C at 5W). A central steel wire with a sharp tip was aligned axially using a supporting BD plastic syringe. This central wire acts as a high voltage electrode and the ring electrode wrapped around the bottom end of the jet pipe is used as a ground electrode. The thickness (0.5 mm) of the

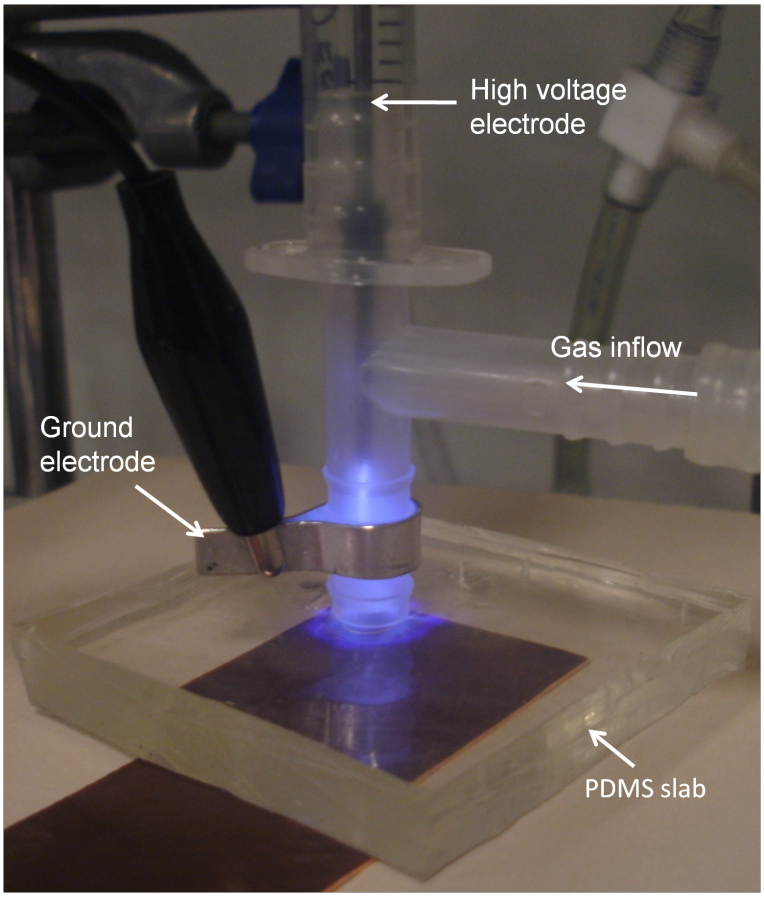

Fig 6.3. Treatment of PDMS slab.

polypropylene pipe acts as a dielectric barrier. Fig. 6.4 clearly shows that the hydrophilicity of the PDMS surface was achieved using this novel configuration as the water contact angle (WCA) decreases from 107° for bare PDMS to 9.16° for coated PDMS .

DBD is a non thermal plasma and therefore it processes a low temperature. The plasma temperature remains typically in the range 40°- 60°C, therefore it is thermally non-aggressive for PDMS treatment and lowers the risk of damage to the surface.

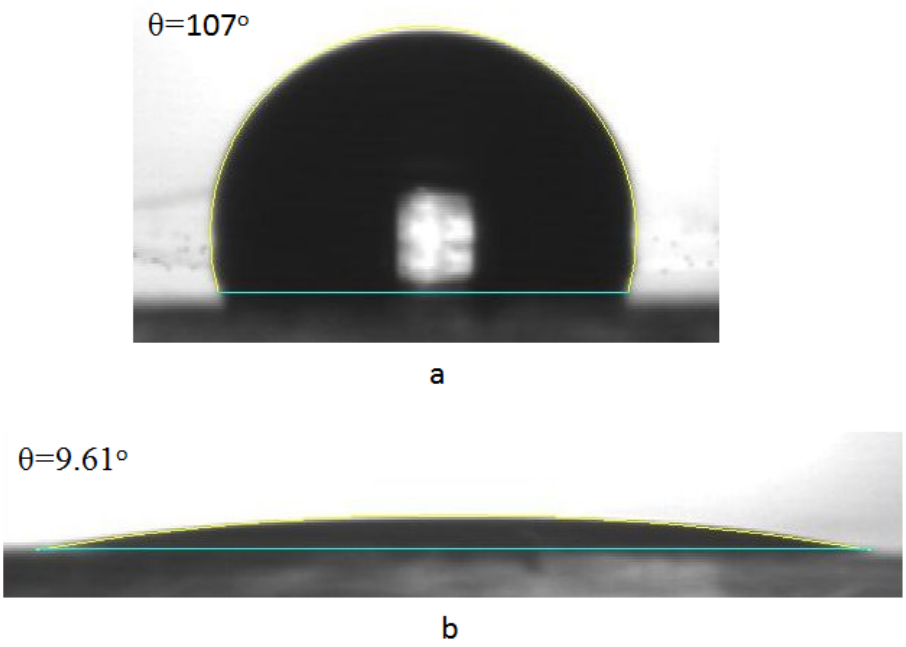

Fig 6.4. a) Bare PDMS b) Treated PDMS with PAAc.

6.4 Surface coating of microchip using DBD plasma

The modification of internal surfaces within a sealed microfluidic device are potentially promising for achieving a broad range of physical and chemical properties of microchannel surfaces that are difficult to attain by wet-chemical processes or plasma processes in vacuum. By using a suitable electrode arrangement, the coating of a selected segment of a microfluidic device can be localized.

In the current approach, a DBD microjet was used to localize microplasma in a microfluidic device at atmospheric pressure which is difficult or almost impossible to achieve under vacuum due to the difficulties of feeding the gas/monomer

flow into the sealed microchannel. An important feature of the proposed approach lies in its parallelization such that the modification of multiple microfluidic channels can be achieved simultaneously.

6.4.1 Electrode configuration for onchip DBD plasma

The configuration used for plasma generation inside the microfluidic chip is shown in Fig. 6.5. A stainless steel hollow tube was used as a high voltage thin electrode. The concentrated high voltage electric field that emanated from the sharp tip of the steel tube helped to sustain a stable glow discharge in the microchannel. The outer diameter of the steel tube was chosen to ensure that it fitted into the outlet in order to avoid gas leakage. A copper sheet of thickness 0.6 mm was used as a ground electrode. This was placed underneath the microchip. The microchip was formed from two PDMS sheets bonded together. The lower PDMS sheet of thickness 2 mm acted as a dielectric barrier.

6.4.2 Plasma deposition process

The PDMS channel surface was activated in-line via the He plasma for about 1 min. A mixture of He gas and a gaseous precursor of acrylic acid monomer was fed into the microchannel in order to deposit a thin layer of acrylic acid coating onto the walls of the microchannel. All process parameters such as the flow rates of He and the monomer, and power from plasma source, were optimized in order to sustain a stable plasma and to effectively deposit a PPAA film onto the microchannel surface. The deposition time was about 8 min. The deposited thin film was then cross linked by post treatment using He plasma for approximately 2 min. The plasma power was kept at 4-5 W throughout the deposition process

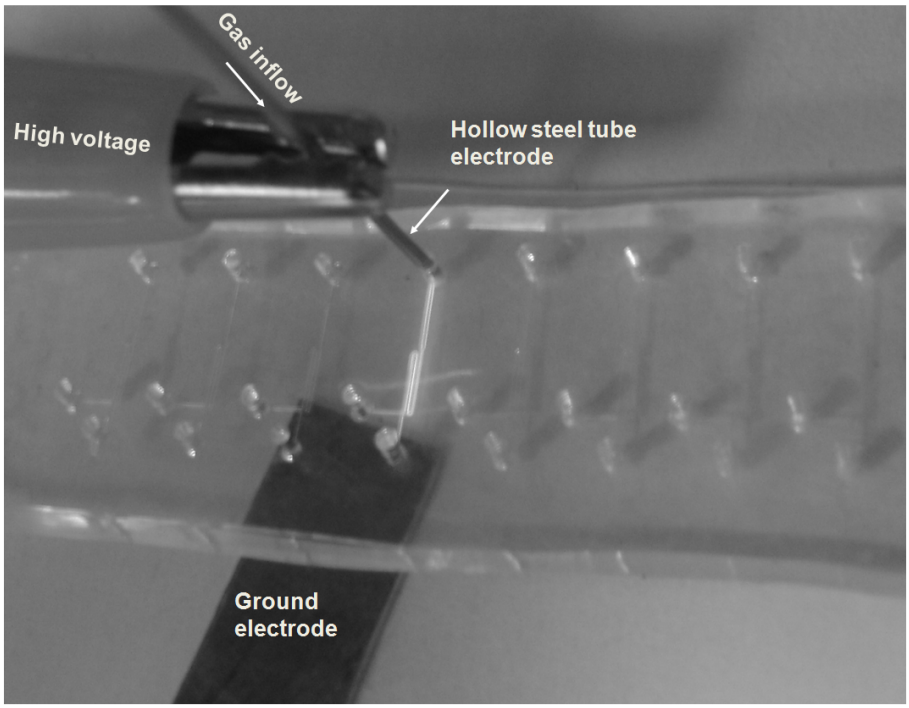

Fig 6.5. Plasma treatment of PDMS chip.

to gently treat the PDMS surface. The flow rate of pure helium was kept at 400 sccm through the deposition process and that of acrylic acid was kept at 20 sccm. The pre-treatment of the PDMS surface with plasma should not be longer than 1 min otherwise cracks may occur on the surface. In a modified hydrophilic microchannel water completely wets the channel surface and therefore the WCA is 0° with the channel surface. The deposited film was further characterized by on-chip plasma emission spectroscopy using USB2000 spectrometry (Ocean optics). An optical fiber for collection of the emitted light spectrum is placed directly above the microchannel during the pretreatment with He-plasma as well as during deposition of acrylic acid. Hence, due to the optical transparency of PDMS, the spectrum was collected without losing any light signals. Fig. 6.6 shows the plasma emission spectrum of pure helium along with helium mixed with acrylic acid gaseous monomer. The peaks of the plasma emission spectra

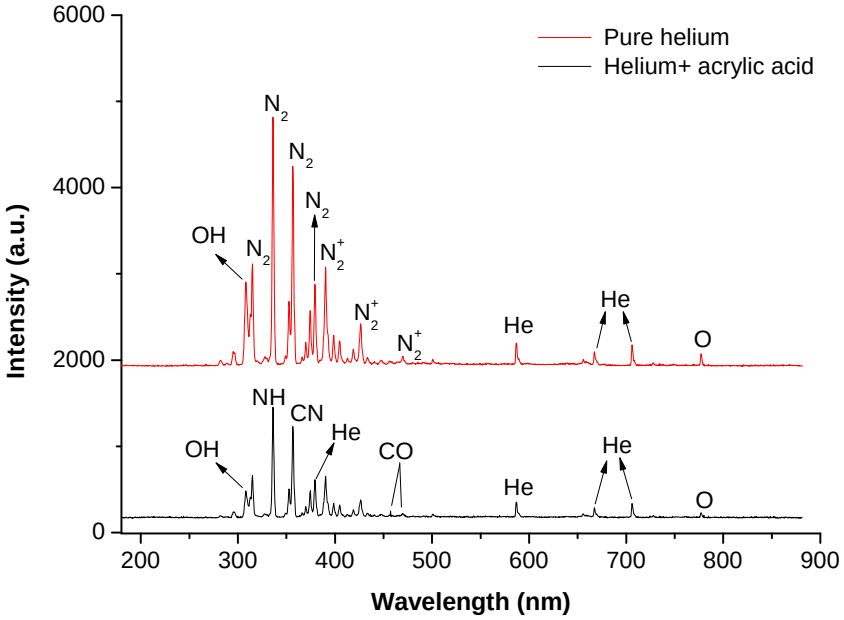

Fig 6.6. Plasma spectroscopy of helium (top plot) and helium mixed with acrylic acid (lower plot).

of helium were identified as OH at 309nm, N_2 at 315, 337 and 357nm, N_2+ at 391nm, He at 380, 587, 668 and 706nm and, O at 780nm (Chen al., 2008; Tran al., 2009; Massines and Gouda, 1998). Peaks corresponding to hydroxyl radical, nitrogen and oxygen indicate that the discharge channel is contaminated with air. When acrylic acid was mixed with helium in order to achieve deposition in the microchannel, peaks of NH at 337nm, CN at 359nm and CO at 457nm and 470nm were observed in the emission spectrum. In this case it was observed that the intensities of the emission spectral lines decreased, which is most likely due to the use of helium metastables for breaking the chemical bonds of acrylic acid during additional reactions. Furthermore, spectral lines of NH at 337nm, and CN at 359nm indicate that monomer fragmentation takes place during the plasma deposition process.

6.5 Formation of oil-in-water microdroplets

Oil-in-water emulsions were successfully prepared in the same PDMS microfluidic device after modification of the channel surface to hydrophilic. As a result of this modification, water now preferentially wets the channel walls instead of oil, and consequently the formation of oil droplets in water is made possible. Droplets of oil-in-water were continuously produced in modified microchips for a wide range of flow rates and were observed for about 4 hrs. During this observation period the film was stable and no degradation was noticed. The same device was connected in series with a hydrophobic device to produce double emulsions and was reused several times over a 4 week period without any change in its hydrophilic character. Microfluidic droplet formation experiments were performed using a continuous phase of deionized water and a dispersed phase of mineral oil. Fig. 6.7 is a snapshot of monodispersed mineral oil droplets formed at constant flow rate of 1 μl/min and water flow rates of 4 μl/min, 8 μl/min and 16 μl/min respectively. The length of mineral oil droplets corresponding to a range of water flow rates from 1 μl/min to 40 μl/min are presented in Fig. 6.8. The droplet size decreases with increasing flow rates of the continuous water phase for a specific flow rate of the dispersed oil phase. The droplet size increases with increasing flow rate of the disperse phase which corroborates with previous findings (Thorson et al., 2001; Nisisako et al., 2002; Xu et al., 2006b). Fig. 6.8 confirms that the oil droplet size was precisely controlled by changing the water flow rate. Uniformity of the droplet size was reproducible under different experimental conditions. Furthermore, droplets of fluorinated oil (FC-40) with a low viscosity of 3.4 mPa.s and droplets of sunflower oil with a viscosity of 48.98 mPa.s, which is almost double that of the mineral oil, were

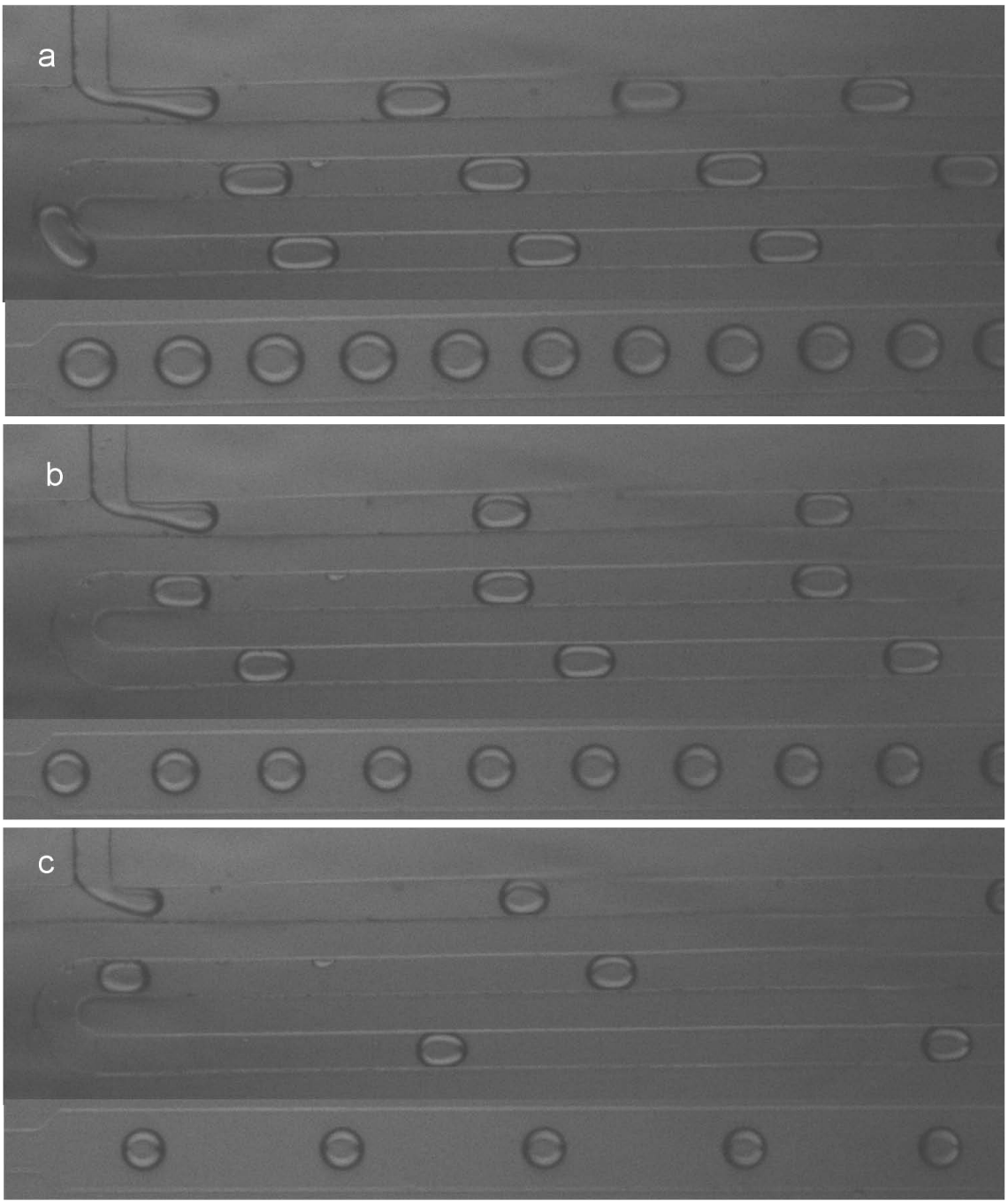

Fig 6.7. Snapshots of mineral oil droplet formation in water in a hydrophilic PDMS device, (a) Q_o=1 μl/min, Q_w=4 μl/min, (b) Q_o=1 μl/min, Q_w=8 μl/min, (c) Q_o=1 μl/min and Q_w=16 μl/min.

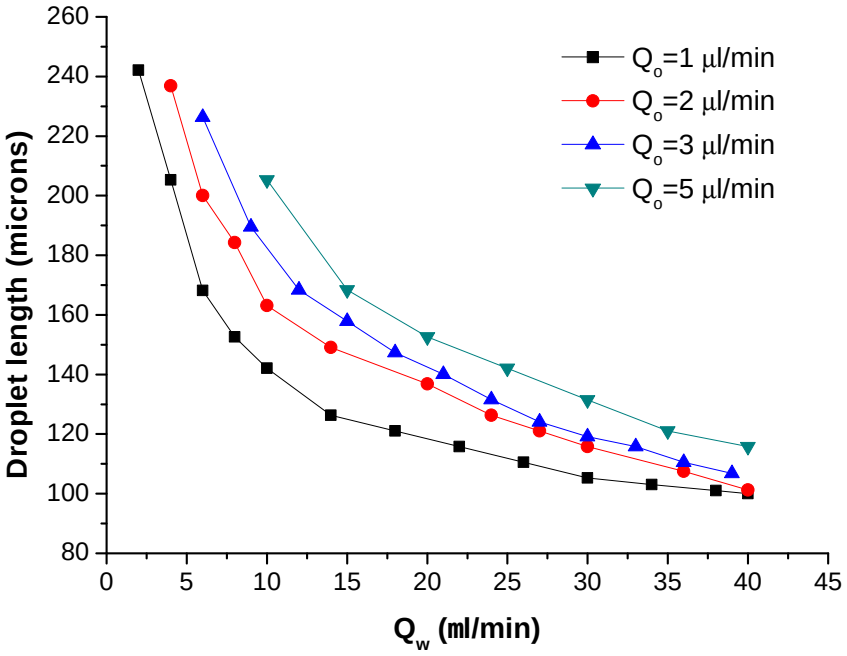

Fig 6.8. Influence of two phase flow rates on length of mineral oil droplets utilizing hydrophilic PDMS microchannel.

also formed in water and compared with those of mineral oil at a fixed oil phase flow rate of 3 μl/min as shown in Figs. 6.9 and 6.10. It can be seen that over the whole range of continuous phase flow rates considered, the oil droplet length decreases as the viscosity of the dispersed oil phase is increased.

6.6 Microfluidic system for double emulsions

The formation of a double emulsion is a two step process. In the first step, the aqueous phase acts as the dispersed phase and is sheared off by the carrier oil phase to form a water-in-oil emulsion. In the second step, an oil stream containing water droplets acts as the dispersed phase and is sheared off by another

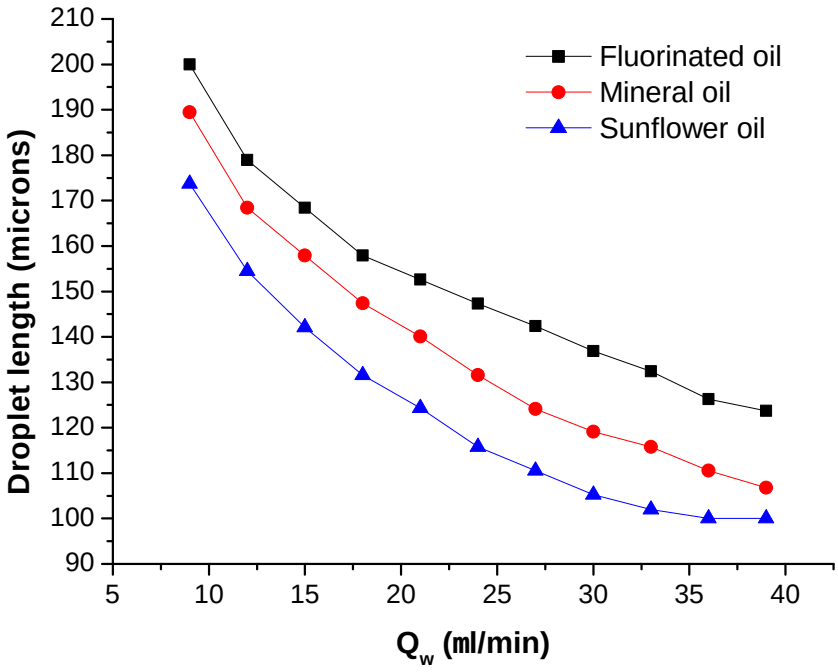

Fig 6.9. Effect of water phase flow rates on length of droplets generated using three different oils with varying viscosities at a fixed flow rate of 3 μl/min. Fluorinated oil (μ=3.4 mPa s), mineral oil(μ=24 mPa s) and sunflower oil (48.98 mPa s) were used.

continuous aqueous phase to form a water-in-oil-in-water double emulsion. This two step double emulsion formation process can be performed via a single chip module or by a double chip module. The generation of a double emulsion in a single chip module is usually difficult to achieve by means of surface modification. In order to form a double emulsion, either a part of the hydrophilic device needs to be modified to become hydrophobic, or part of the hydrophobic device needs to be modified into hydrophilic. However, in a two chip module, one of the microchips connected in series needs to be modified. This results in a flexible double emulsion system in terms of implementation for different types of configurations and their surface modification (Okushima et al., 2004;

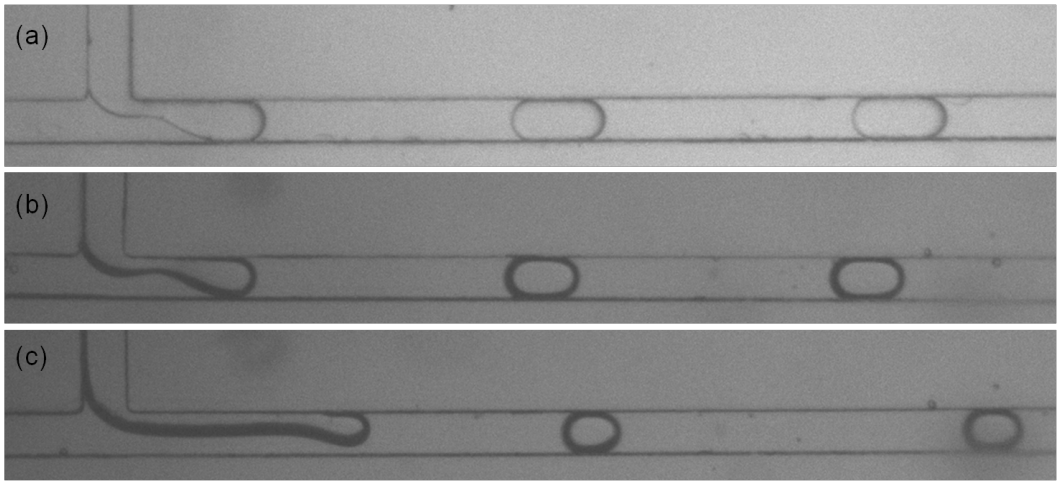

Fig 6.10. Droplets generated using three different oils with varying viscosities at fixed flow rate of 3 μl/min. (a) Fluorinated oil(μ=3.4 mPa s), (b) Mineral oil(μ=24 mPa s) and (c) Sunflower oil (48.98 mPa s). The flow rate of water is kept at 12 μl/min.

Nisisako, 2008).

6.7 Two microchip module

A schematic diagram of the double emulsion process using the two-microchip module is illustrated in Fig. 6.11. Two separate T-shaped microfluidic PDMS devices were used to generate double emulsions. Both microfluidic chips consist of the same T-shaped geometry with rectangular cross section channels. The generation of a water-in-oil emulsion in the first microchip results from the natural hydrophobicity of the channel. This microchip has a channel cross sectional area of 100 $\times$ 50 μm^2. DI water was used as the dispersed phase and mineral oil containing 4% of Span 80 surfactant was used the continuous phase. The second microchip contains a channel of 200 $\times$ 100 μm^2 cross-sectional area such that the aspect ratio remains the same as that of the first microchip. This mi-

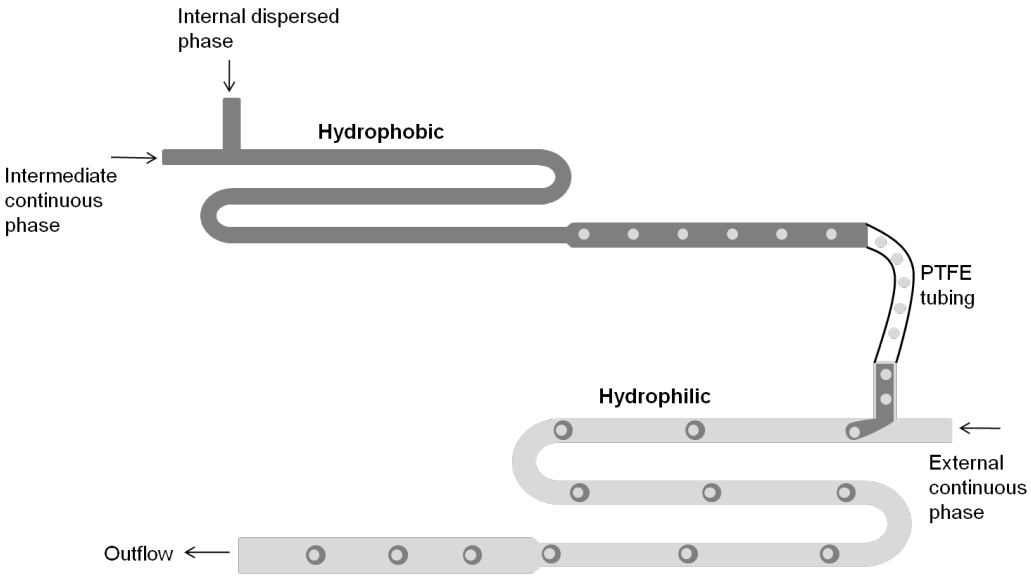

Fig 6.11. Schematic diagram of two-microchip module used for double emulsion.

crochip was made hydrophilic using the aforementioned localized microplasma polymerization technique in order to generate oil-in-water emulsions. In this step, mineral oil containing water droplets from the first microchip was used as the dispersed phase and DI water was used as an external carrier phase. The droplets of water generated in the first microchip, along with a carrier oil, were transported into the second microchip via a very small piece of PTFE tubing to form a water-in-oil-in-water double emulsion. The first microchip was elevated with respect to second microchip in order to avoid droplets from being pushed back by the external carrier phase into the second microchip as shown in Fig. 6.12.

6.7.1 Preparation of double emulsions

Fig. 6.13 shows photographic images of the formation of a double emulsion formation in the two-microchip module. The internal water droplet size in the

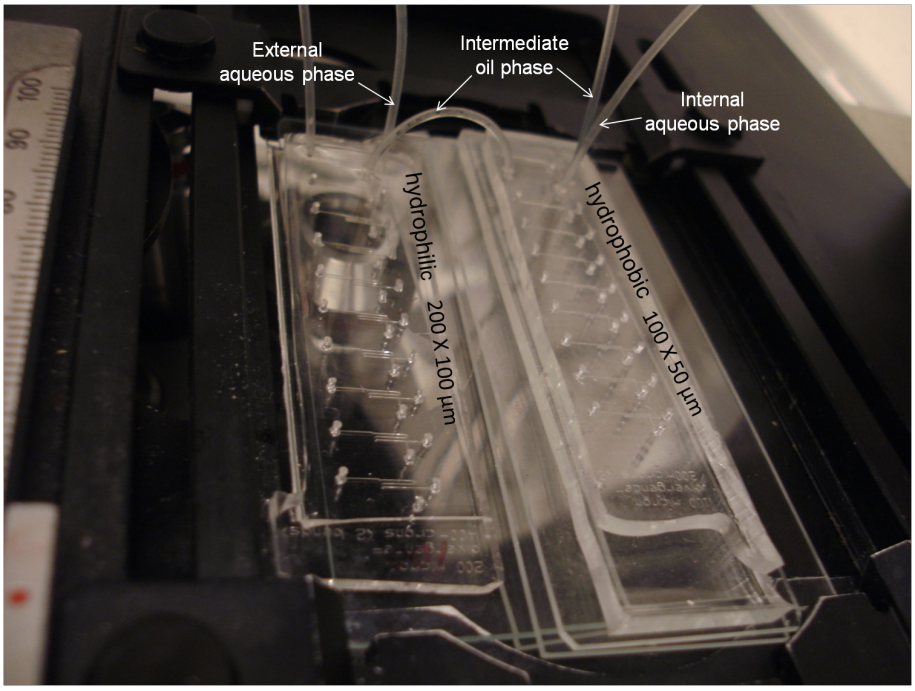

Fig 6.12. Photographs of experimental setup for double emulsion formation in the two-microchip module.

hydrophobic microchip can be controlled by altering the ratio of flow rates of the internal water phase to that of the middle oil phase. Fig. 6.14 shows the effect of the external water phase flow rate in the second microchip on intermediate oil droplet sizes for different flow rate ratios. We can write $Q_i = \frac{Q_{iw}}{Q_{mo}}$, where Q_{iw} is the flow rate of the internal dispersed water phase and Q_{mo} is the middle oil phase flow rate. The oil droplet sizes decrease with the external water phase flow rate but the internal water droplet size D_{iw} is not affected by any changes made to the external flow conditions at a constant flow rate ratio Q_i. Similar observations were also made in previously reported double emulsion data obtained using a two chip module by Okushima et al. (2004), where they have used a silane-coupling agent to modify one of the hydrophilic glass microchips to become hydrophobic. This suggests that the optimization

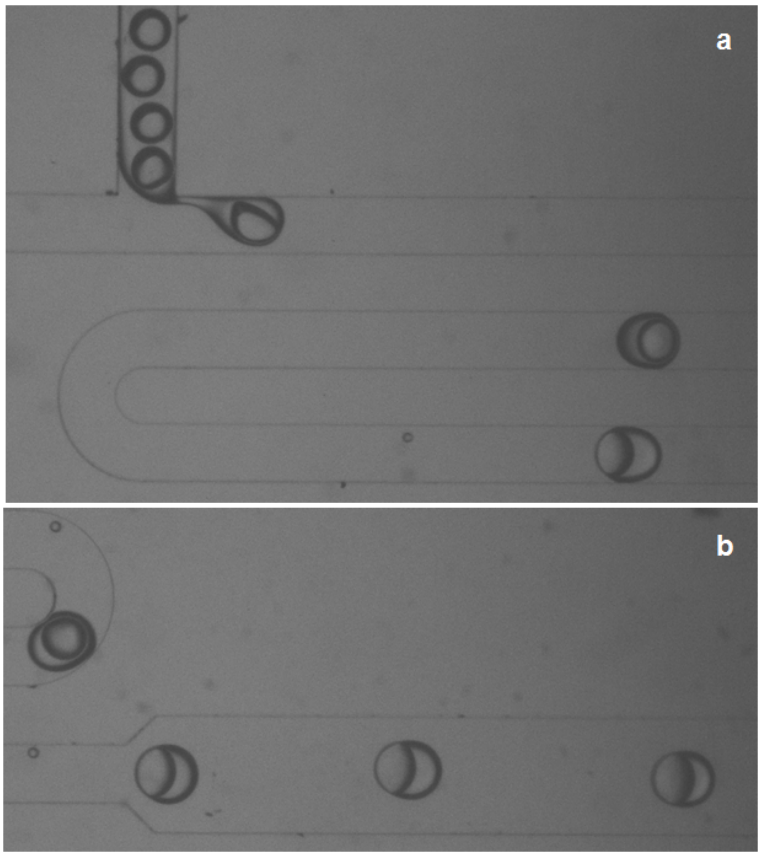

Fig 6.13. Snapshots of a water-in-oil-in-water emulsion generated using a hydrophilic PDMS device at (a) T-junction with Q_{iw}=1μl/min, Q_{mo}=2μl/min, Q_{ew}=60μl/min and (b) flowing down in the diverging section of the device.

of the flow rate ratio Q_i in a water-in-oil emulsion is necessary to obtain the appropriate droplet size that could be enclosed in an oil droplet in order to achieve regular encapsulation each time in the second T-junction device. It was observed that the regular encapsulation of water droplets within the middle oil droplets was obtained for Q_i=1, Q_i=0.5 and Q_i=0.25. In the cases where Q_i=1 and Q_i=0.5, single water droplet encapsulation within the oil drop was obtained, whilst in the case of Q_i=0.25 two water droplets that were enclosed within a single oil droplet as shown in Fig. 6.15 were obtained. The existence of an external aqueous phase flow rate beyond which each oil droplet encloses

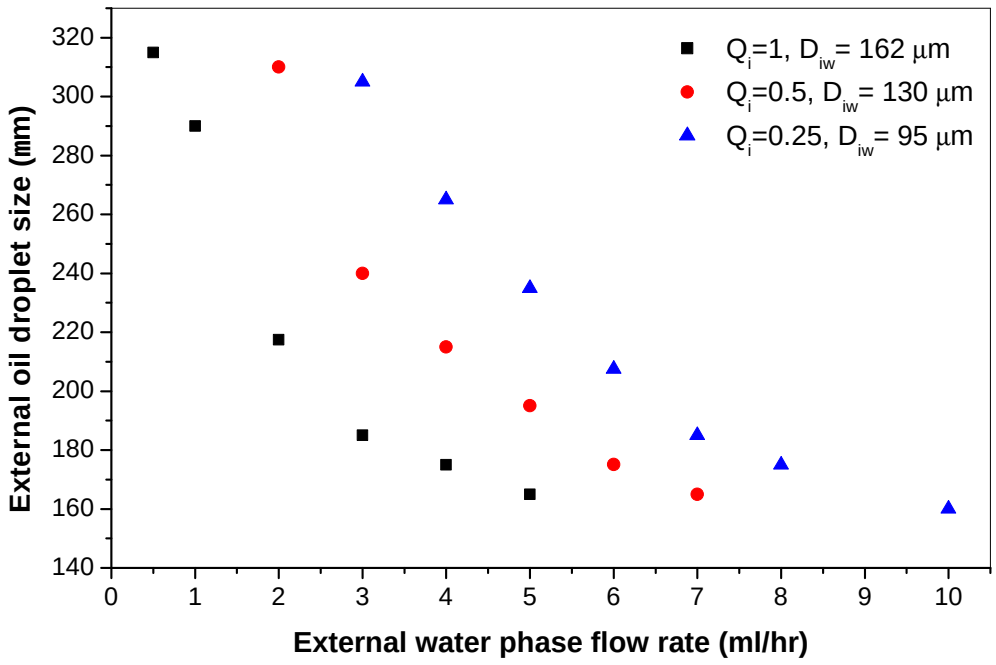

Fig 6.14. Effect of external water phase flow rate on water-in-oil-water emulsion.

a single aqueous droplet is probable e.g., in case of Q_i=0.5 a single droplet encapsulation in each oil droplet was observed when Q_{ew} was around 50 μl/min (3 ml/hr) and this scenario persists until the flow rate reached 117 μl/min. At Q_{ew}=117 μl/min (7 ml/hr), the oil droplet size becomes approximately equal to the size of the encased water droplet, which is the minimum possible size for an encased droplet to exist. Beyond this external flow rate the probability of water droplet encapsulation in oil droplets decreases. In this regime most of the oil droplets were observed to be generated without encapsulating a water droplet and eventually at higher external flow rates the number of encapsulating droplets became zero as the droplets started to push back into the first microchip. Therefore, the external phase flow rate needs to be carefully optimized in order to generate double emulsions where each oil droplet contains a

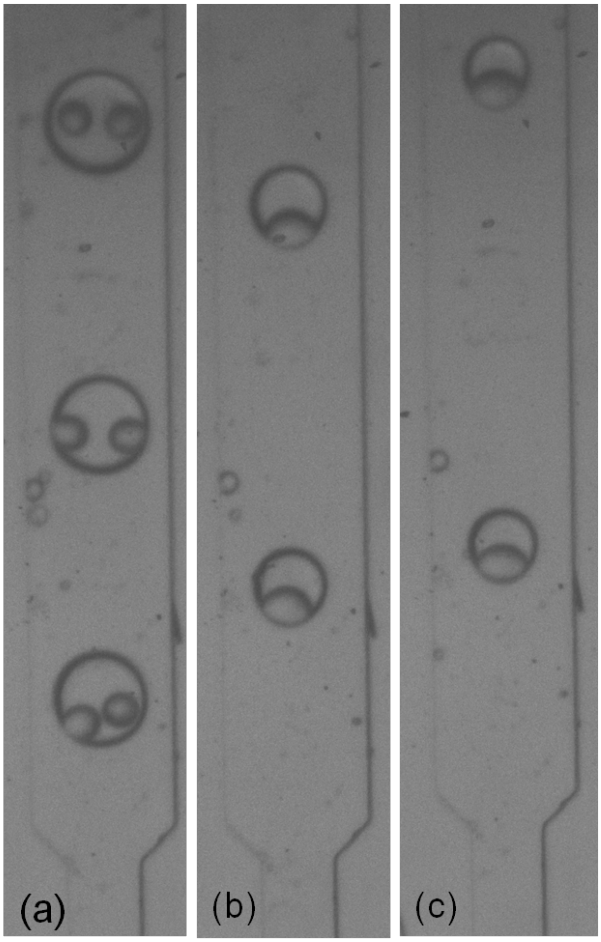

Fig 6.15. Snapshots of a water-in-oil-in-water emulsion generated using a hydrophilic PDMS device with Q_i=0.25, (a) Q_{ew}=2 ml/hr, (b) Q_{ew}=6 ml/hr and (c) Q_{ew}=8 ml/hr.

single water droplet. Double emulsion experiments were repeated three times in order to assess the reproducibility of the results.

6.8 Single microchip module

A single microchip containing two T-junction microchannels in cascade is shown in Fig. 6.16. A selective modification of a microchip was made using a plasma polymerization technique. Honey containing 20% w/w glycerol was injected

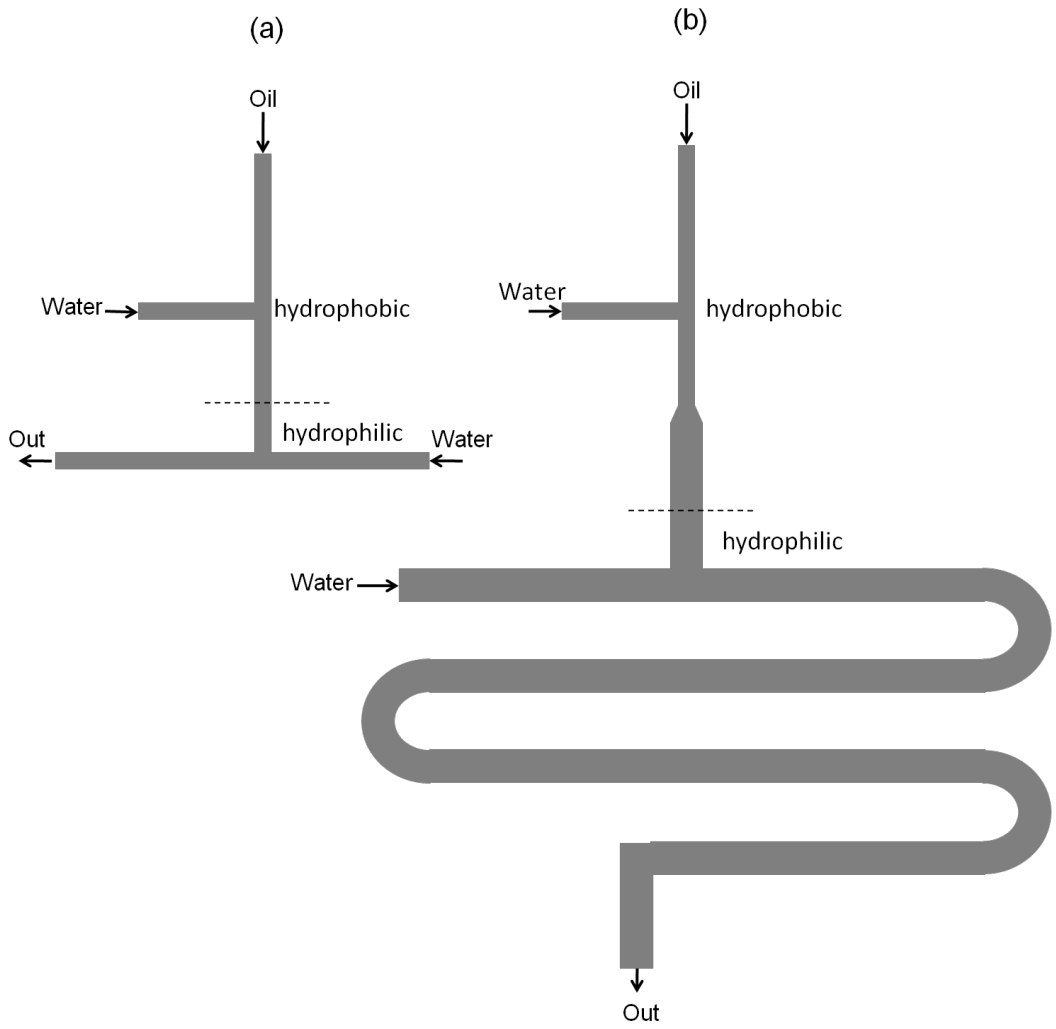

Fig 6.16. Schematic of double emulsion microchips (single chip module).

from the oil inlet and was monitored through the microscope as it started to fill the channel. Glycerol was added to the honey in order to avoid its solidification in the microchannel. When the channel was filled to the point just above the second T-junction indicated by the dotted line, the flow was stopped. As honey is a highly viscous liquid there is almost no chance that it will flow past the junction. After blocking the hydrophobic part of the microchip, plasma polymerization of acrylic acid was carried out. Plasma was generated using an

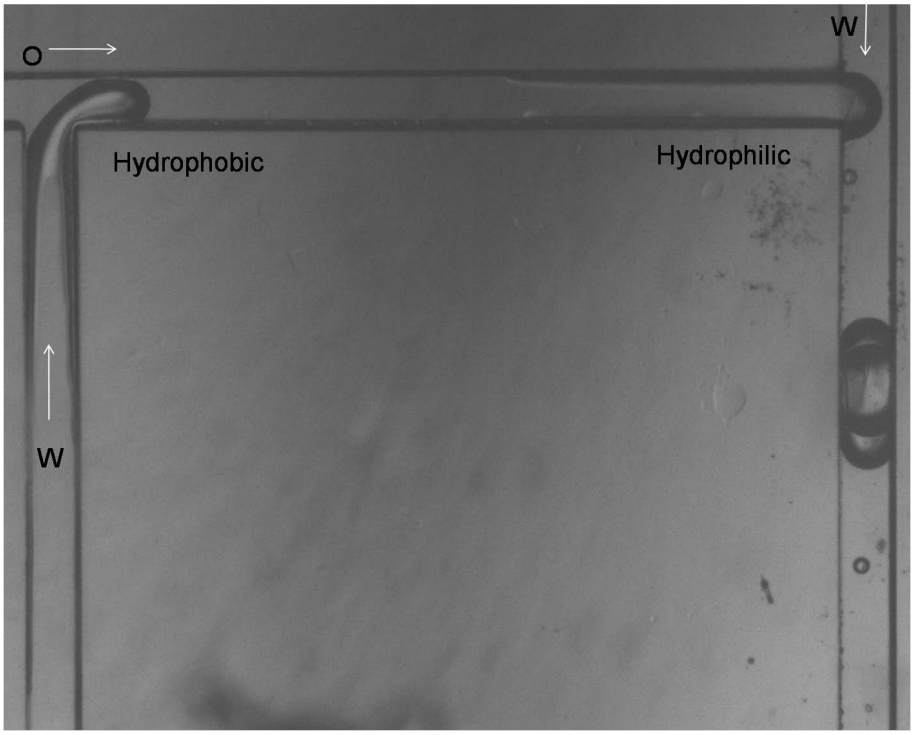

Fig 6.17. Water-in-oil-in-water emulsion in a double T-junction comprising channels of equal dimensions.

original aforementioned microjet technique via an external water phase inlet. As the discharge power is low, the temperature of the blocked channel will not increase thus avoiding any lowering of the viscosity of the honey. However, if the viscosity of the honey is too high, then plasma reactive species will be inhibited from accessing those regimes of the microchannel surface that are blocked by the honey and therefore those regions will remain hydrophobic. The regions of the channel surfaces that are exposed to the plasma will become hydrophilic. The hydrophilic microchannel is the second channel in series which is preferentially wetted by water over oil as shown in Fig. 6.16. This hydrophilic modification results in emulsification of oil droplets in water at the second T-junction of the microchip. Once the oil droplet formation in water was ensured, formation of a double emulsion was achieved by use of both the hydrophobic and hydrophilic

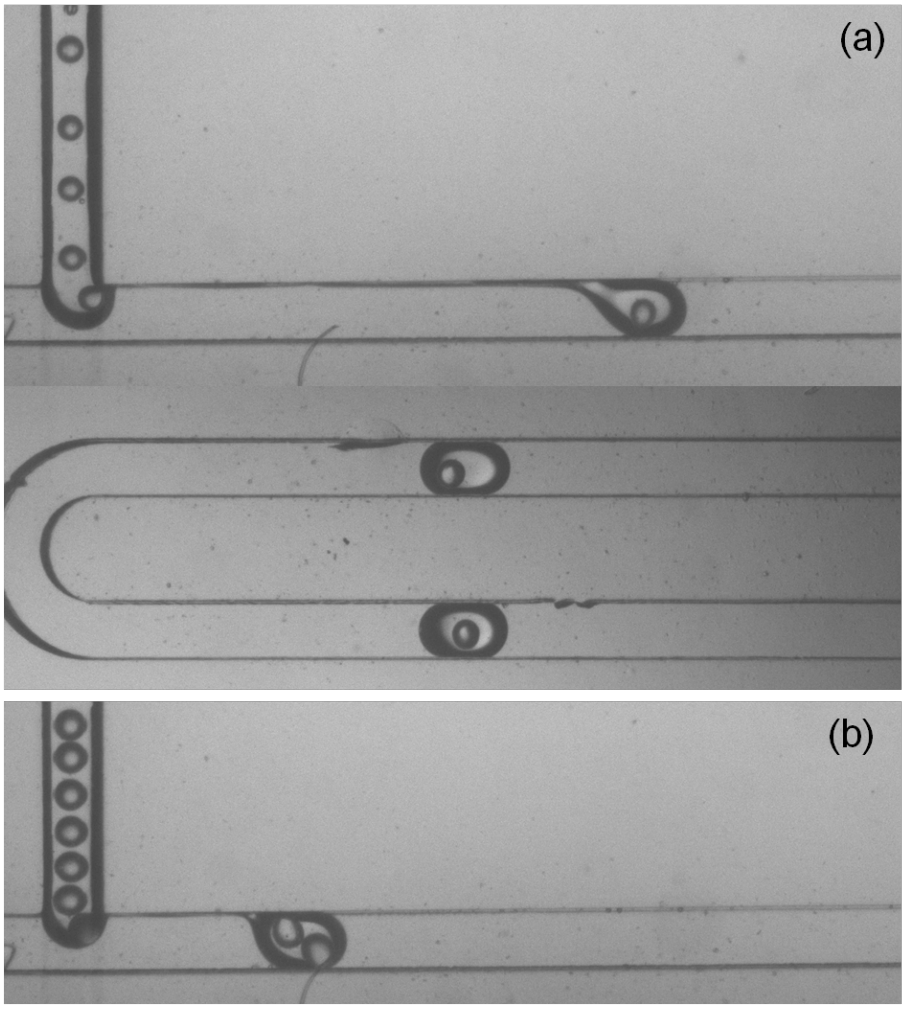

Fig 6.18. Water-in-oil-in-water emulsion in double T-junction with different dimensions. Water droplet encapsulation in an oil droplet/plug. (a) Q_{iw}:Q_{mo}:Q_{ew}=1:4:200 (b) Q_{iw}:Q_{mo}:Q_{ew}=1:2:200.

junctions of the same microfluidic chip.

Two types of configuration were employed in order to perform the double emulsion experiments as shown in Fig. 6.16. In the first geometry considered, both the upper and lower parts of the microchannel were of the same dimensions (100 μm wide). A single internal water droplet encapsulation occurs in an intermediate oil plug as shown in Fig. 6.17. However, in second type of geometry where

the hydrophilic section of the microchip is wider (200 μm) than the hydrophobic section (100 μm), the number of internal water droplets can be altered by varying the flow rate ratio $Q_i = \frac{Q_{iw}}{Q_{mo}}$ whilst keeping the external water phase flow rate, Q_{ew}, fixed as shown in Fig. 6.18.

6.9 Conclusions

A single step inline microchannel surface modification method based on plasma polymerization of acrylic acid was presented for stable production of onchip double emulsions. Highly monodispersed oil-in-water and water-in-oil-in-water emulsions in hydrophilically modified PDMS microdevices were successfully prepared. Droplets of different types of oil were used to form single oil-in-water emulsions and the results were compared in order to see the effect of viscosity on droplet size. The oil droplet size decreases using an oil with a relatively high viscosity over the entire range of water flow rates considered. Water-in-oil-in-water double emulsions were prepared using the two chip module and the single chip module. In the two chip module double emulsions were flexibly generated. In W/O/W emulsions, the intermediate oil droplet size was controlled by varying the external flow rate conditions and the size of droplet enclosed in an intermediate oil droplet was altered by changing the flow rate ratio at the hydrophobic junction. The plasma based surface modification method was proved to be robust, and avoids the use of surfactants in the continuous phase. Furthermore, a section of a single microchip was modified to hydrophilic using a novel viscous liquid blocking technique for the generation of W/O/W emulsions.

7

Flow fields during formation of W/O and O/W emulsions using μPIV

The current work investigates two phase flow visualization in a microchannel using micron resolution particle image velocimetry (μPIV). Droplets of both oil-in-water and water-in-oil were generated in a T-junction PDMS microfluidic device and the corresponding flow fields were measured downstream in the divergent section of the device. To obtain the velocity fields in both types of emulsions, fluorescent particles of 0.86 μm size were added into the dispersed water phase in case of water-in-oil emulsions, and in the continuous water phase in case of oil-in-water emulsions.

7.1 Introduction

Micron resolution image velocimetry (μPIV) is a well known flow visualization and velocity measurement technique. It can be used to measure the instantaneous velocity fields in a microchannel. The basic principle of μPIV is same as that of conventional PIV but instead the whole volume of the microchannel is illuminated. It involves an intrusion of nano- to micron-sized seeding particles into the flow field. These are illuminated using a double pulsed laser. As a result, two consecutive images separated by a short time interval are recorded. These two images are then correlated to determine the displacement of particles over the time interval (separation between two images) and hence the velocity field is determined. μPIV requires an optical access to the microfluidic device and therefore the device needs to be transparent for flow visualization.

The first successful application of μPIV was made by Santiago et al. (1998) to analyze local flow fields in a microchannel. Since then, this technique has been used by a large number of researchers to characterize flow in microfluidic devices (Devasenathipathy et al., 2003; Sinton, 2004; Brown et al., 2006; Linken et al., 2006; Bandulasena et al., 2008, 2009). μPIV can be used to characterize two phase flows in a microchannel. This is particularly useful for liquid phase dispersion which is needed in the design of microreactors with enhanced performance. Generally, velocity profiles can be determined in each of the phases with the addition of appropriate seeding particles (Steijn et al., 2007; Malsch et al., 2010; Timgren et al., 2008; Wang et al., 2007).

In this chapter the flow field around an oil droplet, and inside water droplets, in a PDMS microchannel have been presented. These flow fields were analysed

at a time when the droplets had migrated far away from the T-junction and had relaxed downstream into the divergent channel. The microfluidic channel details are described in chapter 5. In the diverging channel fluid velocities are reduced compared to those of the initial inflow. The flow behaviour differs from that in the vicinity of the T-junction. This phenomenon has not previously been well-explored, and hence it forms the major topic of this chapter.

7.2 System description and principle of μPIV

As shown schematically in Fig. 7.1, our micron resolution particle image velocimetry equipment consists of a Nd:YAG double pulsed laser with a wavelength of 532 nm. The laser is aligned with an inverted microscope (Zeiss Axiovert S100). A 12 bit CCD camera (PCO Sensicam) is mounted on the microscope for imaging with a window comprising 1280 $\times$ 1024 pixels. A synchronizer controls both the laser and the camera. A long pass filter with a cut off of 560 nm is used to block the laser light. A personal computer with VidPIV software installed is used to record the data and to perform the post processing of the images.

Droplet formation experiments were performed in a PDMS microfludic device consisting of a T-shaped droplet generator of 100 $\times$ 50 μm^2 cross section, intersecting channels and a wider diverging section of 200 $\times$ 50 μm^2 rectangular cross section where droplets are subsequently relaxed. Fluorescent particles of diameter 0.86 microns (Dukes Scientific Co.) were used as seeding particles into the DI water flow, which acted as a droplet phase in case of water-in-oil emulsions and as a continuous phase in case of oil-in-water emulsions. Fluorescent particles were added into the DI water in a proportion of 30 μl per 2ml solution

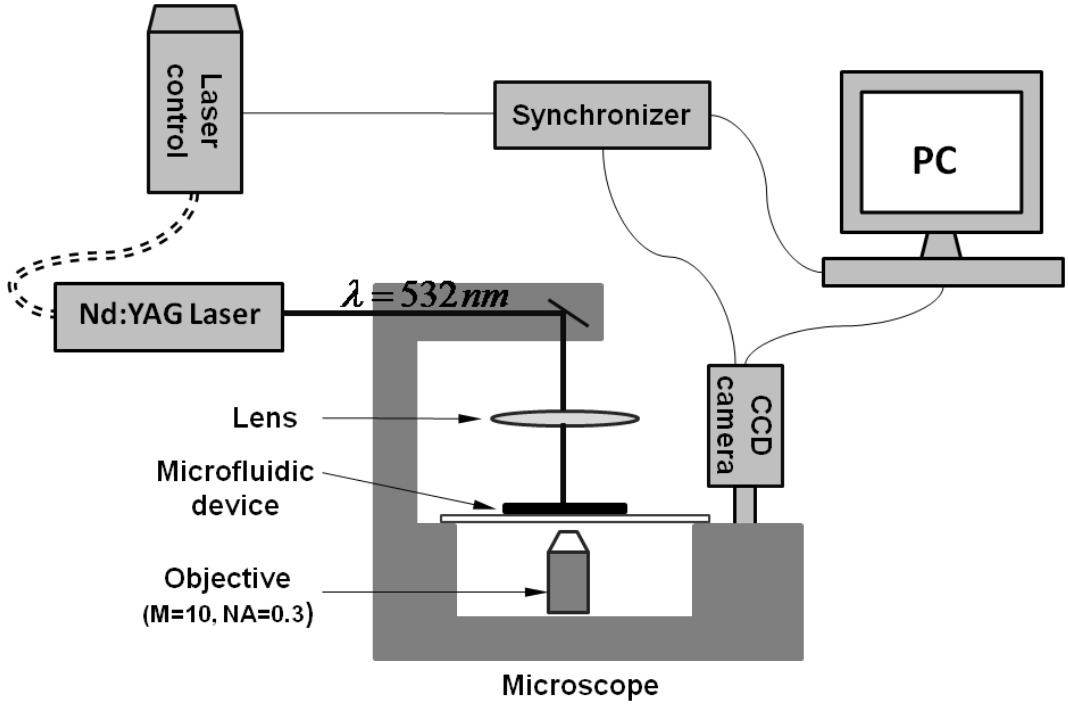

Fig 7.1. Schematic of experimental setup for microPIV

(0.015 % v/v). The particles were mixed into the DI water using an ultrasonic treatment for a period of 30 min duration. The laser beam illuminates a region of flow within the microchip. Fluorescent tracer particles are excited by the 532 nm wavelength laser and emit light at a wavelength of around 585 nm. A long pass filter cube adjusted below the magnification lens blocks the laser light but allows the passage of light emitted by the particles. The resulting images were acquired using a high resolution CCD camera. Pulse distance, which is the time separation between the two images was set according to the averaged flow rate of the two phase fluid flow rates in such as way that the maximum particle displacement is around 25% of the size of the interrogation window (32 $\times$ 32 pixels). VidPIV software computes how far the particles have moved between the pairs of images using a standard cross correlation technique and finally a map of the velocity field is generated.

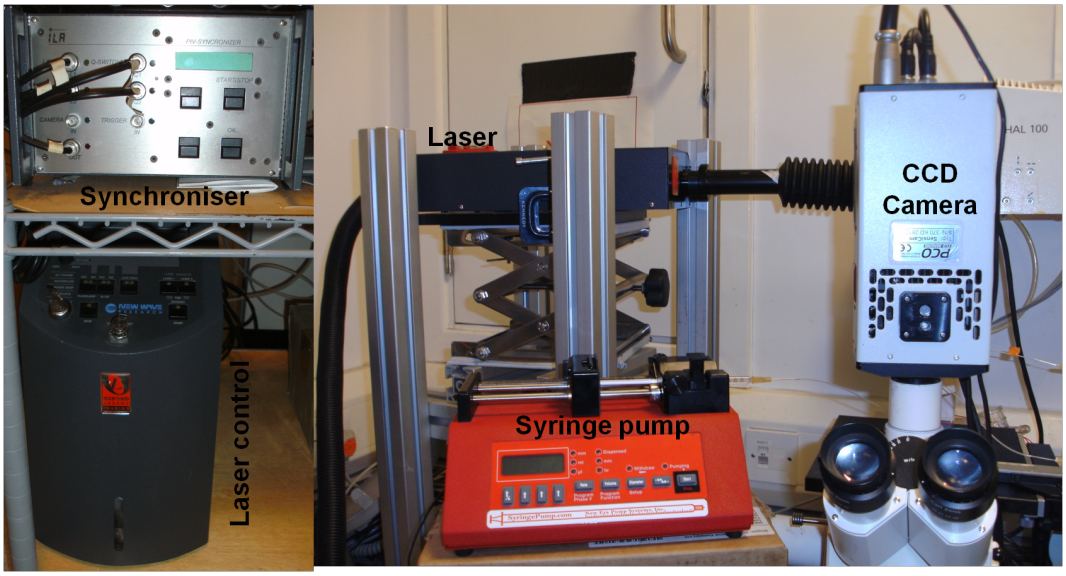

Fig 7.2. Experimental setup for microPIV

7.3 Results and discussion

7.3.1 μPIV measurement

Droplets are generated at a T-junction intersection and are subsequently relaxed in a divergent section of the microfluidic device. The divergent section of the microchip is focussed via volume illumination for PIV imaging. Flow visualization was achieved by capturing a 10-fold magnified image by the CCD camera. Therefore, the system needs to be calibrated with the actual length scale in order to determine the original distance between the particles. For this purpose, graticules with graduation marks of 0.01 mm and 0.05 mm were captured with a 10$\times$ objective lens as shown in Fig. 7.3. The horizontal distance with a number of pixels in a row was compared with the actual dimensions and as a result we obtained the relationship that 1 pixel=0.6667 microns. The optical parameters associated with the μPIV measurements are given below in

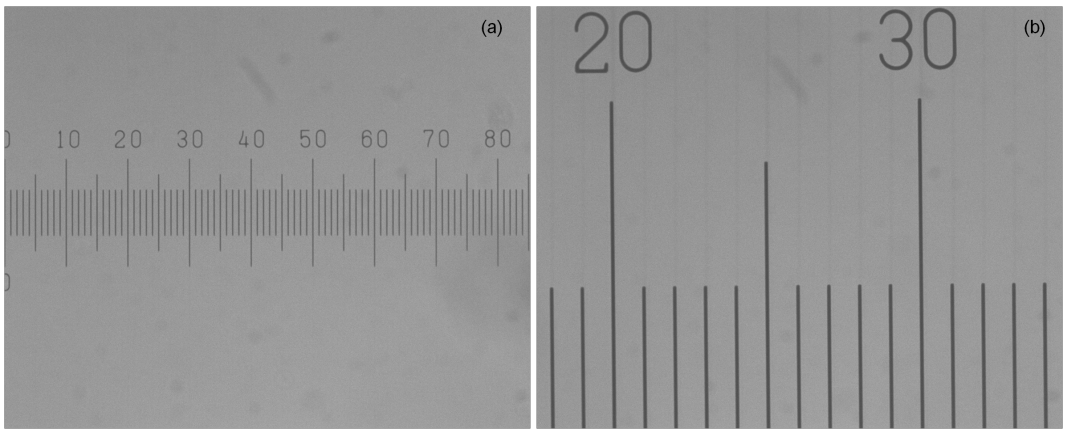

Fig 7.3. Graticule image with (a) 0.01mm graduation marks and (b) 0.05 graduation marks taken by CCD camera on 10X magnification.

Table 7.1. Parameters for μPIV setup.

n (water) Refractive index	M Magnification	NA Numerical aperture	d_p Particle diameter	ρ_p Particle density	λ_l Wavelength
1.33	10	0.3	0.86 μm	1005 kg/m^3	585 nm

Table. 7.1. Hence, the field of view is 853.38 μm$\times$682.70 μm for the objective lens used (Table. 7.1). The in-plane spatial resolution of 21.3 μm$\times$21.3 μm was obtained using an interrogation window size of 32$\times$32 pixels. A high signal to noise ratio (SNR) is usually obtained by either reducing the depth of the channel or the particle concentration (Meinhart et al., 2000). Due to the predefined dimensions of the microchannel geometries, the depth is fixed, therefore the particle concentration is the main parameter that can be optimized. The concentration of fluorescent particles in our experiment was chosen by considering results from a series of experiments comprising different particle concentrations in order to obtain adequate quality PIV images.

The choice of seeding particles should be made such that they are small enough

to closely follow the flow and to avoid clogging of the microchannel. On the other hand they should be large enough to obtain a successful fluorescent image and to minimise the effect of Brownian motion. In contrast to fluid mechanics at macroscales, the hydrodynamic particle size is usually not of importance in microfluidics due to the large surface to volume ratios at small length scales. The particle behaviour can be determined by representing the response time of a particle as a step change in fluid velocity. Based on the assumption of Stokes flow, the response time of particles is given by:

$$\tau_p = \frac{d_p^2 \rho_p}{18\eta}, \tag{7.1}$$

where d_p is the particle diameter, ρ_p is the density of the particle and η is dynamic viscosity of the fluid. The response time of 0.86 micron diameter polystyrene particles in water, which were used in our flow visualization experiments, is of the order of 10^{-8}s which is much smaller than the time scales of any practical liquid or gas flow at low speed.

The random motion of seeding particles causes uncertainty in μPIV measurements which were quantified by Santiago et al. (1998). The relative error, ε_B, in the measured horizontal displacement of a particle immersed in a fluid moving with velocity u, over a time interval Δt is estimated as

$$\varepsilon_B = \frac{1}{u}\sqrt{\frac{2D}{\Delta t}}, \tag{7.2}$$

where D is the Stokes-Einstein diffusion coefficient of a particle.

The spatial resolution of an optical system is limited by the diffraction (Inoue and Spring, 1997). The diameter of the diffraction limited point-spread function

is given by

$$d_s = 2.44M\frac{\lambda_l}{2NA}, \tag{7.3}$$

where M is the magnification, NA is the numerical aperture and λ_l is wavelength of the recording light (Nguyen and Wereley, 2006). The diameter of the diffraction limited point-spread function, d_s, was calculated from parameters listed in Table. 7.1 as 23.79 μm.

The effective diameter of a particle image, d_e, recorded on the CCD array is a convolution of the diffraction limited point-spread function and geometric image, and is estimated as (Adrian and Yao, 1985; Adrian, 1997):

$$d_e = \sqrt{M^2 d_p^2 + d_s^2}. \tag{7.4}$$

This diameter is calculated to be 25.3 μm for our system. When the image on the CCD array is projected back into the flow field, the effective diameter is estimated to be 2.53 μm. The diameter of the particle image needs to be resolved by more than 3-4 pixels in order to determine the location of the image correlation peak to within one tenth of the particle image diameter (Prasad et al., 1992). This results in a measurement uncertainty of $\delta x = d_e/10M = 253$ nm.

According to Meinhart et al. (2000), the measurement depth is more relevant than the depth of field in μPIV. The measurement depth of two dimensional μPIV is twice the distance from the objective plane in which a particle is sufficiently unfocussed that its contribution to the velocity measurement becomes insignificant. Considering this, the cut-off particle image intensity is set to be 10% of the maximum intensity of the focused particles. This gives an estimate

for the total measurement depth, δz_m, as

$$\delta z_m = \frac{3n\lambda_l}{(NA)^2} + \frac{2.16d_p}{\tan\theta_l} + d_p, \tag{7.5}$$

where θ_l is the light collection angle of the objective (Meinhart et al., 2000) and n is the refractive index of water. For the current experimental setup, this value is estimated to be 25.94 μm.

7.3.2 Flow profiles in the continuous aqueous phase during the formation of oil-in-water emulsions

A PDMS microchannel was modified from hydrophobic to hydrophilic in order to form an oil-in-water emulsion. Mineral oil was used as the dispersed phase and DI water was used as the continuous phase. This section analyses the flow field around an already formed oil droplet as it flows in a divergent section of the T-junction microfluidic device (see chapter 5). The oil droplet formation in DI water containing fluorescent particles with $10\times$ magnification is shown in Fig. 7.4. The base and cross PIV images are shown in Fig. 7.5. The velocity vectors shown in Fig. 7.6 were obtained using the adaptive cross correlation technique. The flow profiles show that when the droplet relaxes in the divergent channel section, the continuous phase sweeps through the small gap between the oil droplet and channel walls at a higher speed due to the high shear rate existing between the continuous water phase and the droplet. Fig. 7.7 presents the velocity profile of the continuous water phase along the line perpendicular to the flow direction across the rear and front sides of the droplet interface, and in the middle of the droplet. The velocity is shown to be zero in the middle of oil

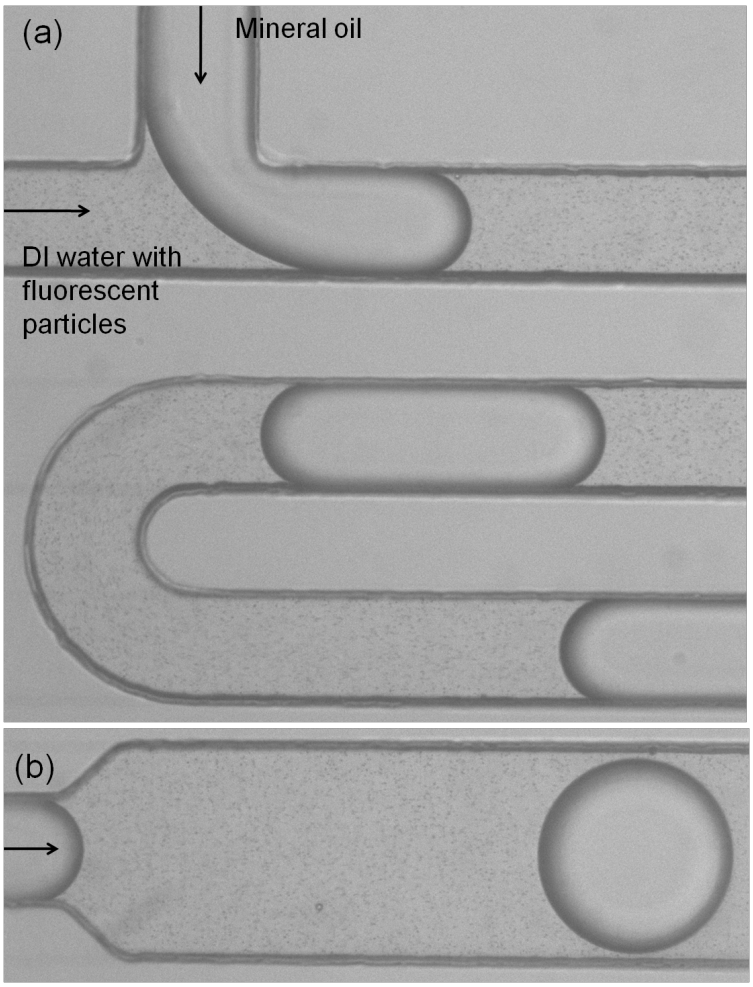

Fig 7.4. Fluorescent particles illuminated by halogen light in a continuous water phase with Q_o=1 μl/min and Q_w=4 μl/min, (a) droplet formation of mineral oil at T-junction (b) droplets of oil moving into the divergent section.

droplet unless any particle diffusion occurs through the interface. However, fluid will flow through the gap between the oil droplet and the channel wall with a speed higher than that of droplet upstream (rear) and downstream (front) side. A gradual deceleration in the velocity profile occurs across the rear and front side of the oil droplet towards the middle of the channel due to the presence of high resistance to the flow at the interface. The magnitude of the velocity vectors in the divergent channel is shown in Fig. 7.8. The color bar indicates

the lowest to highest distribution of the velocity magnitude in the channel.

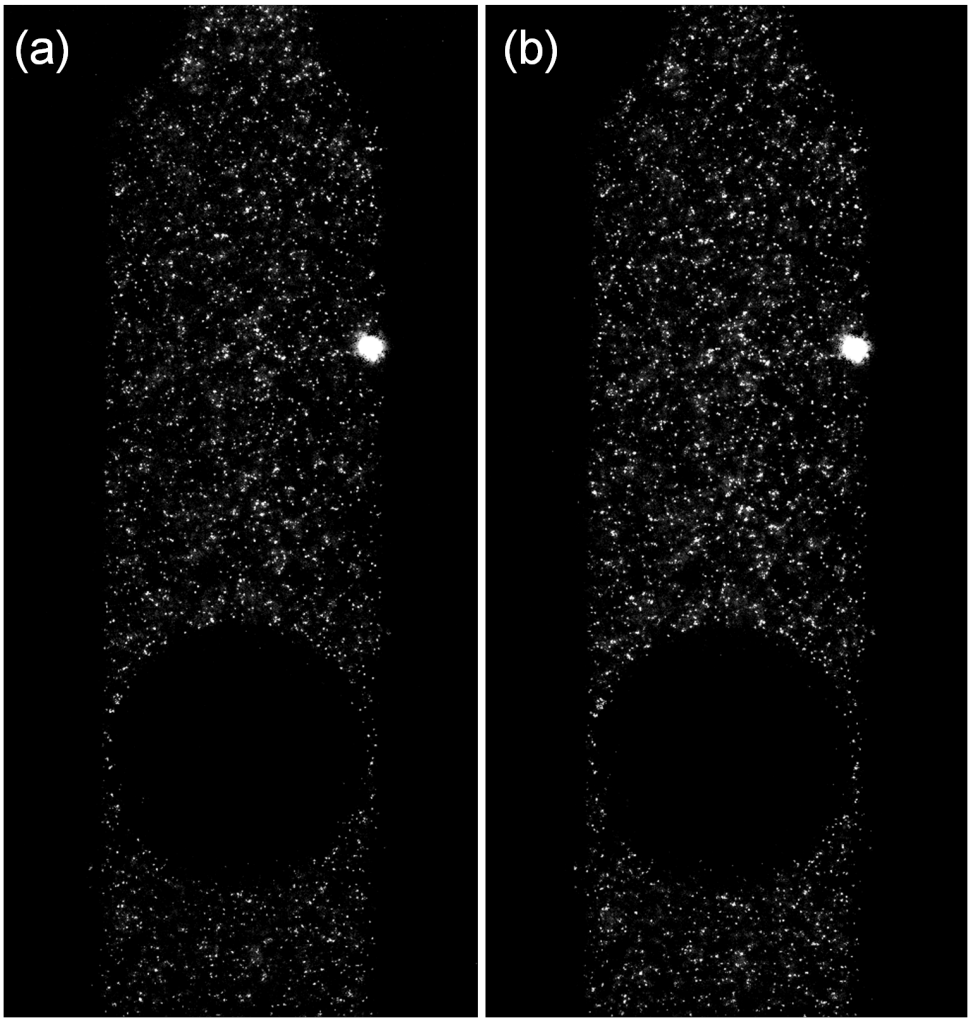

Fig 7.5. Fluorescent particles illuminated by the double pulsed laser in a continuous water phase that contains a previously formed oil droplet with Q_o=1 μl/min and Q_w=4 μl/min, (a) base image at time t, (b) cross image at $t + \triangle t$.

7.3.3 Flow profiles in an aqueous droplet phase during the formation of water-in-oil droplets

The internal flow field of a moving droplet confined in a diverging channel is presented in Fig. 7.9. As the flow is extremely slow, we did not observe standard

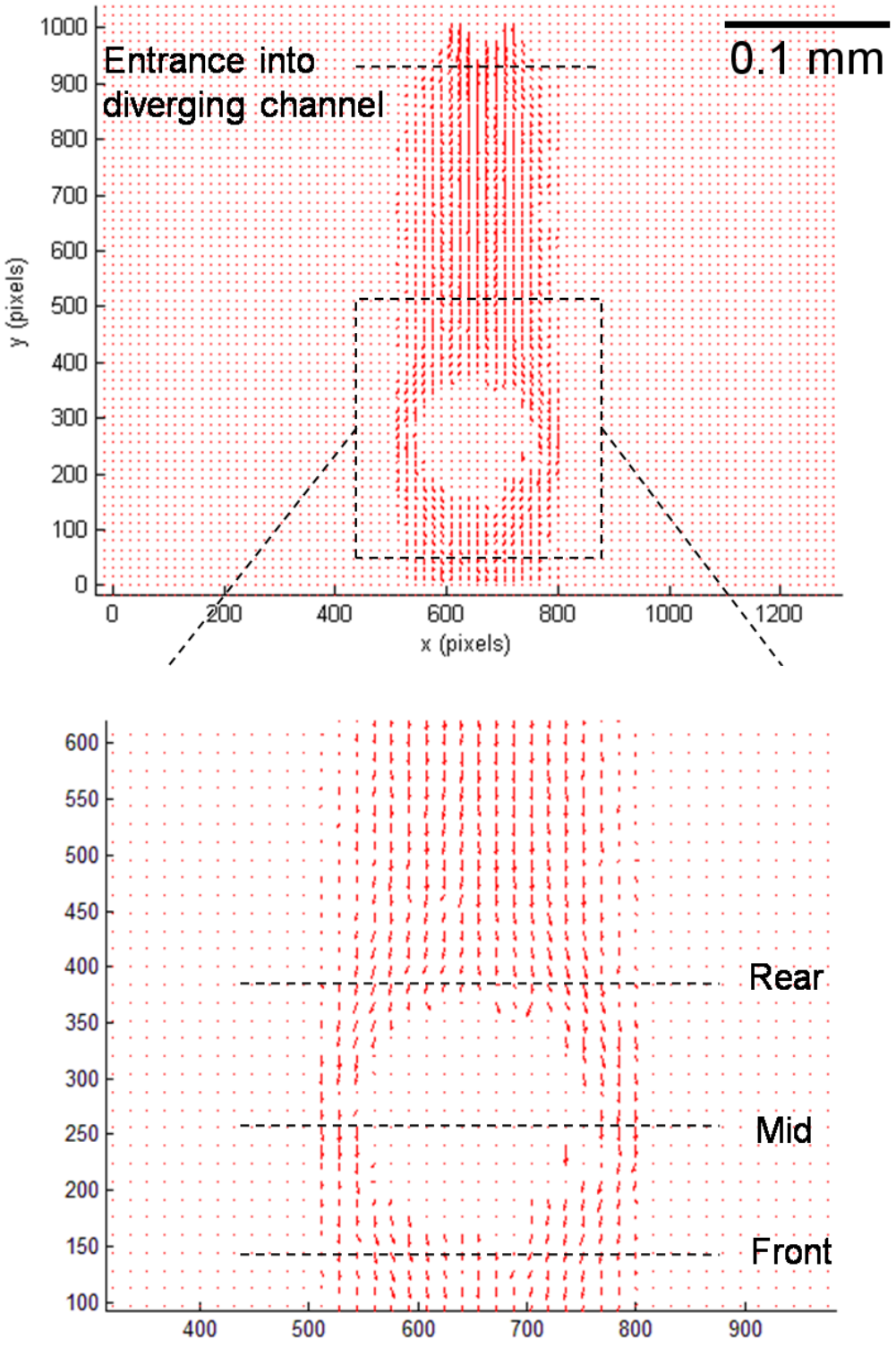

Fig 7.6. Velocity vectors in continuous water phase around an oil droplet, Q_o=1 μl/min, Q_w=4 μl/min.

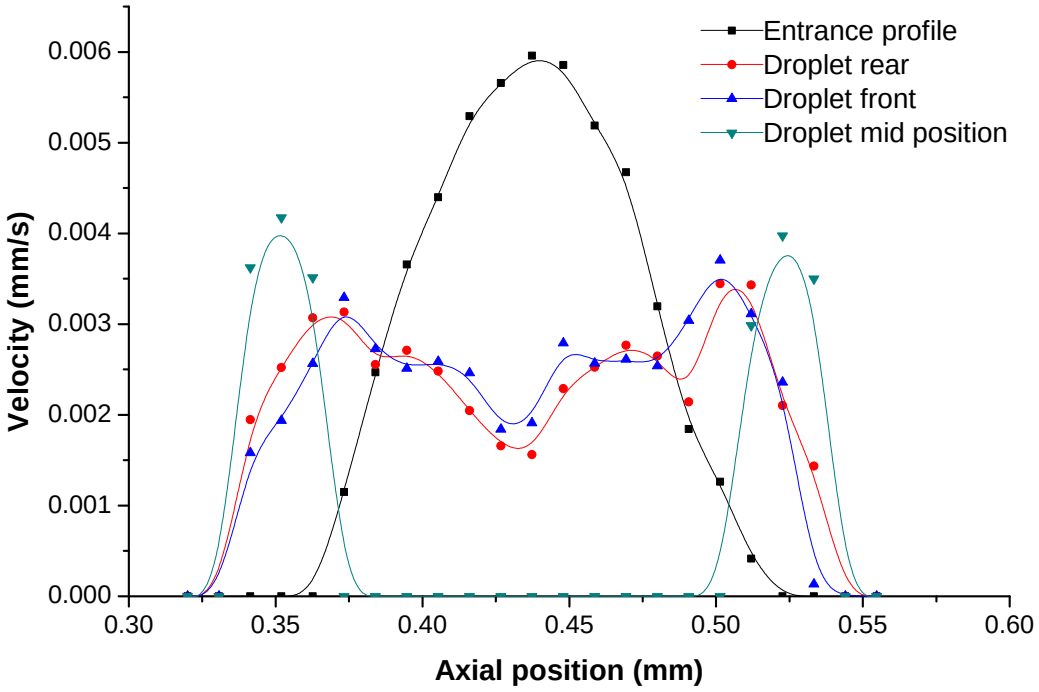

Fig 7.7. Velocity profiles in different sections of the continuous water phase around an oil droplet with Q_o=1 μl/min and Q_w=4 μl/min.

circulation within the droplet.

As the oil flow rate increases the droplet size decreases, but still remains confined in the divergent section. It becomes unconfined at higher flow rates, e.g. at oil flow rates of 4 μl/min and 8 μl/min as shown in Fig. 7.10, when the gap between the droplet and the wall increases. It was observed that the velocity at the streamwise interfaces for continuous phase flow rates of Q_o=0.5 μl/min, 1 μl/min and 2 μl/min is higher than those operating at flow rates of Q_o=4 μl/min and 8 μl/min (Fig. 7.11). This is because the shear stress effect at interfaces with the continuous phase flow is more pronounced in the case of confined droplets. The velocity profile is slightly parabolic in the case of the lowest flow rate considered (Q_o=0.5 μl/min), showing that in the center of

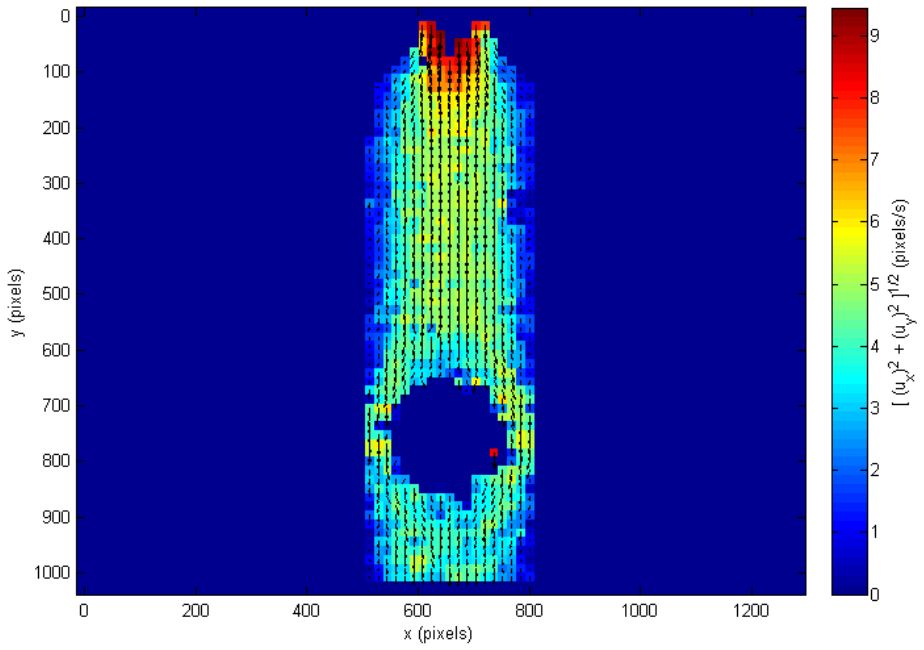

Fig 7.8. Velocity profiles in continuous water phase containing an already formed oil droplet, Q_o=1 μl/min, Q_w=4 μl/min.

the droplet the flow is weakly accelerated. This profile damps gradually at increasing continuous phase flow rates and eventually becomes reversed within the unconfined droplet at highest flow rate considered (8 μl/min), showing a strong deceleration in the center of droplet. However, the overall motion of the droplet follows the direction of flow downstream.

7.4 Conclusions

The flow profiles presented herein provide a fundamental understanding of the very slow flow rate of droplets within a divergent microchannel. The flow becomes very slow as the droplets move downstream in the divergent section of

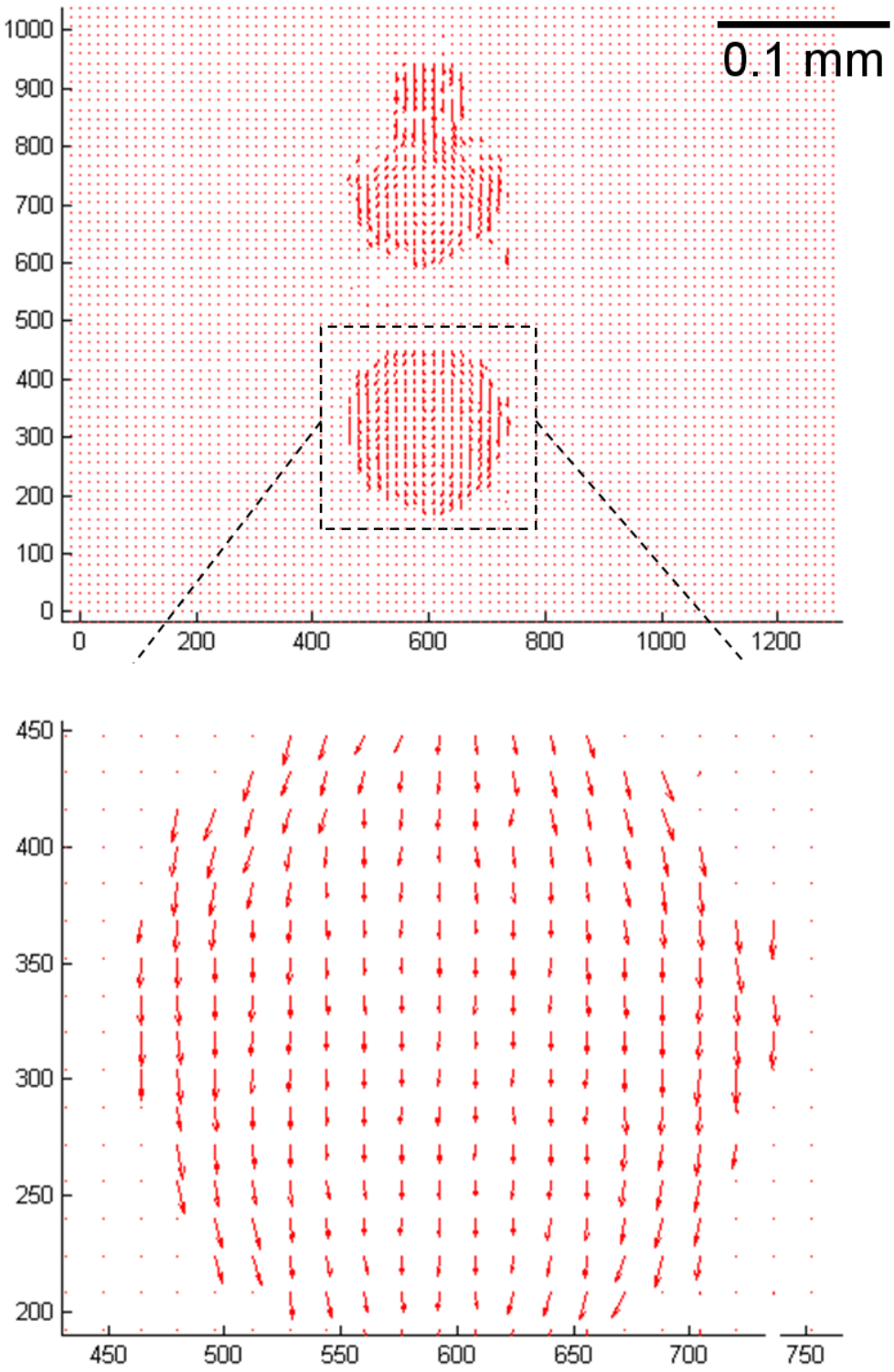

Fig 7.9. Velocity vectors in continuous water phase around an oil droplet, Q_o=1 μl/min, Q_w=1 μl/min.

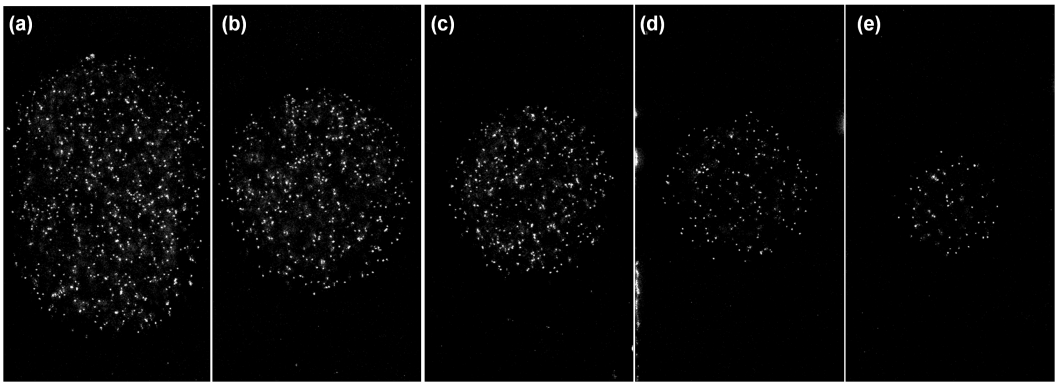

Fig 7.10. PIV images of fluorescent particles in water droplet moving in diverging section of microchannel at different oil flow rates of (a) Q_o=0.5 μl/min, (b) Q_o=1 μ l/min, (c) Q_o=2 μl/min, (d) Q_o=4 μl/min, (e) Q_o=8 μl/min.

the microchannel. This results in the velocity profiles across water droplets dispersed in a carrier oil indicating that no regions of circulation are present. Furthermore, flow profiles in the center of water droplet for different flow rates were compared and it was found that the degree of confinement of the droplet in the divergent microchannel altered the velocity profiles in droplets. The flow was observed to decelerate through the thicker films of carrier fluid that existed between the droplet and the microchannel walls. In the case of the formation of an oil-in-water emulsion, velocity profiles in the continuous water indicated that the maximum velocity occurred around the interface adjacent to the channel wall. This arose due to the strong shear existing between the droplet and the channel wall. A high degree of deceleration in the flow around the center of the rear interface of the oil droplet was observed which is due to the high level of resistance to the flow, and around the center of the front interface due to the resistance to the outflow. As these observations of flow behaviour are according to expectation, we conclude that the data can be useful for validating computational fluid dynamic models as part of a future work programme.

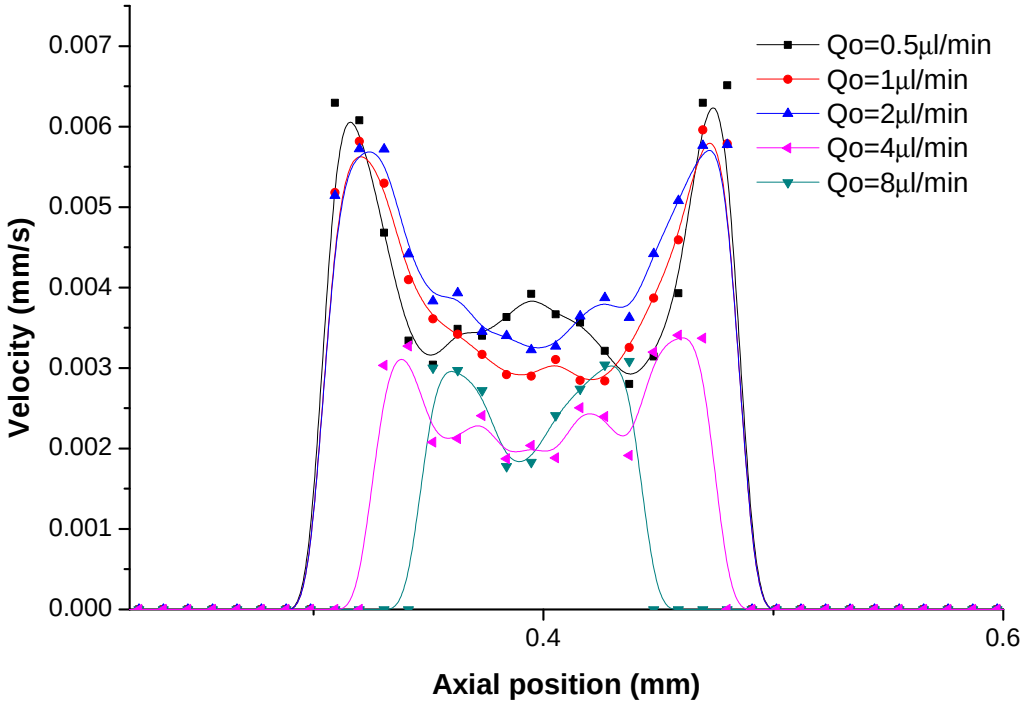

Fig 7.11. Velocity profiles across water droplets dispersed in a continuous oil phase for range of flow rates Q_o=0.5 μl/min, 1 μl/min, 2 μl/min, 4 μl/min and 8 μl/min with a constant dispersed water phase flow rate of Q_w=1 μl/min. The profiles are shown in mid position of the droplet perpendicular to the flow direction.

8

Summary and outlook

This study was motivated by the numerous existing and potential uses of droplet based microfluidic systems in a wide variety of applications. The objective of this thesis was to gain a comprehensive understanding of the principles and dynamics of droplet formation in microfluidic T-junction devices. T-junction devices were chosen due to their simplicity in terms of design, operation and fabrication. The first part of the study was based on the understanding of the physical parameters affecting the droplet formation process in the microfluidic device which is necessary in order to achieve the precise control over the production of microdroplets. Numerical simulations based on the two phase level set method were performed to predict the effect of different control parameters, including the contact angle of the droplet with the microchannel walls. The wetting property was found to have an important role in determining the droplet size and formation time. The influence of contact angle on droplet size was found to be significant for $Ca < 0.02$ (squeezing regime) but became negligible for $Ca \geq 0.02$. For a specific contact angle, the droplet size was predicted to in-

crease logarithmically with the interfacial tension between two fluids. Moreover, in a strictly confined T-shaped microchannel, the four phases of the droplet formation process (intrusion, blocking, squeezing and breakup) were distinguished through the evolution of the pressure profile upstream of the T-junction near the rear interface of the forming droplet. The upstream pressure near the rear interface of the droplet was found to gradually decrease as the contact angle was increased. Consequently the time taken by the emerging droplet to block the channel downstream decreased and thus the droplet formation time was reduced.

Surfactants are important ingredients in the preparation of emulsions as they stabilize emulsions against coalescence. They can promote de-wetting of liquids on solid surfaces. These miraculous properties of surfactants motivated the experimental study that comprised preparation of water-in-oil emulsions containing an oil soluble surfactant in a PDMS microfluidic device. Mineral oil was used as a carrier oil phase containing Span 80 surfactant. Macroscale measurements of interfacial tensions between water-oil+Span 80 interface and static contact angles of water on the PDMS surface immersed in an oil+Span 80 with a range of Span 80 concentrations were carried out. The data provided a basis for studying dynamic wetting in microdroplet experiments. The droplet lengths of water in the microchannel were measured for different concentrations of surfactant in oil. The droplet lengths were found to be independent of surfactant concentration beyond the CMC level of $\sim$1% w/w. This finding is of importance as it provides a route for estimating the CMC level for droplet formation experiments. Dynamic contact angles (advancing and receding) of water droplets with the channel wall were found to increase with increasing surfactant concentration in carrier oil, and to decrease with increasing flow rate ratios.

In the second part of the experimental programme, an innovative surface modification method based on an inline plasma polymerization technique was presented. The internal walls of PDMS microfluidic devices were modified to render them hydrophilic in order to exploit them for the generation of oil-in-water and water-in-oil-in-water double emulsions. The two chip module was applied successfully by connecting a hydrophobic and a modified hydrophilic PDMS device in series and proved to be a straightforward double emulsion system. Furthermore, a new channel blocking technique was also employed in order to partially modify the surface of a single microfluidic chip comprising of two T-junctions in series to make it capable of uniform production of double emulsions.

Finally, a micron resolution flow visualization technique (μPIV) was used to determine the velocity fields in both water-in-oil and oil-in-water droplets in the diverging section of a microfluidic T-junction device. The fundamental flow behaviour inside and around the moving droplets was captured. This technique can be used to quantitatively describe the complex flow behaviour inside microfluidic devices which may often be counterintuitive due to low Reynolds number hydrodynamics.

In conclusion, the numerical modelling provided insight for understanding the physical behaviour of the droplet formation processes. The experimental methods for altering the wettability of PDMS microfluidic devices proved to be robust for the production of both types of single emulsions and double emulsions. In spite of the achievements presented, still some challenges for future studies remain:

Due to the explicit representation of sharp interfaces in the level set method it has the capability to describe the complicated physics involved in the droplet formation process. This could be enhanced further by improving the mesh

quality in order to reduce further the error in mass loss. The method has great potential for modelling droplet splitting, merging and sorting. Despite the fact that the numerical simulations capture the small scale features, it is always good practice where possible to compare the results obtained from simulations with observation from experiments for validation. μPIV has proved to capture these features experimentally and provides data for validating the numerical model. However, its practical implementation is cumbersome. Although, we have shown an improved performance of hydrophilically modified PDMS surfaces, further work is still required due to its potential in several microfluidic applications. The application of the plasma coating method could be further generalized by parallelizing it for the modification of several microfluidic channels simultaneously. The selective modification of microfluidic devices for the production of double emulsions could be achieved using our plasma modification method more flexibly if the path length between the two junctions is increased. As the double emulsions formed in this work are highly uniform, stable and monodispersed their utilization for important applications such as cell encapsulation and drug delivery could be guaranteed.

Bibliography

Adrian. R.J., Yao. C.S., 1985. Pulsed laser technique application to liquid and gaseous flows and the scattering power of seed materials, Applied Optics, 24, 44-52.

Adrian. R.J., 1997. Dynamic ranges of velocity and spatial resolution of particle image velocimetry, Meas. Sci. Technol. 8, 1393-1398.

Anna, S. L., Bontoux, N., Stone, H. A., 2003. Formation of dispersions using 'flow focusing' in microchannels. Appl. Phys. Lett. 82(3), 364-366.

Armani, D., Liu, C., Aluru, N., 1999. Re-configurable fluid circuits by PDMS elastomer micromachining, MEMS'99: 12th IEEE International conference on Micro Electro Mechanical Systems, USA. 222-227.

Bandulasena, H.C.H., Zimmerman, W.B. and Rees, J.M., 2008. An inverse methodology for the rheology of a power law non-Newtonian fluid. Journal of Mechanical Engineering Science, Part C, 222(5), 761-768.

Bandalusena, H.C.H., Zimmerman, W.B, Rees, J.M., 2009. Microfluidic rheometry of a polymer solution by micron resolution particle image velocimetry: A model validation study, Meas. Sci. Technol. 20(11), 115404 (9pp).

Bashforth, S., Addams, J.C., 1882. An attempt to test the theory of capillary action, Cambridge University Press and Deighton, Bell and Co, London.

Barbier, V., Tatoulian, M., Tori, T., Arefi-Khonsari, F., Ajdari, A., Tabeling, P.,2006. Stable modification of PDMS surface properties by plasma polymerization: Application to the formation of double Emulsions in microfluidic systems. Langmuir. 22, 5230-5232.

Bashir, S., Rees, J. M., Zimmerman, W. B., 2011. Simulations of microfluidic droplet formation using the two-phase level set method. Chem. Eng. Sci. 66, 4733-4741.

Bauer, W.A.C., Fischlechner, M., Abellb, C., Huck, W.T.S., 2010. Hydrophilic PDMS microchannels for high-throughput formation of oil-in-water microdroplets and water-in-oil-in-water double emulsions, Lab Chip, 10, 1814-1819.

Berthier, J., Silberzan, P., 2006. Microfluidics for biotechnology, ARTECH HOUSE, INC., Norwood, Vol. 1.

Bodas, D., Khan-Malek, C., 2007. Hydrophilization and hydrophobic recovery of PDMS by oxygen plasma and chemical treatmentAn SEM investigation Sens. Actuator B Chem. 123, 368373.

Breslauer, D. N., Lee, P. J., Lee, L. P., 2006. Microfluidics-based systems biology, Mol. Biosyst. 2, 97-112.

Bringer, M. R., Gerdts, C. J., Song, H., Tice, J. D., Ismagilov, R. F., 2004. Microfluidic systems for chemical kinetics that rely on chaotic mixing in droplet. Phil. Trans. R. Soc. Lond. A. 362, 1087-1104.

Bown, M.R., MacInnes, J.M., Allen, R.W.K., Zimmerman, W.B.J., 2006. Department of three-dimensional, three-component velocity measurements using stereoscopic micro-PIV and PTV, Meas. Sci. Technol. 17, 2175-2185.

Chen, G., Chen, S., Chen, W., Yang, S., 2008. Biofilm deposited by the atmospheric plasma liquid sputtering. Surf. Coat. Technol. 202, 4741-4745.

Christopher, G. F., Noharuddin, N. N., Taylor, J. A., Anna, S. L., 2008. Experimental observations of the squeezing-to-dripping transition in T-shaped microfluidic junctions. Phys. Rev. E Stat. Nonlin. Soft Matter Phys. 78, 036317.

Davies, J., 1957. A quantitative kinetic theory of emulsion type. I. Physical chemistry of the emulsifying agent, Proceedings of the International Congress of Surface Activity, 426-438.

Davidson, M. R., Harvie, D. J. E., Cooper-White, J. J., 2005. Flow focussing in microchannels. ANZIAM J. 46(E), C47-C58.

Deshpande, K. B., Zimmerman, W. B., 2006. Simulation of interfacial mass transfer by droplet dynamics using the level set method. Chem. Eng. Sci. 86(18), 4163-4166.

Devasenathipathy, S., Santiago, J.G., Wereley, S.T., Meinhart, C.D., Takehara K., 2003. Particle imaging techniques for microfabricated fluidic systems, Experiments in Fluids, 34, 504-514.

De Menech, M., 2006. Modeling of droplet breakup in a microfluidic T-shaped junction with a phase-field model. Phys. Rev. E 73, 031505.

De Menech, M., Garstecki, P., Jousse, F., Stone, H. A., 2008. Transition from

squeezing to dripping in a microfluidic T-shaped junction. J. Fluid Mech. 595, 141-161.

Dorrer, C., Ruhe, J., 2006. Advancing and receding motion of droplets on ultrahydrophobic post surfaces, Langmuir 22(18), 7652-7657.

Duffy, D.C., McDonald, J.C., Schueller, O.J.A., Whitesides, G.M., 1998. Rapid prototyping of microfluidic systems in poly(dimethylsiloxane), Anal. Chem. 70, 4974-4984.

Dussan, E.B., 1979. On the spreading of liquids on solid surfaces: static and dynamic contact angles. Ann. Rev. Fluid Mech. 11, 371-400.

De Gennes, P.G., Wetting: statics and dynamics, 1985. Reviews of Modern Physics, 57(3), 827-863.

De Luca, M., Rocha-Filho, P., Grossiord, J.L., Rabaron, A., Vaution, C., Seiller, M., 1991. The multiple emulsions, International Journal of Cosmetic Science 13, 1-21.

Dreyfus, R., Tabeling, P., Willaime, H., 2003. Ordered and disordered patterns in two-phase flows in microchannels. Phys. Rev. Lett. 90(14), 144505.

Extrand, C.W., 2002. Model for contact angles and hysteresis on rough and ultraphobic surfaces. Langmuir, 18, 7991-7999.

Figeys, D., Pinto, D., 2000. Lab-on-a-Chip: A revolution in biological and medical sciences. Analytical Chemistry, 330A-335A.

Garstecki, P., Stone, H. A., Whitesides, G. M., 2005. Mechanisms for flow-rate controlled breakup in confined geometries: a route to monodisperse emulsions. Phys. Rev. Lett. 94, 164501.

Garstecki, P., Fuerstman, M. J., Stone, H. A., Whitesides, G. M., 2006. Formation of droplets and bubbles in a microfluidic T-junction scaling and mechanism of break-up, Lab. Chip 6, 437-446.

Griffin, W.C., 1949. Classification of surface-active agents by 'HLB', Journal of the Society of Cosmetic Chemists 1, 311.

Griffin, W.C., 1954. Calculation of HLB values of non-ionic surfactants, Journal of the Society of Cosmetic Chemists 5, 259.

Hansen, F.K., Rodsrun, G.J., 1991. Surface tension by pendant drop: I. A fast standard instrument using computer image analysis, J. Coll. Inter. Sci. 141(1), 1-9.

Haynes, L. G., Himmelblau, D. M., Schechter, R. S., 1968. Effect of plate wettability on droplet formation. Ind. Eng. Chem. Process Des. Dev. 7(4), 508-511.

Herlod, K.E., Rasooly, A., 2009. Fabrication and microfluidics, Vol. 1, p. 382. Caister Acadamic Press, Norfolk, U.K.

Hessel, V., Hardt, S., Lwe, H., 2004. Chemical micro process engineering, WILEY-VCH Verlag GmbH and Co. KGaA, Weinheim.

Hillborg, H., Ankner, J. F., Gedde, U. W., Smith, G. D., Yasuda, H. K., Wikstrom, K., 2000. Crosslinked polydimethylsiloxane exposed to oxygen plasma studied by neutron reflectometry and other surface specific techniques, Polymer 41, 68516863.

Husny, J., Cooper-White, J., 2006. The effect of elasticity on drop creation in T-shaped microchannels. J. Non-Newton. Fluid 137, 121-136.

Hu, S., Ren, X., Bachman, M., Sims, C.E., Li, G.P., Allbritton, N., 2002. Surface modification of poly(dimethylsiloxane) microfluidic devices by ultraviolet polymer grafting, Anal. Chem. 2002, 74, 4117-4123.

Inoue, S., and Spring, R.K., 1997. Video Microscopy: The Fundamentals, 2nd Ed., Plenum Press, New York.

Jullien, M. C., Ching, M. J. T. M., Cohen, C., Menetrier, L., Tabeling, P., 2009. Droplet breakup in microfluidic T-junctions at small capillary numbers. Phys. Fluids 21, 072001.

Kamusewitz, H., Possart, W., 2006. The static contact angle hysteresis and Young's equilibrium contact angle, in: Mittal, K. L. (Ed.) Contact Angle, Wettability and Adhesion, Volume 4, pp.101-104.

Kobayashi, I., Mukataka, S., Nakajima, M., 2005. Effects of type and physical properties of oil phase on oil-in-water emulsion droplet formation in straight-through microchannel emulsification, experimental and CFD studies. Langmuir 21, 5722-5730.

Link, D. R., Anna, S. L., Weitz, D.A., Stone, H. A., 2004. Geometrically mediated breakup of drops in microfluidic devices. Phy. Rev. Lett. 92(5), 054503.

Leng, J., Salmon, J.-B., 2009. Microfluidic crystallization. Lab. Chip 9, 24-34.

Leshansky, A. M., Pismen, L. M., 2009. Breakup of drops in a microfluidic T junction. Phys. Fluids 21, 023303.

Li, S., Xu, J., Wang, Y., Luo, G., 2008. Controllable preparation of nanoparticles by drops and plugs flow in a microchannel device. Langmuir 24(8), 4194-4199.

Li, D., 2008. Encyclopedia of microfluidics and nanofluidics, Springer, New York, USA.

Lindken, R., Westerweel, J., Wieneke, B., 2006. Stereoscopic micro particle image velocimetry, Experiments in Fluids 41, 161-171.

Massines, F., Gouda, G., 1998. A comparison of polypropylene-surface treatment by filamentary, homogeneous and glow discharges in helium at atmospheric pressure. 31, 3411-3420.

Malsch, D., Gleichmann, N., Kielpinski, M., Mayer, G., Henkel, T., Mueller, D., van Steijn, V., Kleijn, C.R., Kreutzer, M.T., 2010. Dynamics of droplet formation at T-shaped nozzles with elastic feed lines, Microfluid Nanofluid, 8, 497-507.

Matsumoto, S., Kita, Y., Yonezawa, D., 1976. An attempt at preparing water-in-oil-in-water multiple phase emulsions. J. Colloid Interface Sci. 57, 353-361.

McClements, J.D., 1999. Food emulsions: Principle, practices and techniques, CRC Press, Boca Raton, Florida, U.S.A.

McDonald, J.C., Duffy, D.C., Anderson, J.R., Chiu, D.T., Wu, H., Schueller, O.J.A., Whitesides, G.M., 2000. Fabrication of microfluidic systems in poly(dimethylsiloxane), Electrophoresis, 21, 27-40.

McDonald, J.C., Whitesides, G.M., 2002. Poly(dimethylsiloxane) as a material for fabricating microfluidic devices, Accounts of Chemical Research, 35(7), 491-499.

Meinhart, C.D., Wereley, S.T., Santiago, J.G., 1999. PIV measurements of a microchannel flow, Experiments in Fluids, 27. 414-419.

Meinhart, C.D., Wereley, S.T., Gray, M.H.B., 2000. Volume illumination for two-dimensional particle image velocimetry, Meas. Sci. Technol., 11, 809-814.

Ng, J.M.K., Gitlin, I., Stroock, A.D., Whitesides, G.M., 2002. Components for integrated poly(dimethylsiloxane) microfluidic systems, Electrophoresis 2002, 23, 3461-3473.

Nguyen, M.T., Wereley, S.T., 2006. Fundamentals and applications of microfluidics, ARTECH HOUSE, INC. Norwood, 2nd Edition.

Nisisako, T., Tori, T., Higuchi, T., 2002. Droplet formation in a microchannel network. Lab. Chip 2, 24-26.

Nisisako, T., 2008. Microstructured devices for preparing controlled multiple emulsions. Chem. Eng. Technol. 31(8), 1091-1098.

Nisisako, T., Tori, T., Higuchi, T., 2004. Novel microreactors for functional polymer beads. Chem. Eng. J. 101, 23-29.

Okushima, S., Nisisako, T., Tori, T., Higuchi, T., 2004. Controlled production of monodisperse double emulsions by two-step droplet breakup in microfluidic devices. Langmuir. 20, 9905-9908.

Olsson, E., Kreiss, G., 2005. A conservative level set method for two phase flow. J. Comput. Phys. 210, 225-246.

Osher, S., Sethian, J. A., 1988. Fronts propagating with curvature-dependent speed: Algorithms based on Hamilton-Jacobi formulations. J. Comput. Phys. 79, 12-49.

Papra, A., Bernard, A., Juncker, D., Larsen, N.B., Michel, B., Delamarche, E., 2001. Microfluidic networks made of poly(dimethylsiloxane), Si, and Au

coated with polyethylene glycol for patterning proteins onto surfaces, Langmuir, 17, 4090-4095.

Paria, S., Khilar, K. C., 2004. A review on experimental studies of surfactant adsorption at the hydrophilic solid-water interface. Adv. Colloid Interface Sci. 110(3), 75-95.

Peng, S. J., Williams, R. A., 1998. Controlled production of emulsions using a crossflow membrane. Part. Part. Syst. Charact. 15, 21-25.

Prasad, A.K., Adrian, R.J., Landreth, C.C., Offutt, P.W., 1992. Effects of resolution on the speed and accuracy of particle image velocimetry interrogation, Experiments in Fluids, 13, 105-116.

Qian, D., Lawal, A., 2006. Numerical study on gas and liquid slugs for Taylor flow in a T-junction microchannel. Chem. Eng. Sci. 61, 7609-7625.

Roman, G.T., Hlaus, T., Bass, K.J., Seelhammer, T.G., Culbertson, C.T., 2005. Sol-gel modified poly(dimethylsiloxane) microfluidic devices with high electroosmotic mobilities and hydrophilic channel wall characteristics, Anal. Chem. 77, 1414-1422.

Rosengarten, G., Harvie, D.J.E., Cooper-White, J., 2006. Contact angle effect on microdroplet deformation using CFD. Appl. Math. Model. 30, 1033-1042.

Sang, L., Hong, Y., Wang, F., 2009. Investigation of viscosity effect on droplet formation in T-shaped microchannels by numerical and analytical methods. Microfluid. Nanofluid. 6, 621-635.

Santiago, J.G., Wereley, S.T., Meinhart, C.D., Beebe, D.J., Adrian, R.J., 1998.

A particle image velocimetry system for microfluidics, Experiments in Fluids, 25, 316-319.

Schaerliab, Y., Hollfelder, F., 2009. The potential of microfluidic water-in-oil droplets in experimental biology. Mol. BioSyst. 5, 1392-1404.

Sethian, J. A.,1990. Numerical algorithms for propagating: Hamilton-Jacobi equations and conservation laws. J. Diff. Geom. 31, 131-161.

Shum, H.C., Lee, D., Yoon, I., Kodger, T., Weitz, D.A., 2008. Double emulsion templated monodisperse phospholipid vesicles, Langmuir, 24, 7651-7653.

Shum, H.C., Kim, J.W., Weitz, D.A, 2008. Microfluidic fabrication of monodisperse biocompatible and biodegradable polymersomes with controlled permeability, J. Am. Chem. Soc., 130, 9543-9549.

Sia, S.K., Whitesides, G.M., 2003. Microfluidic devices fabricated in poly(dimethylsiloxane) for biological studies, Electrophoresis, 24, 3563-3576.

Sinton, D., 2004. Microscale flow visualization, Microfluid. Nanofluid. 1, 2-21.

Skurtys, O., Aguilera, J. M., 2008. Applications of microfluidic devices in food engineering. Food Biophysics 3, 115.

Solvas, X., C., I., DeMello, A., 2011. Droplet microfluidics: recent developments and future applications, Chem. Commun., 47, 1936-1942.

Song, H., Tice, J. D., Ismagilov, R. F., 2003. A microfluidic system for controlling reaction networks in time. Angew. Chem. Int. Ed. 42(7), 767-772.

Song, H., Chen, D. L., Ismagilov, R. F., 2006. Reactions in droplets in microfluidic channels. J. Phys. D: Appl. Phys. 45, 7336-7356.

Squires, T.M., Quake, S.R., 2005. Microfluidics: Fluid physics at the nanoliter scale, Reviews of Modern Physcis, 77, 977-1026.

Van Steijn, V., Kreutzer, M.T., Kleijn. C.R., 2007. μPIV study of the formation of segmented flow in microfluidic T-junctions. Chem Eng Sci, 62, 75057514.

Stone, H. A., Stroock, A. D., Ajdari, A., 2004. Engineering flows in small devices: microfluidics toward a lab-on-a-chip. Annu. Rev. Fluid. Mech. 36, 381-411.

Su, F., Chakrabarty, K., Fair, R.B., 2006. Microfluidics-based biochips: Technology issues, implementation platforms, and design-automation challenges, Computer-aided design of integrated circuits and systems, 25(2), 211-223.

Tabeling, P., 2005. Introduction to microfluidics, Oxford University Press Inc., New York.

Tan, Y.-C., Cristini, V., Lee, A. P., 2006. Monodispersed microfluidic droplet generation by shear focusing microfluidic device. Sens. Actuators B 114, 350-356.

Tan, J., Xu, J. H., Li, S. W., Luo, G. S., 2008. Drop dispenser in a cross-junction microfluidic device: Scaling and mechanism of break-up. Chem. Eng. J. 136, 306-311.

Tan, J., Li, S.W., Wang, K., Luo, G.S., 2009. Gas-liquid flow in T-junction microfluidic devices with a new perpendicular rupture flow route. Chemical Engineering Journal, 146, 428-433.

Tardos, T.F., 2009. Emulsion science and technology, WILEY-VCH Verlag GmbH and Co.KGaA, Weinheim, Vol. 1.

Taylor, G., 1953. Dispersion of soluble matter in solvent flowing slowly through a tube. Proceedings of the Royal Society of London. Series A. 219, 118-203.

Teh, S.-Y., Lin, R., Hung, L.-H., Lee, A. P., 2008. Droplet microfluidics. Lab. Chip 8, 198-220.

Theberge, A. B., Courtois, F., Schaerli, Y., Fischlechner, M., Abell, C., Hollfelder, F., and Huck, W. T. S., 2010. Microdroplets in microfluidics: An evolving platform for discoveries in chemistry and biology. Angew. Chem. Int. Ed. 49, 5846-5868.

Thorsen, T., Roberts, R. W., Arnold, F. H., Quake, S. R., 2001. Dynamic pattern formation in a vesicle-generating microfluidic device. Phys. Rev. Lett. 86(18), 4163-4166.

Tice, J.D., Song, H., Lyon, A.D., Ismagilov, R.F., 2003. Formation of droplets and mixing in multiphase microfluidics at low values of the Reynolds and the capillary numbers. Langmuir 22(19), 9127-9133.

Timgren, A., Tragardh, G., Tragardh, C., 2008. Application of the PIV technique to measurements around and inside a forming drop in a liquid-liquid system, Exp Fluids, 44, 565-575.

Tong, J., Nakajima, M., Nabetani.,H and Kikuchi, Y., 2000. Surfactant effect on production of monodispersed microspheres by microchannel emulsification method, Journal of Surfactants and Detergents, 3(3), 285-293.

Tran, D. T., Mori, S., Tsuboi, D., Suzuki, M., 2009. Formation of plasma-polymerized top layers on composite membranes: Influence on separation efficiency. Plasma Process. Polym. 6, 110-118.

Urban, K., Wagner, G., Schaffner, D., Roglin, D., Ulrich, J., 2006. Rotor-stator and disc systems for emulsification processes, Chemical Engineering and Technology 29(1), 24-31.

Utada, A.S., Lorenceau, E., Link, D.R., Kaplan, P.D., Stone, H. A. Weitz, D. A., 2005. Monodisperse double emulsions generated from a microcapillary, Science 308, 537-541.

Van der Graaf, S., Steegmans, M.L.J., Van der Sman R.G.M., Schroen, C.G.P.H., Boom, R.M., 2005. Droplet formation in a T-shaped microchannel junction: A model system for membrane emulsification. Colloids. Surfaces A: Physicochem. Eng. Aspects 266, 106-116.

Van der Graaf, S., Nisisako, T., Schroen, C.G.P.H., van der Sman, R.G.M., Boom, R.M., 2006. Lattice Boltzmann simulations of droplet formation in a T-shaped microchannel. Langmuir 22, 4144-4152.

Van Steijn, V., Kreutzer, M.T., Kleijn. C.R., 2007. μPIV study of the formation of segmented flow in microfluidic T-junctions. Chem Eng Sci, 62, 7505-7514.

Wang, C., Nguyen, N.T., Wong, T.N., 2007. Optical measurement of flow field and concentration field inside a moving nanoliter droplet, Sensors and Actuators A, 133, 317-322.

Wang, K., Lu, Y. C., Xu, J. H., Luo, G. S., 2009. Determination of dynamics interfacial tension and its effect on droplet formation in the T-shaped microdispersion process. Langmuir. 25, 2153-2158.

Wang, L., 2010. Advances in Transport Phenomena: 2010, Springer-Verlag Berlin Heidelberg, ISBN: 978-3-642-19465-8.

Weigl, B. H., Yager, P., 1999. Microfluidic diffusion-based separation and detection, Science 283, 346-347.

Woodward, R.P., 2008b. Surface tension measurements using the drop shape method, 6 p. http://firsttenangstroms.com/pdfdocs/STPaper.pdf.

Xu, J.H., Luo, G.S., Li, S.W., Chen, G.G., 2006. Shear force induced monodisperse droplet formation in a microfluidic device by controlling wetting properties. Lab Chip, 6, 131-136.

Xu, J.H., Li, S.W., Tan, J., Wang, Y.J., Luo, G.S., 2006. Controllable preparation of monodisperse O/W and W/O emulsions in the same microfluidic device. Langmuir 22, 7943-7946.

Xu, J. H., Li, S. W., Tan, J., Luo, G. S., 2008. Correlations of droplet formation in T-junction microfluidic devices: from squeezing to dripping. Microfluid. Nanofluid. 5, 711-717.

Yap, Y.-F., Tan, S.-H., Nguyen, N.-T., Murshed, S. M. S., Wong, T.-N., Yobas, L., 2009. Thermally mediated control of liquid microdroplets at a bifurcation. J. Phys. D: Appl. Phys. 42, 065503.

Zheng, B., Tice, J. D., Roach, L. S., Ismagilov, R. F., 2004. A droplet-based, composite PDMS/glass capillary microfluidic system for evaluating protein crystallization conditions by microbatch and vapor-diffusion methods with on-chip X-ray diffraction. Angew. Chem., Int. Ed. 43, 2508-2511.

Zheng, B., Roach, L. S., Ismagilov, R. F., 2003. Screening of protein crystallization conditions on a microfluidic chip using nanoliter-size droplets. J. Am. Chem. Soc, 125, 11170-11171.

Zheng, B., Tice, J.D., Ismagilov, R.F., 2004. Formation of arrayed droplets by soft lithography and two- phase fluid flow, and application in protein crystallization. Adv. Mater. 16(15), 1365–1368.

Zhou, C., Yue, P., Feng, J.J., 2006. Formation of simple and compound drops in microfluidic devices. Phys. Fluids 18, 092105.

Zhou, J., Khodakov, D.A., Ellis, A.V., 2012. Review: Surface modification for PDMS-based microfluidic devices, Electrophoresis, 33, 89-104.

Zimmerman, W. B. J., 2006. Multiphysics modelling with finite element methods. Series on Stability, Vibration and Control of Systems, Series A Vol. 18 432pp. World Scientific, Singapore.

http://www.comsol.com/showroom/documentation/model/1994/